An Experimental Investigation into the Effects of Atmospheric Turbulence on the Aerodynamics of Micro Air Vehicle Wings

Ben Loxton

A Thesis submitted for the degree of Doctor of Philosophy

School of Aerospace, Mechanical and Manufacturing Engineering

RMIT University

October 2011

Abstract

One of the limiting factors preventing the widespread deployment of fixed wing Micro Air Vehicles (MAVs) in the field is their inability to maintain stable flight under windy conditions. This is of particular relevance when flying in the low level, built-up urban terrain for which their operation is well suited. Previous work by aerodynamicists has focused on the aerodynamic performance of these vehicles at the low Reynolds numbers (less than 100,000) in which MAVs operate. However, these studies have generally been restricted to smooth flow.

The aim of this research is to focus on their performance under replicated turbulent conditions such that exist on windy days, focusing on the unsteady aerodynamics and resultant transient response. It was hypothesised that the transient behaviour of the separation region on the wing upper surface has a significant effect on the performance and transient response of small flying craft. The effect of free-stream turbulence on the separation region is not well documented.

To document the relative turbulence experienced by MAVs, a wide range of measurements were made in the Atmospheric Boundary Layer (ABL) using a set of dynamic multi-hole pressure probes mounted above a vehicle. The aim of the work was to understand the statistical characteristics of the turbulence, in terms of intensity and scale, and how these vary in different terrains and under different wind speeds. Using this information, a wind tunnel was setup to replicate the important aspects of this turbulent environment using grids.

A representative flat plate MAV wing model based on the work by Pelletier and Mueller (2000) was pressure tapped, and a dynamic pressure measurement system was used to obtain mean C_p information and frequency information up to 2 kHz. Flow visualisation was used to provide further insight into the interpretation of pressure measurements and which flow phenomena they represented.

It was found that at increased turbulence levels, the overall aerodynamic performance of the wing was improved in terms of maximum C_L and L/D, and the incidence at which the wing stalled was increased from 6° to approximately 12° . Surface pressure measurements showed that in the low turbulence conditions (less than 1.5%) above an incidence of 4° , a separation bubble existed on the suction surface at the leading edge with reattachment further downstream. As the incidence was increased the separation bubble grew in size (chord-wise) up to an incidence of 8° , where the flow separated, and the wing was in the stalled condition. Dynamic pressure measurements showed this

separation region to be unstable, forming and bursting periodically and uniformly along the span of the wing. Increasing the ambient turbulence level confined the separation bubble to near the leading edge and delayed stall. At a turbulence intensity level of 7% stall was delayed until 12° and at 11.5% it was delayed completely over the tested range up to 20° . At higher turbulence levels, the amplitude of the periodic formation and bursting of a local separation bubble increased; however, the shedding remained periodic in nature.

As a result of this shedding, the overall intensity of fluctuation in total wing C_L increased in the presence of turbulence, with a spectral peak at reduced frequency (frequency/velocity) of 0.5. This frequency corresponded to a periodic formation and bursting of the separation region on the suction surface. The presence of this was validated with flow visualisation.

From this work it was evident that as the turbulence intensity in the freestream was increased, the wing experienced a delay in stall and an improvement in the overall L/D ratio. However, the increase in freestream turbulence corresponded to an increase in the intensity of the periodic formation and shedding of the separation bubble at the leading edge, resulting in a periodic fluctuation of the total forces acting on the wing.

Parts of this work have been published in the following forms:

- S. Watkins, J. Milbank, and B. Loxton. Atmospheric winds and their effects on micro air vehicles. AIAA Journal, 2006.
- S. Watkins, B. Loxton, C. Bil, M. Abdulrahim, and J. Milbank. Flow fields in complex terrain and their challenges to micro flight. In AIAA Guidance, Navigation and Control Conference and Exhibit, number 2008-6509 in AIAA, Honolulu, Hawaii, August 2008.
- S. Watkins, S. Ravi, and B. Loxton. The effect of turbulence on the aerodynamics of low reynolds number wings. In The 2010 International Conference of Mechanical Engineering. ICME, 2010.
- J. Milbank, B. Loxton, S. Watkins, and W. Melbourne. Replication of atmospheric conditions for the purpose of testing mavs. Technical report, RMIT University, 2005.

Declaration

I certify that except where due acknowledgement has been made, the work is that of the author alone; the work has not been submitted previously, in whole or in part, to qualify for any other academic award; the content of the thesis is the result of work which has been carried out since the official commencement date of the approved research program; any editorial work, paid or unpaid, carried out by a third party is acknowledged and, ethics procedures and guidelines have been followed.

Benjamin J. Loxton

October 2011

Acknowledgements

The author would like to acknowledge the valuable assistance of the following people, without whose assistance and guidance this work would not have been possible:

First and foremost the author wishes to thank Professor Simon Watkins as primary supervisor, without who's support, encouragement, guidance, wisdom and endless patience this project would not have been possible.

Dr Caleb White as second supervisor for his support.

Dr Jon Watmuff for his guidance with the experimental accuracy, his enthusiasm for experimental work and his attention to detail and accuracy of results.

Mr Gilbert Atkins, Mr Patrick Wilkins, Mr Terry Rosewarne and Mr Don Savvides and all the technical staff at RMIT University School of Aerospace, Mechanical and Manufacturing Engineering for their technical assistance, technical expertise and for their support.

Dr Riccardo Pagarelia for his assistance with numerous aspects of this work including proof reading the draft of this thesis and assistance with experimental work, as well as his friendship, support and encouragement.

Dr Juliette Milbank for her assistance with the initial phases of this work including outdoor data measurements and data processing.

Mr Peter Mousley (Turbulent Flow Instrumentation) for assistance with instrumentation, equipment calibration and data processing.

Dr Mujahid Abdulrahim (University of Florida) who as an external consultant brought much to the project by way of inspiration and guidance, as well as practical demonstration of the challenges of flying small aircraft in turbulent flow in restricted space.

Mr Matthew Marino, Mr Edward Cruz, Mr Justin Woolley and other members of the MAV Aerodynamics Group at RMIT University for their collaboration on key points in this project including wind tunnel testing, experimental set-up and model manufacture.

With a experimental investigation such as this, significant resources are required and the author would especially like to acknowledge the financial assistance of the United States Air Force Asian Office of Scientific Research for their vision and support for this work.

Friends and family for their support and optimism through out this project, including all the members of the Victorian Motorless Flight Group, the Gliding Club of Victoria and other members of the gliding community around Australia.

Contents

List of Figures

List of Tables

Nomenclature

a	Speed of sound in air (344m/s)
c	Wing chord (m)
C_D	Coefficient of drag
C_L	Coefficient of lift
C_p	Coefficient of pressure
D	Tubing system diameter (m)
f	Frequency (Hz)
F_s	Sampling frequency (Hz)
I	Turbulence Intensity Relative to the Earth Axis System
J	Turbulence Intensity Relative to the Wind Axis System
k	Reduced frequency or wave number (f/u)
L_u	Turbulence LengthScale
N	FFT block size (number of samples)
P_s	Static pressure (pa)
P_t	Total pressure (pa)
P_{xx}	Power spectrum of 'x'
Q	Total number of samples
q	Dynamic Pressure
Re	Reynolds Number
S	Reference area for force coefficient calculations (m^2)

c	Time(s)
u	Instantaneous wind velocity component in the X axis
$\bar{U}$	Mean component of flow (m/s)
U_∞	Freestream Velocity (m/s)
$U(t)$	Time-dependant flow, composed of mean and fluctuating components ($U(t) = \bar{U} + u(t)$)
$u(t)$	Fluctuating component of flow
v	Instantaneous wind velocity component in the X axis
V_w	Mean Wind Speed
w	Instantaneous wind velocity component in the X axis
α	Angle of incidence, or pitch angle
β	Angle of sideslip, or yaw angle
δ	Boundary layer displacement thickness (m)
ρ	Density of working fluid (kg/m3)
μ	Viscosity
σ	Standard deviation of the fluctuating component of freestream velocity ($\sigma_u = \sqrt{\bar{u}^2}$
τ	Time lag (auto correlation function) (s)
$'$	Fluctuating component of velocity with the mean removed
rms	Root mean square
ABL	Atmospheric Boundary Layer
AR	Aspect ratio (span/chord
IWT	RMIT Industrial Wind Tunnel
LE	Leading Edge
TE	Trailing Edge

Chapter 1

Introduction, Background and Objectives

Very small aircraft (< 1 m in span) - commonly referred to as Micro Air Vehicles (MAVs) - represent an emerging technology garnering significant interest over the past decade from military and intelligence organisations as a real-time intelligence tool. Relatively small remotely piloted aircraft are already enjoying field successes. Further miniaturisation remains an active research priority, enabling MAVs to provide intelligence gathering in locations unobservable using current technologies, for example heavily built up areas and inside buildings (Wilson and Schneph 2001).

MAVs are envisioned to operate close to ground immersed in (what wind engineers refer to as) the roughness zone, the layer of air close to the ground containing convection currents, local wakes and influences of upstream objects such as buildings. This environment is highly turbulent in conditions involving a mean surface wind. This high turbulence presents a significant challenge to any craft, artificial or natural, operating within it; developing a MAV able to maintain a stable sensor platform in any environment on windy days remains a significant challenge to be overcome if the potential of MAVs are to be realised in the field beyond "fair weather use only". Presently, the environmental flow field is emerging as a major constraint on the operations of MAVs with an increasing vulnerability to turbulence as size and speed reduces (Spedding and Lissaman 1998).

This challenge involves two key discipline areas:

- Atmospheric sciences, particularly the study of the turbulence present in the lower parts of the atmosphere, known as the Atmospheric Boundary Layer (ABL).
- The aerodynamics of small flight vehicles operating at low Reynolds number (Re) within this turbulent environment.

Traditionally these two research disciplines are studied separately. Aircraft engineers design aircraft in smooth flow environments (experimental and computational) using statistically generated loading spectrums to design for gust loading and response for extreme cases only. Study of low *Re* flight and flow behaviour is similarly restricted to the smooth flow domain, whilst atmospheric scientists and meteorologists focus on large scale motions and longer duration disturbances. There are useful insights to be gained from studies in wind engineering concerning the lower levels of the atmosphere and effects on the loading of large structures such as bridges and buildings, including works concerning the dispersion of pollutants around buildings.

With the flight of MAVs significantly influenced by relevant environmental turbulence, traditional aeronautical design and control methodologies need to be revisited. This work aims to do so, investigating the flow environment in which MAVs are required to operate and the effect of this environment on the aerodynamic performance of very small aircraft.

The remainder of this chapter examines the relevant background in MAV development and design and the current body of knowledge in atmospheric research and wind engineering, particularly that of the roughness layer near the ground. Specific research goals of this work are presented at the end of this chapter.

1.1 Micro Air Vehicles: Definition, Development and Challenges

Strategists of leading governments and military agencies demand real time intelligence in any environment at any time (Wilson and Schneph 2001). This paradigm, and the conceptual goal of MAV utilisation is evidenced in the following excerpt from a presentation given by James M. McMichael, then program manager of the Defence Advanced Research Projects Agency (DARPA), United States Government in 1997 describing a future airborne intelligence gathering device (McMichael and Francis 1997):

"The small speck in the sky approaches in virtual silence, unnoticed by the large gathering of soldiers below. In flight, its tiny size and considerable agility evade all but happenstance recognition. After hovering for a few short seconds, it perches on a fifth floor window sill, observing the flow of men and machines on the streets below. Several kilometers away, the platoon leader watches the action on his wrist monitor. He sees his target and sends the signal. The tiny craft swoops down on the vehicle, alighting momentarily on the roof. It senses the trace of a suspected chemical agent and deploys a small tagging device, attaching it to the vehicle. Just seconds later it is back in the sky, vanishing down a narrow alley. Mission accomplished...."

1.1.1 Proposed MAV Target Missions and Deployments

Possible missions envisioned for MAVs by Ricketts (2001) and Sinha et al. (2001) highlight real-time intelligence gathering. Military missions suggested for MAVs include squad-level combat, battle damage assessment, air or artillery spotting, sensor dispersal, communications relay, and detection of mines and hazardous substances (illustrated in Figure 1.1). MAVs could also be equipped with small jamming systems to confuse radar or communications equipment at very short range. MAVs capable of hovering and vertical flight may be used to scout out buildings for urban combat and counter terrorist operations (Burger 2002). MAVs could be utilised in a search and rescue role by being included in a airman's survival kit, used by a downed pilot to keep track of approaching enemy search parties, or relay communications to search and rescue units. Civil applications also exist in the fields of counter terrorism, border patrol, remote sensing, wild fire detecting, and special event security.

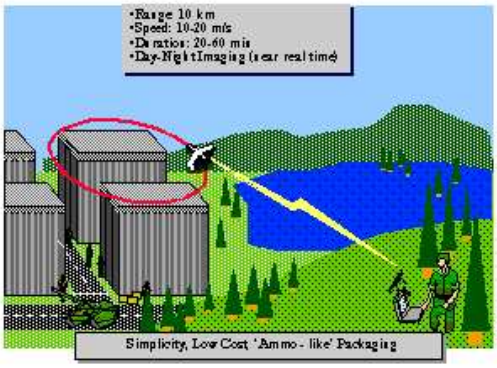

(a) Loiter above a target

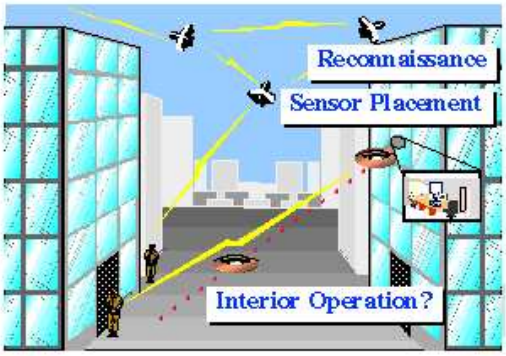

(b) Expand line of sight

(c) Remote sensor platform

Figure 1.1: Proposed MAV deployments (McMichael and Francis 1997)

The fundamental requirements for these vehicles underlying their great strategic appeal are that they be cheap, disposable, and difficult to detect. A more detailed set of ideal requirements was identified Pines and Bohorquez (2006), suggesting a nominal price of USD$1500 per unit, rendering

units a "throw-away item" allowing deployment into hazardous situations where more expensive units or personnel could not be risked. Characteristic small size assists both economically, keeping a low per-unit cost in mass production, and operationally, in detection avoidance.

1.1.2 Definition and Development of MAVs

Miniaturisation of electronics, improvements in propulsion and energy storage have driven rapid development of MAVs in the last two decades. Development has seen several phases, from an initial DARPA specification (early 1990s) to more recent definitions of larger operational aircraft. Not all MAVs are of fixed wing configuration, with active research on fixed, rotary and flapping wing craft, as well as some hybrid concepts employing numerous original configurations. Biologically inspired flapping wing craft (Shyy et al. 1999), whilst not as mature as more conventional designs, also enjoying a high level of current development and some recent success.

1.1.2.1 The Initial DARPA Specification

A formal MAV definition by DARPA (McMichael and Francis 1997) proposed an aircraft not exceeding 15 cm in all dimensions. A program was funded with the aim to develop emerging technologies that could evolve into a mission-capable flight system for military surveillance and reconnaissance applications. Whilst this program yielded many unique designs (Figure 1.2), all flyable aircraft realised were decidedly difficult to operate outdoors on all but the calmest day, largely due to low mass and small size, rendering them highly susceptible to transient atmospheric disturbances (Pines and Bohorquez 2006).

The early MAVs developed to the DARPA specification were typically of conventional fixed rigid-wing design. In an effort to maximise the wing area and payload capacity, they tended towards flying wings of low aspect ratio, driven by the geometric 15×15 cm limitation. One notable example this specification was the successful *Black Widow* MAV developed by AeroVironment (Grasmyer and Keennon 2001) in the late 1990s, shown in Figure 1.2(a). The Black Widow had a 15 cm wing span with aspect ratio (AR) of 1. It was powered by an electric motor and flown by remote control via video downlink from an onboard camera. The aircraft had an endurance of approximately 30 minutes, and a range of 1.8 km.

1.1.2.2 Refinement and Progression of the MAV Concept

Initial efforts to develop a MAV to the original DARPA 15 cm specification highlighted a number of limitations including aircraft handling and payload capacity. Later developments subsequently moved away from the 15 cm constraint in an effort to develop aircraft better able to fulfil proposed mission requirements. By 2002 MAVs were being developed with wing spans ≤ 40 cm weighing ≤ 270 g, for

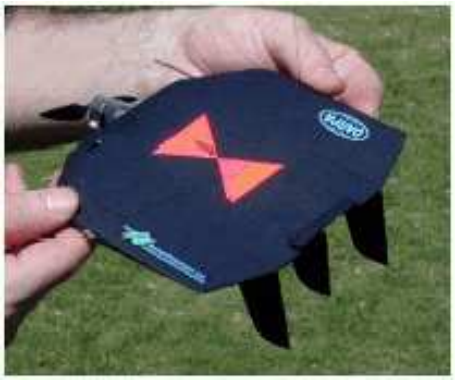

(a) AeroVironment Black Widow

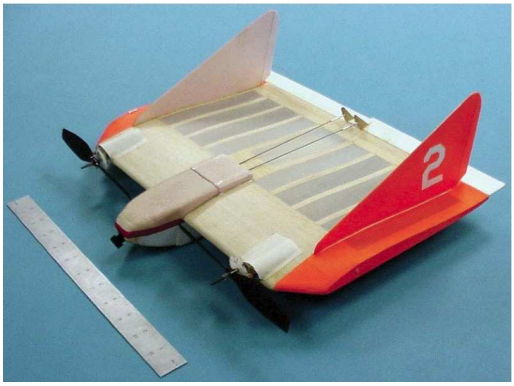

(b) MITE US Naval Research Labratory

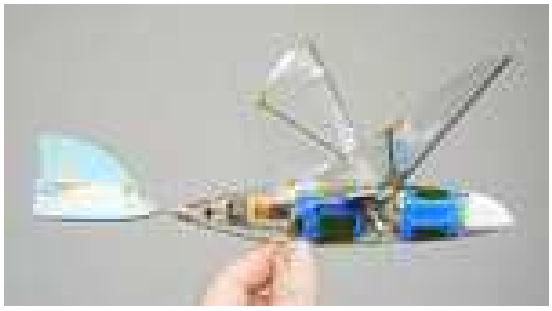

(c) Microbat

(d) Lockheed-Martin Microstar

Figure 1.2: Some examples of MAVs developed to meet the proposed 6 in (15 cm) 1996 DARPA specification (public domain images)

example the *Wasp* and *Hornet* (by AeroVironment, shown in Figure 1.3). The Wasp could carry a surveillance package and stay aloft for over an hour.

Further development focussing on utility saw larger but still "man-portable" aircraft being produced, which a soldier could carry in their kit and deploy in-field. Such concepts have spurred a new wave of development with wingspans ≤ 1 m and subsequently much higher performance, range, payload capacity and better handling. Examples include the *Dragoneye* and *Raven* Mini-UAVs depicted in Figure 1.4, which have seen successful field deployment and are currently in military service (as of 2010).

MAV development has been boosted by a number of university-based competitions around the world since 1998, largely due to their relative simplicity, low development cost and design challenge. Major events held by the University of Florida (USA) and the European IMAV competition (Braunschweig, Germany) are notable examples. A typical competition goal is to been to design, build and fly a MAV which must complete a given mission, including flying a certain distance, photographing a target and returning to the take off point.

Recently attention has turned again towards very small aircraft, with recent advances in electronics

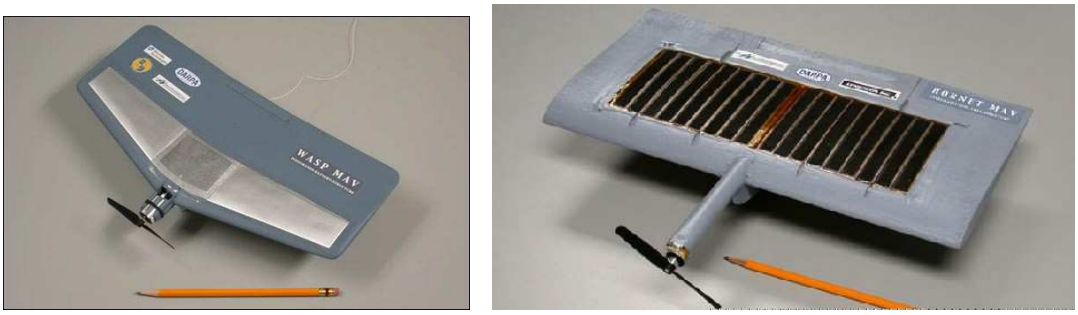

(a) AeroVironment Wasp I 33 cm MAV (b) AeroVironment Hornet Fuel cell 38 cm MAV

Figure 1.3: Larger second generation MAVs by AeroVironment (public domain images)

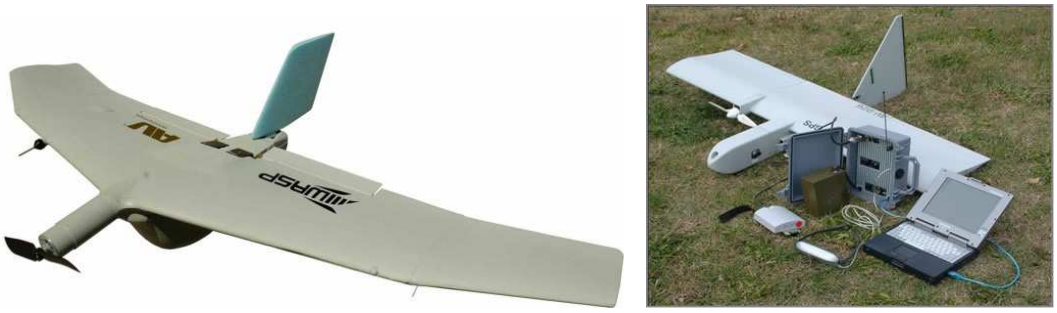

(a) 3rd Generation AV Wasp III 41 cm span (b) Dragoneye 1.34 m Mini-UAV

Figure 1.4: Examples of larger "Mini-UAV" category aircraft (public domain images)

miniaturisation allowing smaller craft to carry a useful payload. A new category of aircraft with wing spans <7 cm is being investigated by DARPA dubbed Nano-Air Vehicles (NAVs). Even smaller concepts have been put forward, including vehicles that mimic insects, robotic flys and sensors that that float on the air akin to seeds in wind, a concept called *"smart dust"*.

For the remainder of this work, the term "Micro Air Vehicle" will be used to describe a class of remotely piloted aircraft with a wingspan $\leq$1 m (operating at Re <500,000), which encompass the majority of small craft being development at the time of writing.

1.1.3 Current and Future Developments

Current development efforts may be loosely categorised into:

- fixed wing
- rotary wing
- flapping wing and

- other unique concepts such as morphing aircraft.

Much of the rationale behind unique concepts stems from attempts to improve the handling of rigid fixed wing craft described previously, particularly when flown outdoors.

While fixed wing designs offer many advantages (simple construction, low cost, durability, good payload capacity and good endurance) susceptibility to turbulence and gusts is a significant problem preventing MAVs from widespread use. Researchers have explored a number of methods to improve handling and stability. Other configurations such as rotary and flapping wing craft have been investigated, although debate exists as to which configuration offers greatest benefits in turbulent conditions. While small rotary wing aircraft have been successfully demonstrated, flapping wing craft are yet to reach comparable maturity allowing comprehensive comparison; challenges in control, power efficiency and reliability are yet to be overcome. This represents a very active current research effort.

Further variations still have been presented, one notable example is the *Samurai* MAV developed by Lockheed Martin. The Samurai mimicked flight dynamics of the sycamoore seed and was powered by a thruster on the tip. The vehicle spins at high rpm, thereby achieving gyroscopic stability with (presumably) significant control challenges.

Despite these innovations, the allure of a fixed wing craft that can maintain stable flight outdoors remains strong. Researchers draw inspiration from nature, where one can observe birds and even insects (with masses far less than MAVs) flying on windy days around the city. They are able to successfully navigate a flight path with precision, picking up a object mid flight, or landing neatly on a thin branch or window ledge. Research focused on improving the handling and stability of fixed wing MAVs has resulted in several key concepts, including flexible and variable geometry. Collectively these developments concern morphing MAVs, such as those developed by the University of Florida (Abdulrahim 2007).

Hoover (1999) noted that flexible wings might alleviate some of the effects of turbulence, but that small gusts have extremely detrimental effects on such small craft. Investigations of the controllability of MAVs, including a 6 cm span MAV by Jenkins et al. (2001) analysed flight control positions via reversal counting and autospectra, in order to determine the best aircraft under a range of atmospheric conditions. It was concluded that control workload was unquestionably related to how often rapid (in the range 1-10 Hz) control movements must be made to maintain stability.

Flexible structures and morphing wings Abdulrahim (2007) have been proposed as a method of passively compensating for the variations in lift over the wingspan by changing shape as the structure is exposed to the loading cycles. Lian and Shyy (2007) compared the performance of rigid and flexible airfoil performance and concluded that the transient geometry of the flexible membrane caused significant variation in wing performance and bubble behaviour.

1.2 Aerodynamics of MAVs

Due to their small size and low flight speeds (5-15 m/s), MAVs operate at a relatively low chord *Re* of between $10^4 - 10^6$ (Figure 1.5). Work by several authors, including Hu and Yang (2008), Ward (1963) and Mueller (2001) show that the aerodynamic performance of airfoils used on lifting surfaces reduces as *Re* decreases, a phenomenon largely attributed to the behaviour of the boundary layer (which remains largely laminar), the formation of laminar separation bubbles on the surface, and the increased influence of fluid viscosity on fluid behaviour. A review by Spedding and Lissaman (1998) suggests this low *Re* environment poses one of the greatest challenges for MAV designers given effects on both lift production and propulsive efficiency, with Mueller (2001) acknowledging a significant knowledge deficit in this flight regime.

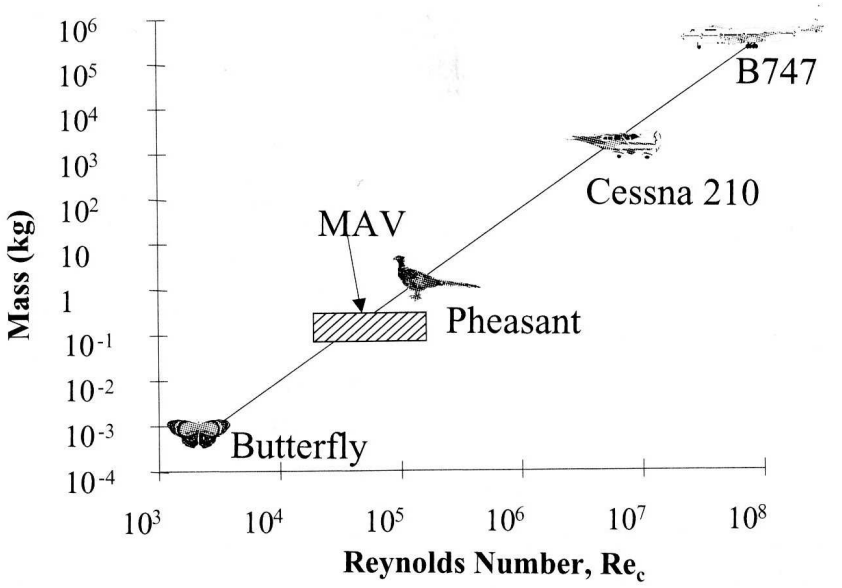

Figure 1.5: Typical operating *Re* range of MAVs (Mueller 1989)

A review by Pines and Bohorquez (2006) similarly highlights the lack of knowledge regarding fundamental flow physics in this this low *Re* regime required to produce accurate predictions to assist designers in modelling the steady and unsteady environments that MAVs encounter during flight. This seems relevant with regard to operation on windy days when high levels of turbulence are present in the ABL near the ground, particularly how this turbulence interacts with the airfoil boundary layer at low *Re*.

This section provides a review of relevant literature regarding low *Re* aerodynamics, exploring the extent of the performance deficit between finite and infinite wings, as well as specific flow phenomena present in this *Re* range - such as separation bubbles and their influence on aerodynamic performance.

1.2.1 Performance of Lifting Surfaces at Low *Re*

Designers aim to optimise the performance of an aircraft for a particular mission. Higher performance aircraft have a more "efficient" wing, and a measure of the efficiency of the a wing is given by the lift-to-drag (L/D) ratio. A variety of numerical techniques have been developed to aid designers in optimising an airfoil and wing geometry to achieve optimum efficiency. Modern aircraft designs commonly achieve section L/D values >100. However, research has shown that at low Re ($< 10^6$) wing efficiency reduces significantly. Additionally, the methods traditionally used for airfoil design no longer accurately predict airfoil performance, especially for thin wing sections and low aspect ratio wings (Mueller 2001). The issue of performance reduction at low Re has been investigated by several authors; however, significant knowledge gaps exist in relevant fluid mechanics at low Re principally concerning flow separation and reattachment and the associated effect on airfoil performance. This is also true regarding the effects of high levels of free-stream turbulence on the performance of low Re wings, which is the principle focus of this thesis and elaborated upon later.

1.2.1.1 Performance of Infinite Span (2D) Wings

Airfoil section performance is typically measured experimentally by a wind tunnel model spanning test section width or height using the walls as reflection planes, leading to them being referred to as infinite, or 2D wings. Results are obtained by acquiring either section force and/or surface pressure data.

The effect of reducing Re on airfoil performance was investigated by McMasters and Henderson (1980). Figure 1.6 shows the maximum section lift coefficient ($C_{L_{\text{Max.}}}$), minimum section drag coefficient ($C_{D_{\text{Min.}}}$) and maximum lift to drag ratio ($\frac{C_L}{C_{D_{\text{Max.}}}}$) as a function of Re for several typical wing types. For smooth airfoils, a reduction in Re shows the expected corresponding reduction in $C_{L_{\text{Max.}}}$, increase in $C_{D_{\text{Min.}}}$ and reduction in the overall $\frac{C_L}{C_{D_{\text{Max.}}}}$ (or reduction in the efficiency) of the airfoil. In all cases the sharpest gradient occurs around $Re = 10^5$, indicating that this Re range corresponds to a transition point in wing performance between high and low Re values. This Re range corroborates findings by Horton (1968), who demonstrated that separation bubbles form in this Re range; the results of Figure 1.6 indicate the presence of long chordwise bubbles (discussed further later). Additional work has been done on analysing many specific airfoil types at low Re.

Pelletier and Mueller (2000) examined the performance of thin wings at low Re by comparing experimental measurements on a thin 2% thick flat-plate wing and a 4% cambered variant of the same geometry (Figure 1.7) at $Re = 8 \times 10^4$ and $Re = 1.4 \times 10^5$. The models were mounted in a wind-tunnel test section with removable end plates to approximate a 2D wing, and connected to a force balance acquiring lift and drag force. In Figure 1.8 results for the 2D case are shown against various finite AR cases at $Re = 1.4 \times 10^5$. Pelletier and Mueller showed that for the 2D case there exists a reduction in C_L and an increase in C_D at $8 \times 10^4 \leq Re \leq 1.4 \times 10^5$; however, the potential influence on results of a relatively thick boundary layer close to the endplates was speculated.

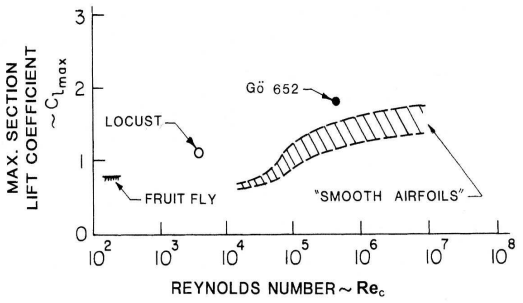

(a) Maximum section lift coefficient vs. *Re*

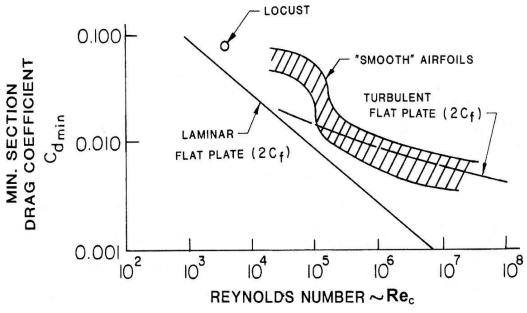

(b) Minimum section drag coefficient vs. *Re*

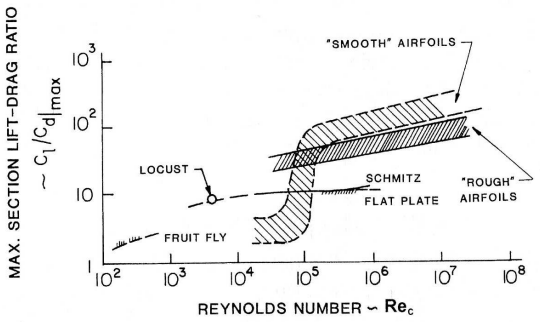

(c) Maximum lift to drag ratio vs. *Re*

Figure 1.6: 2D (infinite span) wing performance as a function of *Re* (McMasters and Henderson 1980)

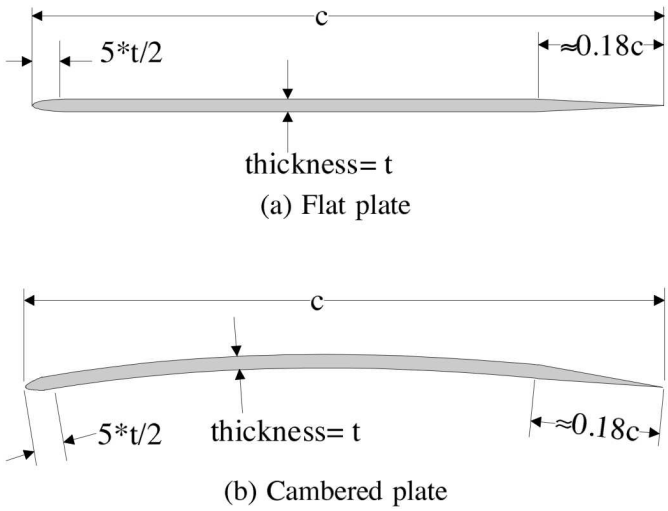

Figure 1.7: Airfoils tested by Mueller (1999) for 2D tests

1.2.1.2 Performance of Finite Span (3D) Wings and Effect of Aspect Ratio

Infinite wings are useful to study the performance of a airfoil; however, wings in use on aircraft are of finite span (free wing tips without endplates). Due to the pressure differential between upper and lower surfaces of a lift-generating finite wing, a net flow from the higher to lower pressure surfaces around the wing tip creates a net span-wise flow component on both surfaces, resulting in the formation of a vortex at the wing tip. The strength of the pressure differential defines the strength of this vortex (Figure 1.10). Since this pressure distribution between the suction and pressure surface must reduce to zero at the tip, lift varies with span, resulting in a non-uniform lift distribution (Figure 1.11). Whilst the basic properties of finite wings should be kept in mind when considering the work presented, specific details of finite wing aerodynamics will not be presented here; rather the reader is encouraged to consult to any number of texts on the subject for further explanation, for example that by Houghton and Carpenter (1993) or Street et al. (1996).

Due to the influence of the tip vortex, the wing experiences an overall upwash effect. This causes an additional drag component (in addition to the drag produced by the wing section alone) called induced drag. It can be shown, though the details will not be presented here, that the induced drag is a function of the lift produced by the wing, and is inversely proportional to the aspect ratio (AR) of the wing (Equation 1.1). Thus to reduce the effect of the tip vortex and improve overall wing efficiency, it is necessary to increase AR. In extreme cases, for example sailplane design – where low drag and high efficiency are the design goal – very high aspect ratio wings are used.

$$C_{d_i} = \frac{C_L}{\pi e AR} \tag{1.1}$$

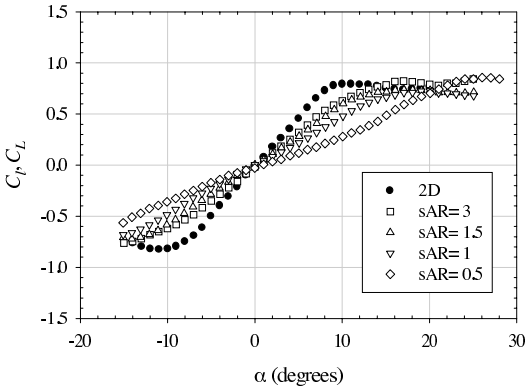

(a) C_L vs. α

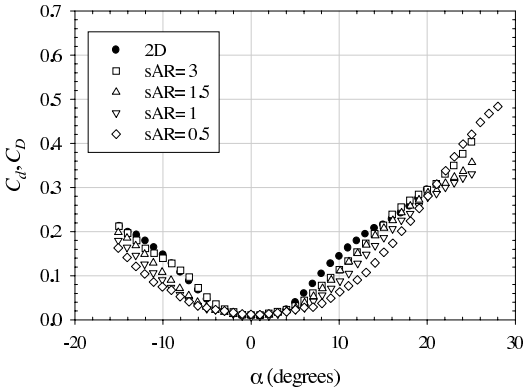

(b) C_D vs. α

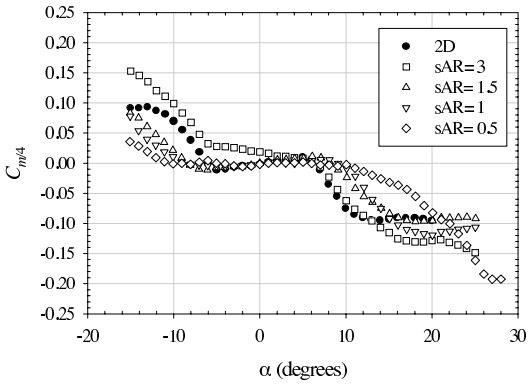

(c) C_M vs. α

Figure 1.8: Wind tunnel results for a flat plate of different aspect ratios at $Re = 1.4 \times 10^5$ (Pelletier and Mueller 2000)

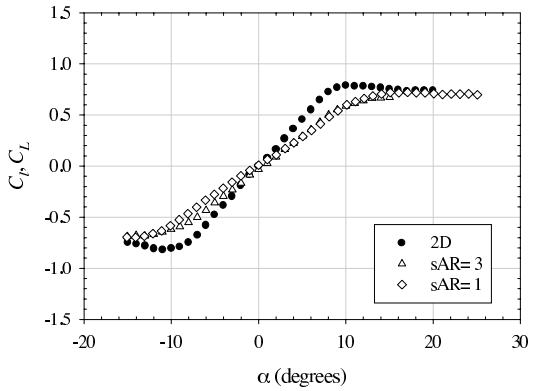

(a) C_L vs. α

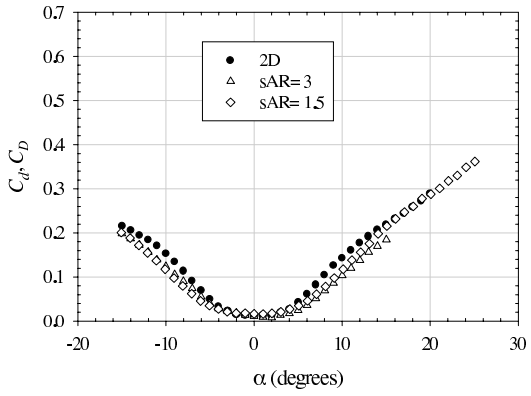

(b) C_D vs. α

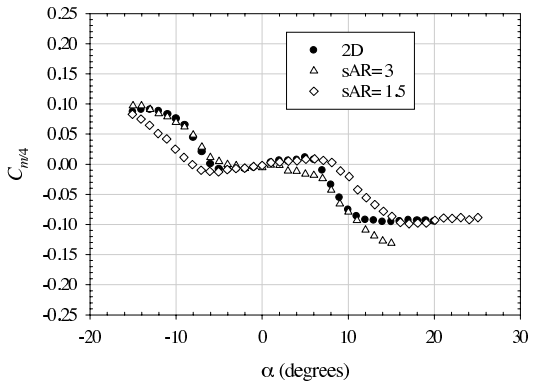

(c) C_M vs. α

Figure 1.9: Wind tunnel results for a flat plate of different aspect ratios at $Re = 80,000$ (Pelletier and Mueller 2000)

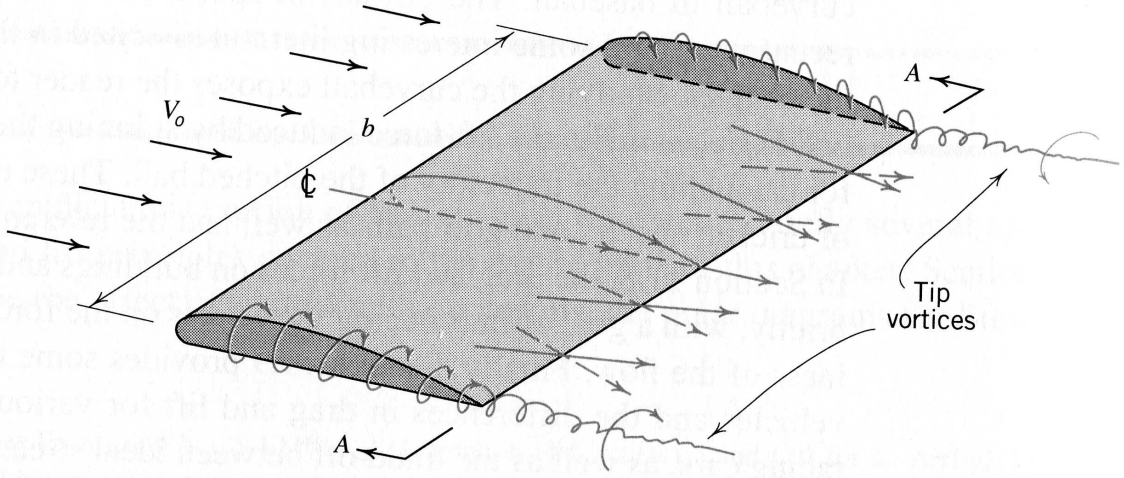

Figure 1.10: Flow field for a finite wing (Street et al. 1996)

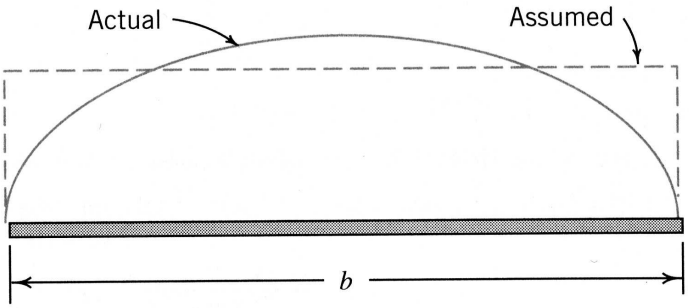

Figure 1.11: Lift distribution over a finite wing (Street et al. 1996)

Traditional MAVs of the initial DARPA specification have relatively low AR wings – in some cases near 1 – resulting in high induced drag and poor lift to drag ratios. This, combined with the reduced performance of the wing sections at the low Re at which these craft operate, yield typically low performance with overall $L/D \leq 6$ in some cases. Torres and Mueller (2000a) highlighted a fundamental lack of information regarding the performance of very low AR wings at low Re, and described measurements on low AR wings at $7 \times 10^4 \leq Re \leq 1.5 \times 10^5$. It was demonstrated that performance reduces with reducing AR, also showing that for a rectangular platform with AR < 1, the lift curve became non-linear at high angles of attack.

Pelletier and Mueller (2000) performed wind tunnel tests with finite wings based on the same geometry as that used for 2D tests (Figure 1.7) enabling a comparison between 2D and 3D results for $1 \leq$ AR ≤ 3 (shown in Figures 1.8 and 1.9 for $Re = 1.4 \times 10^5$ and $Re = 8 \times 10^4$ respectively). It was shown that at an Re of 1.4×10^5 as AR was reduced from 3 to 0.5, C_L and C_D were reduced at α of less than 20° , with the effect greater for AR$<$ 1. At α greater than 20° there was some delay

in lift reduction and a large increase in drag for the AR= 0.5 case. At $Re = 8 \times 10^4$ the reduction in performance was similar than for the higher Re case, with an overall reduction in both lift and drag. It was also shown that the wings based on the 4% camber airfoil section showed improved performance over the flat plate.

Later work by Torres and Mueller (2004) tested a number of platform shapes each utilising a 2% thick flat plat section with a wing AR between 2 and 0.5 (Figure 1.12) to further investigate the performance of low AR wings at low Re and sensitivity to platform geometry. It was concluded that wing platform had a significant effect on wing performance, with the "inverse Zimmerman" platform type proving the most efficient at AR$<$ 1, with the elliptical plan form more efficient at higher AR. It was again shown that large non-linearities were present in the lift curve at AR$<$ 1.25. It appears from this work that a transition point is reached at AR= 1.25 between linear and non-linear behaviour in the lift curve at high α, Torres and Mueller (2004) indicate that such non-linerities at low Re and at low AR are now well modelled using conventional analytical techniques.

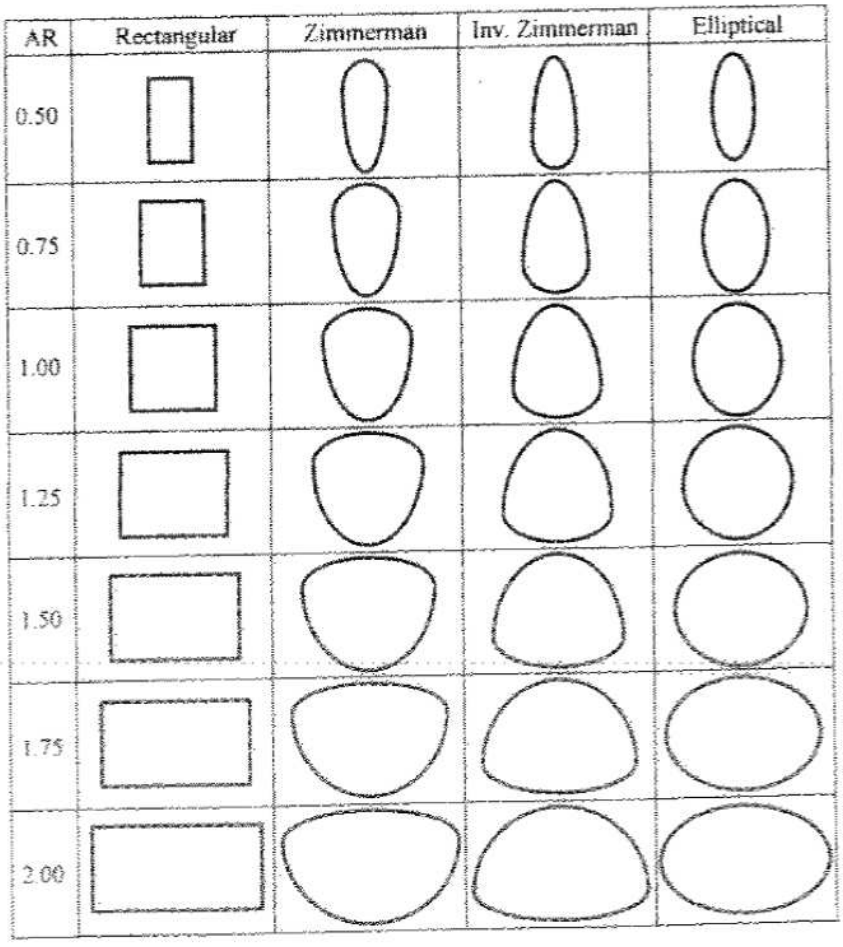

Figure 1.12: Flat-plate based platforms tested by Torres and Mueller (2004)

1.2.2 On Laminar Separation Bubbles

At the low Re typical of MAV flight, the airfoil boundary layer remains laminar over much of the wing. A review by Lian and Shyy (2007) notes that the laminar boundary layer maybe unable to resist the adverse pressure gradient (depending on its strength) immediately past the suction peak, resulting in separation of the shear layer from the surface. If the conditions are suitable, the resulting free shear layer may undergo turbulent transition and reattach to the surface downstream forming a separation bubble (Figure 1.13). The behaviour of this bubble, including its formation, growth and stability, has a significant influence on the aerodynamic performance of lifting surfaces and subsequently the overall performance and stability of the aircraft.

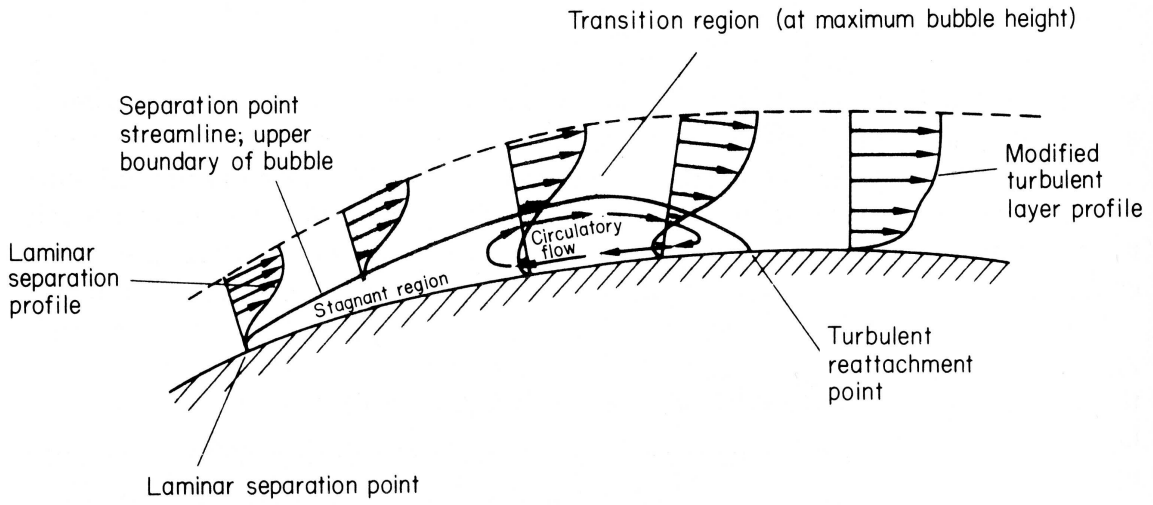

Figure 1.13: Typical time averaged features of a transition bubble (Houghton and Carpenter 1993)

Early observations of the laminar separate bubble were made by Jones (1934) during an investigation of airfoil stall. Some decades later the phenomenon was revisited by Horton (1968), Gaster (1969) and others as designers used thinner airfoils for high speed applications which became susceptible to stall due to bubble bursting. The problem of laminar separation has recently gained renewed attention as designers look to reduce drag and improve the aerodynamic efficiency of aircraft by using airfoil sections that promote a high degree of laminar flow (such as those used in sailplane design for several decades, albeit at slightly higher Re). Recent developments in MAV and small UAV research at low Re ($< 10^6$) have spurred a renewed interest in bubble formation and stability.

Gaster (1969) theorised that the mechanism for separation is the slowing of the boundary layer shear layer due to the presence of an adverse pressure gradient past the suction peak. At the point where the velocity becomes zero the flow separates and forms a laminar free-shear layer. At some point downstream this laminar free-shear layer transitions to turbulent, and may or may not reattach to the surface. This region of separated flow is termed a laminar separation bubble, and its presence has a significant effect on the pressure distribution around the airfoil. At higher angles of incidence

this bubble may fail to reattach and burst, resulting in a transient change in the forces and moments acting on the airfoil. Flow characteristics within the bubble include a constant surface pressure gradient and the presence of reversed flow and circulation within the bubble (Figure 1.13). Work by Arena and Mueller (1980) showed that this separation could be delayed or removed by tripping the boundary early before the suction peak, thereby creating a boundary layer condition that could resist the adverse pressure gradient further downstream and avoid separation. This technique, in addition to designing airfoils with a suction peak a long way aft on the airfoil chord, has been used with good success in improving the performance of sailplanes which are prone to the effects of laminar separation at certain low-speed flight regimes.

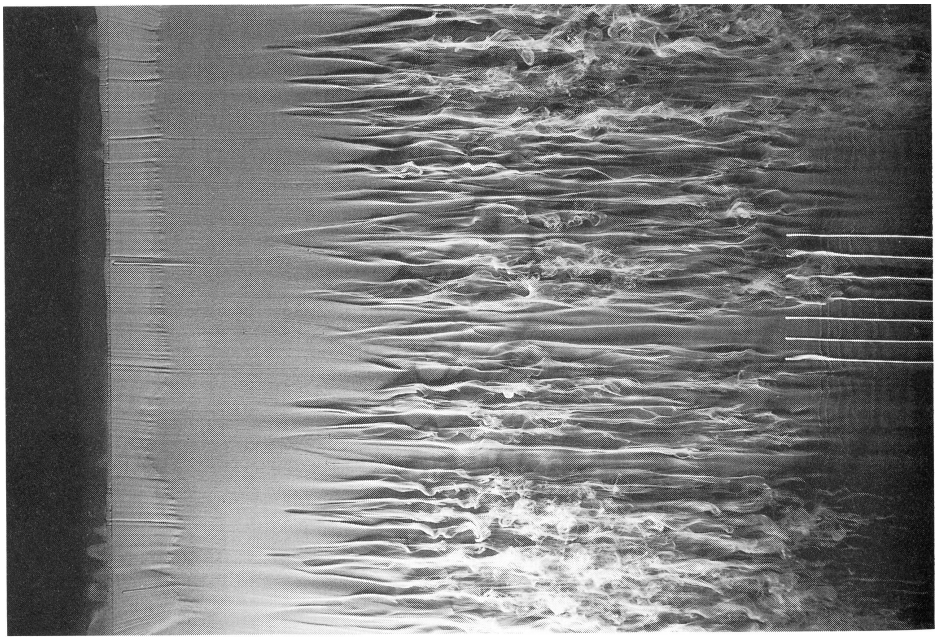

Figure 1.14: Boundary layer transition on a flat plat at zero incidence (Houghton and Carpenter 1993)

1.2.2.1 Bubble Classification: Long and Short Bubbles

A review by Ward (1963) points to early work by Von Doenhoff (1938) and later McGregor (1954) defining two fundamental types of separations bubbles, long and short, that may form on an airfoil suction surface. Short bubbles are small, less than 1% of chord and typically reduce in size with increasing *Re* or incidence. Due to their small size, their presence bears little effect on the overall forces and moments produced by the airfoil; however, at a critical incidence the bubble may burst, leading to stall. Short bubbles are classically referred to as *laminar separation bubbles* in literature, as opposed to long bubbles forming under different conditions (Von Doenhoff 1938). By comparison long bubbles can be any length ranging from a few percent to the entire chord length. The presence of such large bubbles has a significant effect on the pressure distribution and the magnitude and

position of the suction peak, affecting ultimate wing lift and drag.

McGregor (1954) observed that short bubbles generally remain small and located near the wing leading edge, moving forward with increasing incidence up to stall, at which point the rear separation point in the turbulent boundary layer downstream of the bubble can move forward causing separation on the upper surface termed trailing edge stall. Alternately, the short bubble may burst to form a large bubble, or a free shear layer causing leading edge stall. The exact mechanism depends on the specific airfoil used, Re and flow condition.

Ward (1963) suggests that at high incidence and at Re between 5×10^4 and 1.5×10^5, the short bubble may burst, forming a long bubble or a free shear layer. This transition from a short to long bubble with reattachment downstream, or to a completely separated shear layer with no reattachment, may occur gradually with changing conditions or quite quickly depending on airfoil properties. A long bubble may initiate at a few percent of chord at moderate incidence and grow as incidence is increased. A long bubble changes overall pressure distribution, causing a reduction in the suction peak and resulting loss of lift (and increase in drag) as incidence is increased. This gradual progressive stall is often observed on thin airfoils and known as *thin airfoil stall*.

A number of studies have attempted to determine criteria defining bubble formation for either type. The Owen-Klanfer criteria (Owen and Klanfer 1955), determines which type of bubble forms based on the *displacement thickness* Re ($Re_{\delta^*} = U\delta^*/v$) of the boundary layer at the separation point. At $Re_{\delta^*} < 400$ a long bubble will form, and for $Re_{\delta^*} > 550$ a long bubble is more likely. Later work by McGregor (1954) and Gaster (1969) show this criteria to be inadequate; however, Horton (1968) demonstrated that the value of Re_{δ^*} by itself was inadequate for determining the bubble condition and therefor no conclusive criterion exists determining which bubble, if any, may form. It was, instead, demonstrated that many airfoils may show both types depending on incidence and Re.

1.2.2.2 Bubble Bursting, Stall and Unsteadiness

Thin wing sections, as studied by Pelletier and Mueller (2000) and described above have exhibited unsteady stalling properties at high incidence. Initial observations by Jones (1934) described strong fluctuations in lift and drag on thin wings near stall; later work by McCullough and Gault (1951) identified three distinct types of stall at low Re:

- *Trailing edge stall* is preceded by movement of the turbulent separation point forward from the trailing edge with increasing angle of attack.
- *Leading-edge stall* where abrupt flow separation near the leading edge generally occur without subsequent reattachment.
- *Thin-airofil stall* is preceded by flow separation at the leading edge with reattachment at a point which moves progressively rearward with increasing angle of attack.

McCullough and Gault demonstrated that stall type is dependant on several factors, such as Re, free stream turbulence level, airfoil shape and surface quality. It is also possible that a particular airfoil may produce different stalling characteristics depending on the flow conditions.

McGregor (1954) observed for a thin wing with a sharp leading edge that exhibits thin-airfoil-type stall, as incidence is increased the short bubble present at the leading edge eventually bursts, extending further downstream either forming a long bubble or failing to reattach. This bursting of the short bubble and subsequent reattachment downstream has a profound effect on pressure distribution (and hence lift force and moments acting on the airfoil). Subsequent work by Horton (1968) attempted to predict bubble-bursting, proposing a model for bubble growth and bursting based on the external velocity at the point of separation and reattachment, based on local Re. Later work by Gaster (1969) showed this to be an over simplification, giving rise to bursting criteria applicable in only a few cases. Tani (1964) proposed that bursting occurred when the pressure recovery coefficient reaches a critical value based on the *Crabtree criterion* (Crabtree 1958); however, Tani concluded that much further study was required. A detail study of laminar separation bubbles was performed recently by Hu and Yang (2008) correlating pressure measurements with flow field data using particle image velocimetry (PIV), concluding that the bubble length remained independent of angle of attack, and bursting occurred when the adverse pressure gradient became too severe (typically at $\alpha > 12^\circ$). This suggests that a criterion for bubble bursting is dependant on airfoil geometry, and whilst criteria based on pressure recovery may be generally plausible, it is unlikely to be exactly applicable in all cases.

In some cases unsteadiness has been observed near stall due to periodic bubble formation and bursting. This unsteadiness, occurring over a large percentage of chord, produces variation in the airfoil pressure distribution and hence in resulting forces and moments. Chen and Fang (1996) showed that at angles of attack above 10° on a flat plate, the shedding frequencies and associated Strouhal numbers (Equation 1.2) can be predicted and remain constant. Chen and Fang studied this unsteadiness using a flat plate with bevelled leading edge. This work showed that a Strouhal number (Equation 1.2) of approximately 0.16 remained largely constant at α between 10° and 90° and was independent of Re. At lower α the effect of Re was significant and unpredictable due to the presence of downstream reattachment. Observations by McCullough and Gault (1951) on a NACA 63-009 airfoil at a $Re = 5.8 \times 10^6$ showed large periodic variations in force at relatively low frequency consistent with the later observations by Chen and Fang. Broeren and Bragg (1998) performed flow visualisation experiments confirming the presence of both laminar separation bubbles near the leading edge and trailing edge separation on a LRN-700 series thin airfoil, exhibiting unsteady thin airfoil stall. Results from this work also showed interaction between the leading edge bubble and trailing edge separation as the airfoil stalled and re-stalled, causing the unsteadiness characteristic to thin-airfoil type stall.

$$St = f.c.sin\frac{\alpha}{U_{\inf}} \tag{1.2}$$

Broeren and Bragg (2001) further investigated the unsteady stalling characteristics of a thin airfoil at low Re by acquiring dynamic data in a smooth flow wind tunnel. For airfoils exhibiting leading or trailing edge stall types, relatively little unsteadiness was observed. Where thin airfoil stall was present, unsteadiness levels were high. Where a combination of thin airfoil and leading edge stall was present unsteadiness was nearly double that of the thin-airfoil case alone. It was noted that a laminar separation bubble was a common feature in the flow field of separation modes presenting with significant unsteadiness.

1.2.3 On the Influence of Free-stream Turbulence on Wing Performance at Low *Re*

Further study into the mechanisms promoting unsteadiness and bubble bursting, and the effect of free-stream turbulence on bubble stability, formation and growth has led to some research highlighting an improvement in overall aerodynamic performance in the presence of turbulence, albeit at higher Re then those encountered in MAV flight. In recent years, this work has found renewed urgency with real applications to MAVs. The presence of free-stream turbulence levels delays the formation of laminar separation bubbles, thereby reducing the performance loss due to the presence of a laminar separation bubble, and reduces the unsteadiness at stall for very thin wings.

Mueller (1999) investigated the effect of free-stream turbulence on the behaviour of the laminar separation bubble on the leading edge of a 11% thick Lissaman airfoil: increasing the free-stream turbulence resulted in a improvement in $C_{L_{\text{Max.}}}$. It was theorised that this increase in $C_{L_{\text{Max.}}}$ and delayed onset of stall was caused by the earlier transition of the laminar shear layer to turbulence prior to the suction peak thereby preventing separation and bubble formation.

The reduction of performance and effects of turbulence at low Re is not only a active research field for MAV designers, it is also of interest to designers of sailplanes, UAVs and some GA aircraft which employ high aspect ratio wings for improved efficiency. Wind turbines are a growing area of research - turbine efficiency is highly dependant on rotor blade aerodynamic efficiency, which operate at relatively low Re (approximately 10^5) and in an environment of potentially high free-stream turbulence (both from surrounding terrain upstream and other turbines in close proximity). Swalwell et al. (2004) considered the performance of a NACA airfoil section in the presence of large turbulence length scales simulating atmospheric conditions; results showed a significant delay in the onset of stall in the presence of atmospheric turbulence, with a clear increase in $C_{L_{\text{Max.}}}$ consistent with other work in the area.

1.2.4 Notes on the Computational Simulation of Complex Low *Re* Flows

Computational methods are useful for examining overall time averaged body forces, and can predict (to some degree of accuracy) the presence and size of separation bubbles. However, to accurately compute the transient behaviour of these flow structures at a fine scale and at relatively high frequencies substantially increase the computational power required owing to fine mesh sizes required to capture complex near-wall flow structures. Including fine-scale free-stream turbulence as an input condition results in a increase in problem complexity. It is not yet feasible to solve such complex problems within a reasonable timeframe with available computational resources at the time of writing; for such problems, experimental techniques remain the most effective method of investigation. The additional necessity of having a physical model with which to validate computational results adds further credence to an experimental investigation.

1.3 Atmospheric Turbulence and the Atmospheric Boundary Layer (ABL)

The Earth's atmosphere is a complex system extending from the surface to approximately 100 km altitude. Meteorologists categorise the atmosphere into distinct layers based on variations in properties including (but not limited to) temperature laps rate.

The layer closest to the earth and extending to approximately 10 km is called the *troposphere*. Above the troposphere are the *tropapause*, *stratosphere* and *ionosphere*. The troposphere contains all events experienced as weather, the bulk of moisture in the atmosphere, the surface and upper level winds and jet-streams. Winds are defined as large-scale movements of air from regions of (local) high to low pressure, whose motion is compounded by the Earth's rotation resulting in spiral motions across the surface, known as the Coriolis effect. Stull (1988) describes several "sub-layers" within the troposphere, defined by night-to-day variation of the thermal mixing layer close to the surface. The region close to the ground is referred to as the Atmospheric Boundary Layer (ABL), and the remaining atmosphere above it the free atmosphere (Figure 1.15).

Atmospheric scientists (Garratt 1992, Stull 1988) define the ABL as the layer of air directly about the Earth's surface where the effects of friction, heating and cooling act in timescales less than a day. The exact thickness and behaviour of the ABL is dependant on a number of prevailing conditions including (primarily, but not limited to) winds, cloud cover, time of day or night and seasonal variations. During the day and over land, the top of the ABL is most easily identified from an atmospheric temperature sounding and is recognised by a change in temperature - usually a sharp increase - known as a *inversion*, which prevents thermal currents from rising above this level.

It is noted by Garratt (1992) that the ABL bears many similarities to more commonly studied two-dimensional turbulent boundary layers. As with conventional boundary layers, the ABL can

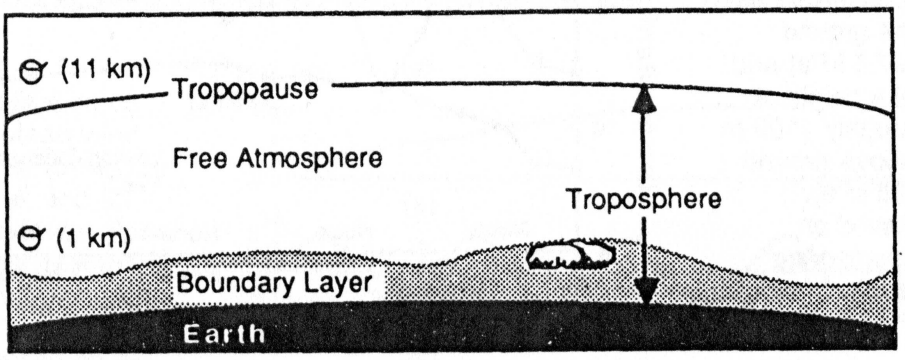

Figure 1.15: Structure of the troposphere containing the ABL and the free atmosphere above it (Stull 1988)

be further defined into sub-layers, each possessing unique characteristics including key turbulence structures within. Garratt (1992) presents three sub-layers within the ABL in Figure 1.18:

- The *outer layer* has little or no dependence on the surface below, which is dominated by the Coriolis forces owing to the Earth's rotation. These forces combined with variations in surface temperature and moisture content are responsible for large scale atmospheric disturbances or weather systems. The effects of the Earth's rotation on the motion of flows in the ocean and atmosphere was studied by Ekman (1905), hence this layer sometimes bears his name.
- The *inner layer*, also referred to as the surface layer is directly affected by surface features such as terrain type and roughness (hills, mountains, etc).
- The *surface layer* extends to just above surface roughness elements (for example buildings and trees), and is dominated by mechanical mixing from the wakes of these objects upstream.

Of these it is the surface layer which is of primary interest to the study of MAVs and small aircraft which operate close to the ground. While large scale weather systems have a dramatic effect on the flow patterns found within the surface layer, this effect is primarily though the presence of atmospheric winds.

1.3.1 The Surface Layer (Roughness Zone)

The atmospheric wind environment near the surface has been been studied in detail over much of the past century by wind engineers performing large scale studies for the purposes of predicting the loading on large structures such as buildings and bridges, as well as pollutant dispersion (Holmes 2001, Lawson 1980, Sutton 1953, Van der Hoven 1957) although generally at much larger scales, both temporary and spatially than are desirable for MAV work.

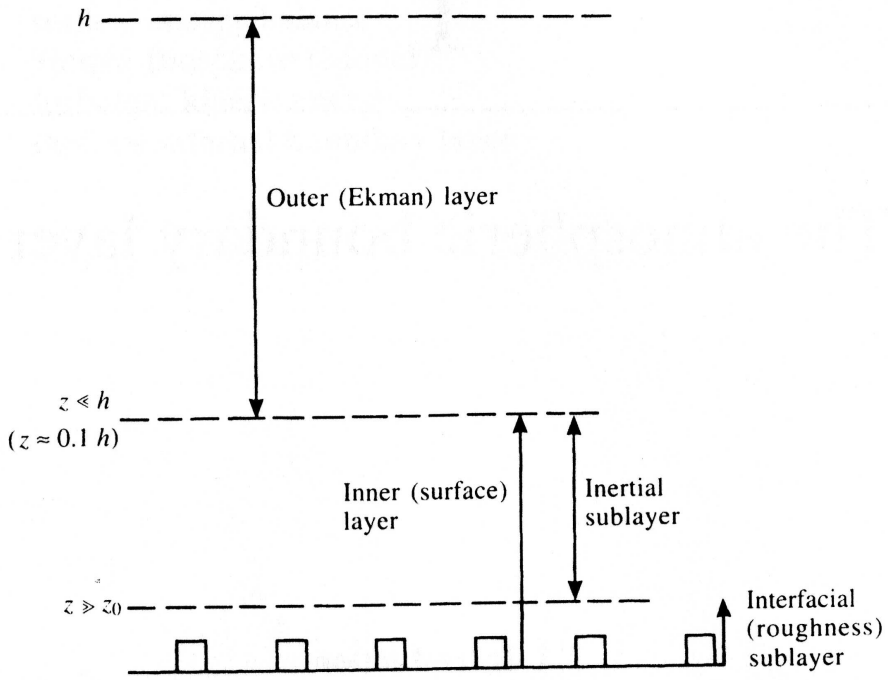

Figure 1.16: Three sub-layers with in the ABL as defined by Garratt (1992), the outer layer, the inner layer and the surface layer

1.3.1.1 Turbulence in Atmospheric Flows in the Roughness Zone

Etkin (1981) describes atmospheric turbulence being composed of *discrete gust inputs* and *random continuous turbulence*. Discreet gusts are isolated encounters with steep gradients, such as the edge of convective disturbances or in the wake of a large object. Random continuous disturbances are chaotic motions of air amenable to statistical characterisation; Etkin suggests measures of stationarity, homogeneity, isotropy, time and distance scales, and correlations and spectra. Statistical methods used for the description and analysis of turbulent flows are discussed in detail in Chapter 2 of this thesis, and will not be discussed here in the interest of brevity.

Atmospheric wind turbulence may vary with many parameters, including (but not limited to) time, terrain type and height above the ground. The mean velocity profile as a function of height above ground is often modelled by a power law profile, varying with terrain type. Walshe et al. (1964) studied the roughness zone as a turbulent boundary layer, categorising boundary layer thickness changes with terrain roughness from data acquired from a 500 m instrumented tower (Figure 1.17).

The mean velocity profile for the lower 300 m of the ABL can be represented by the logarithmic profile in Equation 1.3, where z is height above the ground, z_o a surface roughness parameter and δ the depth of the boundary layer. Values of surface roughness based on terrain type were developed

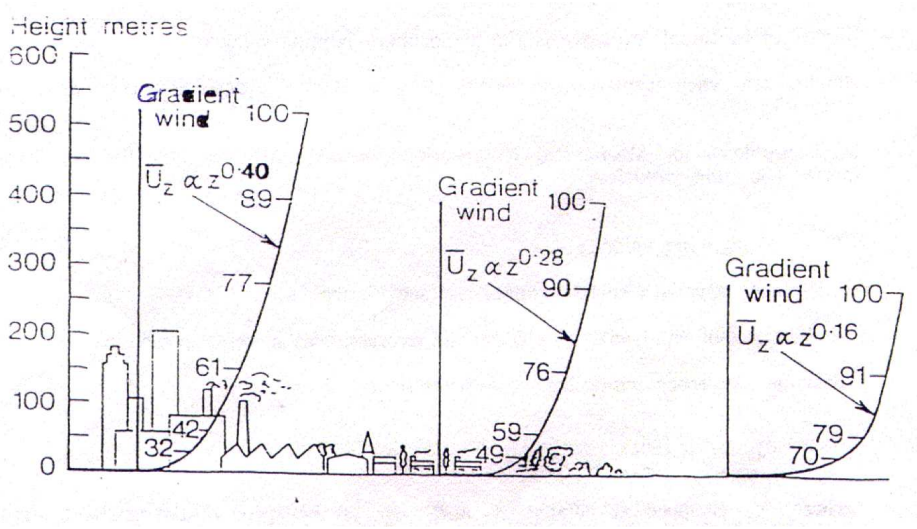

Figure 1.17: Logarithmic boundary layer profiles as a function of surface roughness (Walshe et al. 1964)

by Davenport (1960) and later refined by Wieringa (1992), proposing a classification scheme for categorising terrain types based on density and size of roughness elements (trees and buildings) upstream in addition to large scale undulations and hills. Details of this classification scheme are discussed in Appendix A, and are used later in this work.

$$\frac{U(z)}{U(\delta)} = \frac{ln(\frac{z+z_o}{z_o})}{ln(\frac{\delta}{z_o})} \tag{1.3}$$

The velocity profiles produced by a power law and shown in Figure 1.17 were suggested to be an over-simplification by Cooper and Watkins (2007), warning that the fitting of power laws should be used with caution in all but open smooth terrain: velocity profiles in the lower 300 m of the ABL were shown to be highly dependant on surface roughness, for which Cooper and Watkins noted a lack of information. The profile produced by Equation 1.3 is thus rendered applicable only in open terrain.

The level of turbulence in the flow is characterised by a set of statistical turbulence parameters, detailed in Chapter 2. Two of the most commonly used parameters are:

- Turbulence intensity ($I_x = \frac{\sigma_U}{Uref}, I_y = \frac{\sigma_V}{Uref}, I_z = \frac{\sigma_W}{Uref}$), being the ratio of the standard deviation of fluctuation in the velocity component normalised by mean wind speed where U, V, W are (respectively) longitudinal, lateral and vertical velocity components.
- Integral length scale (L_{ij}) where $i = x, y, z$ and $j = u, v, w$, defining the largest size of any turbulent eddy or gust present in the flow.

As with the mean velocity profile, turbulence intensity predictions (as a function of height) are difficult. Empirical predictions based on scaled logarithmic functions provide a reasonable estimation for heights away from the local effects of upstream roughness elements. Such estimations - commonly used by wind engineers - are provided by the The Engineering Science Data Unit (ESDU) in the form of reference data sheets (Anon 1976a) and (Anon 1976a), in addition to work by Teunissen (1980), whose theoretical profiles of turbulence intensity (as a function of height, based on a logarithmic approximation of the wind profile) for different terrain types are presented in Figure 1.18.

Cooper and Watkins (2007) describes a wealth of information on velocity spectra for atmospheric flows; however, it is pointed out that the majority of the data are concerned with large time scales and relatively large distances above the ground (300-1500 m) in thermally stable boundary layers. An example of a energy spectrum over a large timeframe by Van der Hoven (1957) is shown in Figure 1.19, showing a low frequency peak at approximately 4 days, likely corresponding to the passage of large scale weather system. At higher frequencies a second peak was identified at approximately 1 minute (1/60 Hz), likely the mechanical turbulence present in the wind. However, it is noted by the author that these data, taken at a height of 60 m using large scale instruments over long time frames, lacks the resolution to observe further peaks at higher frequencies. Between the two spectral peaks in Figure 1.19 is what is referred to by Van der Hoven as a "spectral gap", observed to be independent of local terrain conditions.

1.3.1.2 Measurement of Turbulence in the Surface Layer

There is a wealth of experimental wind data in the ABL over the past century by wind engineers and atmospheric scientists (Milbank et al. 2005). Wind data are traditionally obtained utilising propeller, cup, dynes or ultrasonic anemometers placed either in isolation or located on vertical masts with inter-device spacing of several metres. This reflects the interest of the building or road vehicle aerodynamics communities where the structures or vehicles are relatively large in relation to the turbulence scale being measured; however, they are much larger than the scales of interest for the operation of MAVs, and in many cases these instruments are larger than the MAVs themselves.

The data from the closest spacing of anemometers (2 m) appears to be Flay (1978), which is subsequently used as the basis of ESDU data sheet 85020. The size of individual anemometers used was similar to the size of MAVs (in common with nearly all meteorological surveys), and therefore unable to provide the spatial resolution needed to discriminate the turbulence characteristics relevant to MAVs. The vertical configuration was similar to that of meteorological instruments used to provide information as a function of distance from the ground.

Watkins (1990) made a number of measurements of atmospheric turbulence at low level for the purposes of understanding the effect of turbulence on the aerodynamics of road vehicles. Measurements were made using a set of small hot wire anemometers fixed to the roof of a moving vehicle at a height of 3.9 m above the road while driving on the open road under a range of wind conditions. By using small scale instruments at low level and a data acquisition system capable of acquiring data at

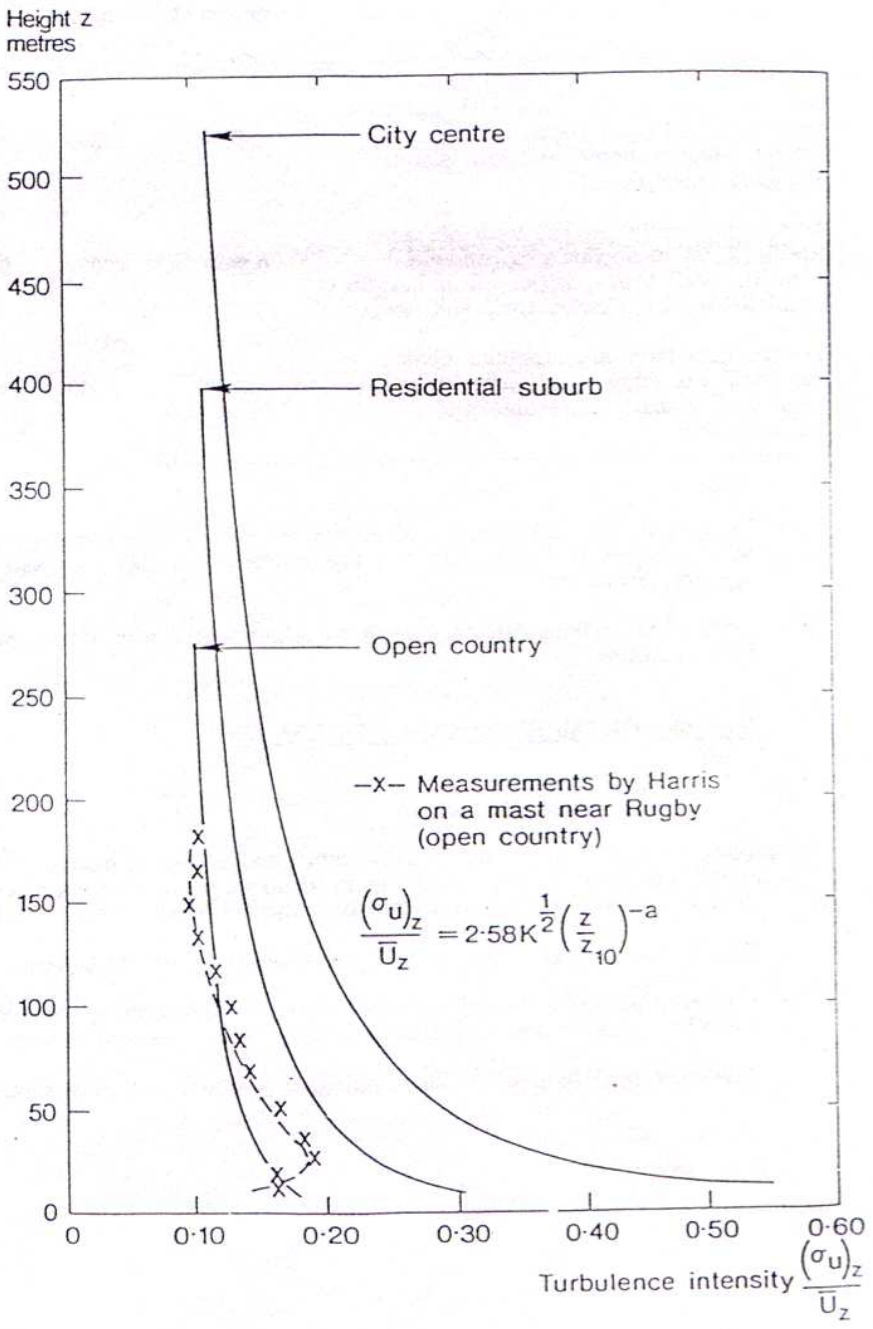

Figure 1.18: Turbulence intensity in the surface wind as a function of height and surface roughness (Teunissen 1980)

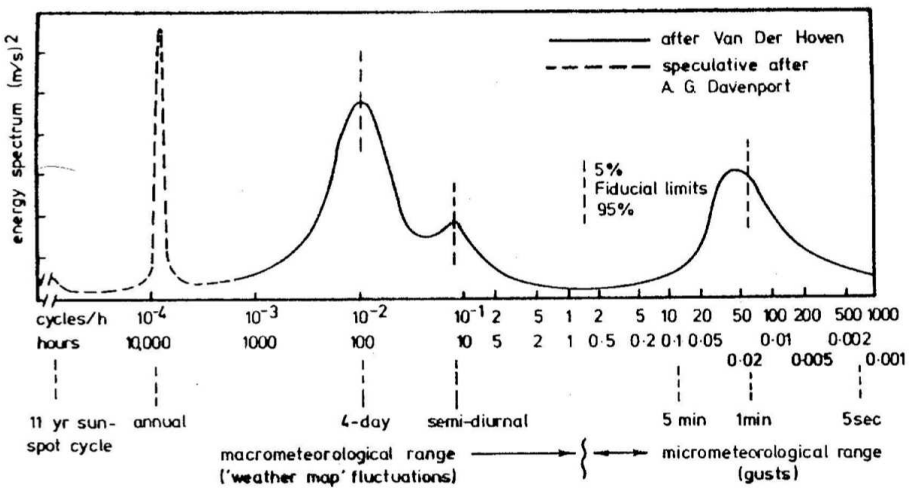

Figure 1.19: Long term spectral energy of surface winds (Van der Hoven 1957)

high frequency, Watkins attempted to contribute high-frequency data to trends acquired by Van der Hoven (1957) and Flay (1978), and to test the accuracy of empirical predictions in data sheets by ESDU in common use. In Figure 1.20 experimentally acquired data is compared to the theoretical prediction; Watkins (1990) concluded that observed differences were due to a low estimation of the variance in the signal. Once a correction was applied the data matched the theoretical result well (Figure 1.21).

Watkins (1990) identified temperature drift as a key limitation of hot-wire anemometers, in addition to the propensity of wires to break easily when struck by airborne debris commonly encountered on road. A later set of experimental measurements by Watkins et al. (2006) measured the turbulence levels in the ABL by mounting a bank of high frequency multi-hole pressure probes (Hooper and Musgrove 1997, Watkins 2003) to a mast on a car roof, 4 m above the road and "flying" them through the atmosphere in a range of different wind speeds and and terrains. The use of the multi-hole pressure probes overcame the limitations associated with the previous anemometers, giving robust acquisition of high-frequency, small-scale turbulent structures. This work formed the basis of the work performed in this thesis and described in Chapter 3.

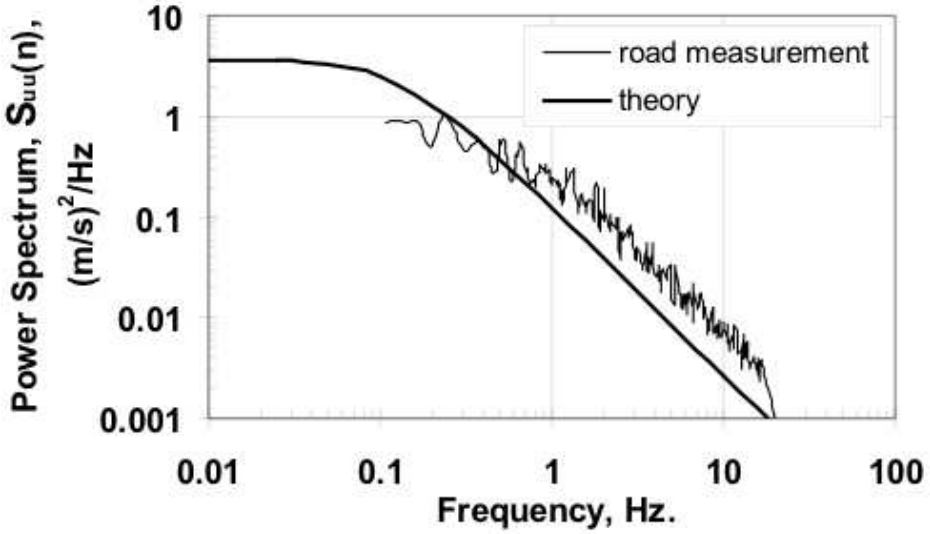

Figure 1.20: Longitudinal power spectra for a vehicle moving through a 7.15 m/s wind in smooth terrain (Cooper and Watkins 2007)

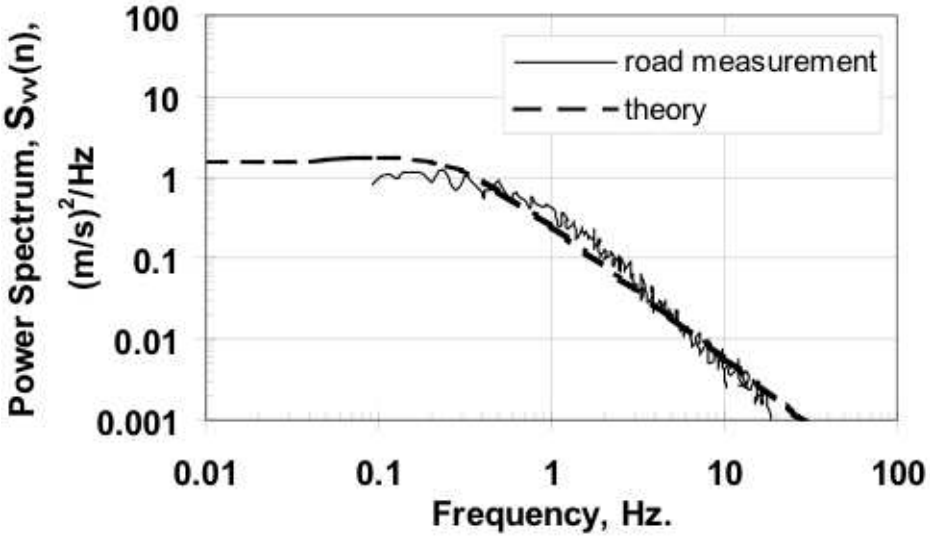

Figure 1.21: Longitudinal power spectra for a vehicle moving through a 7.15 m/s wind in smooth terrain (Cooper and Watkins 2007) with corrections for variation distortion applied

1.3.2 Experimental and Computational Simulation of Atmospheric Turbulence

The majority of work to date on turbulent and unsteady atmospheric flows has been performed using experimental techniques. Due to the high operating and setup costs as well as long lead times associated with experimental work, there has been increasing interest in Computational Fluid Dynamic methods (CFD methods) to simulate such flows. Such simulations are in development and used increasingly; notable examples include Uchida and Ohya (2003), Gosman (1999). A useful but dated review by Murakami (1998) highlights the difficulties in applying CFD to these complex flows, citing large computational times and high mesh densities required to achieve accurate solutions. Recent advances in computing power – at accessible cost – have rendered direct simulation of at least larger turbulent structures to be on occasion feasible on large-scale, "clustered" hardware installations.

Computational resources of sufficient capacity to render sufficient throughput were unavailable for this work, rendering the assessments presented herein experimental.

1.4 Conclusions

After reviewing the relevant literature the following key conclusions are drawn:

1. The development of MAV technology through significant advances in materials, miniaturisation of electronics and sensors (largely through the use of MEMS) and the improvement in high energy density batteries has reached a point where operational MAVs are technically feasible. However, aerodynamic challenges with respect to their operation in the turbulent environments where their operation is desired remains a great challenge.
2. At low Re, and particularly for low AR wings, there is limited research into and understanding of fundamental flow phenomena. It is clear from works reviewed, that aerodynamic performance is reduced in both counts. It is also noted, that despite most experimental works using sophisticated measurement equipment, results are typically analysed in time-averaged contexts, providing little information of transient behaviours in turbulent environments.
3. At low Re the laminar separation bubble on the suction surface of small airfoils dominates the flow field, causing a reduction in the performance on lifting surfaces. A significant amount of research exists on the behaviour of this separation bubble; however, its formation, bursting behaviour and sensitivity to free-stream turbulence variations (particularly with reference to high turbulence levels, relevant to outdoor flows) remains poorly understood.
4. Atmospheric turbulence levels near the ground have been studied extensively to better understand the flows around buildings, plant canopies and large geographic regions to aid design of civil structures and to deconstruct pollutant dispersion. Work seeking to characterise frequency content was carried out initially using relatively large instruments and with insufficient resolution to analyse small scales relevant to MAVs. More recently, advances in instrumentation have allowed necessary acquisition and characterisation of small-scale turbulent flows, highlighting shortcomings in classical works.

1.5 Research Goals and Objectives

The literature review highlights two areas of significance where contributions may usefully further the understanding of MAV flight:

1. The flight environment of small aircraft within the ABL is not well documented nor understood at relevant scales. The current body of knowledge contains significant work characterising the ABL on a mesoscale and at scales relevant to wind engineering and road vehicles. Within this, further knowledge is required to better elucidate sensitivity to terrain effects.
2. The effects of turbulence on aerodynamic performance is not well understood, particularly with respect to the behaviour of the boundary layer and laminar separation bubble existing at low

Re. It is likely that turbulent eddies approaching MAVs in flight induce significant variations in incidence on lifting surfaces. The frequency and magnitude of these disturbances depend on vehicle mass, flight speed, and the size and structure of the turbulence in airflow. The effect of these disturbances on the boundary layer, and on the behaviour of flow separation present at low *Re* is not documented nor understood.

Contributions to the understanding in these areas may be afforded by a series of measurements made outdoors and then in a suitably setup wind tunnel experiment aimed at reproducing relevant flows. The proposed investigations aim to:

1. Measure turbulence levels in the atmosphere near the ground in a range of different terrains and wind conditions at scales relevant to MAV flight.
2. Setup wind tunnel experiments to reproduce the most relevant scales and intensities of turbulence for the purpose of investigating the effects of turbulence on MAVs .
3. Investigate, using established methods, the effect of turbulence levels on a simple MAV geometry, focusing particularly on the aerodynamic performance of the wing and the behaviour and influence of the laminar separation bubble on the suction surface.

1.6 Thesis Layout

This thesis contains the following sections:

- Chapter 2 presents the required background information on turbulence modelling and statistical methods. The sign conventions and force and moment signs that will be used for the remainder of this thesis are also presented.
- Chapter 3 describes the process of measuring the small scale turbulence levels present in the atmosphere under a range of wind conditions and terrain environments.
- Chapter 4 presents a detailed description of the methods and equipment used in the wind tunnel investigation including models, instrumentation and their capabilities and limitations.
- Chapter 5 details the results obtained from the surface pressure on a flat plate wing at low Re in replicated atmospheric turbulence in the wind tunnel.
- Chapter 6 examines the effect of the turbulence on the external flow field around a wing through the use of smoke and surface oil flow visualisation.
- Chapter 7 presents the key conclusions from this work, and discusses their significance and gives a overview of possible extensions to this work in future projects,
- Appendices A-C provide relevant background information as required.

Chapter 2

Theory of Turbulence Relevant to MAV Flight

To study the effects of atmospheric turbulence on MAVs and present a commentary on the results, it is necessary to introduce terminology and analysis techniques used in this thesis to characterise atmospheric flows. Methods of analysis have been developed and used in the fields of wind engineering and meteorology, much of which are typically unfamiliar to the aerospace researcher. Prior work in understanding relevant complex turbulent flows is presented in Chapter 1; readers seeking a more detailed deconstruction of such flows are referred to original sources including such as Panofsky and Dutton (1976), Townsend (1976) and summaries in datasheets by ESDU (Anon 1976a; 1991).

This chapter presents a basic definition of turbulence and common analytical methods applied throughout this work. Further information on atmospheric turbulence modelling are the works of Stull (1988) and Nieuwstadt and van Dop (1981). Details on the mathematical algorithms of the techniques used in this work are presented in relevant appendixes.

2.1 Axis Systems and Frames of Reference

A common frame of reference is defined for the work presented, describing the motion of fluids and bodies and the magnitude and direction of forces acting on them. Three commonly used Cartesian reference frames (or axis systems) are:

- *The Earth axis system* which uses the Earth's surface as a frame of reference (assuming the observer is close enough to the surface, and moving sufficiently slowly that the horizon can be approximated as a straight line and the surface as flat). This system is defined as having the

lateral (x, the direction of travel) and longitudinal (y) axis along the surface, and the vertical axis (z) normal to it (positive downward). A key convenience of this system concerns gravity always acting along the vertical axis. It is less convenient; however, for describing vehicle motion, or motion of a fluid relative to a vehicle.

- *The body axis system* is fixed to a vehicle or rigid body, moving with it. Convention has the longitudinal (x) axis in the forward direction, the lateral (y) axis to the right and the vertical (z) axis in the positive downward direction, known as a"right hand" axis system (illustrated in Figure 2.1). Body axis systems are used when studying vehicle dynamics as the inertial products are zero, thus simplifying the equations of motion.

- *The wind axis system* has the principle axis aligned with the mean wind, with the longitudinal (x) direction aligned positive with the mean flow - rather than the body - the lateral (y) axis to the right and vertical (z) axis positive down as with the body axis system.

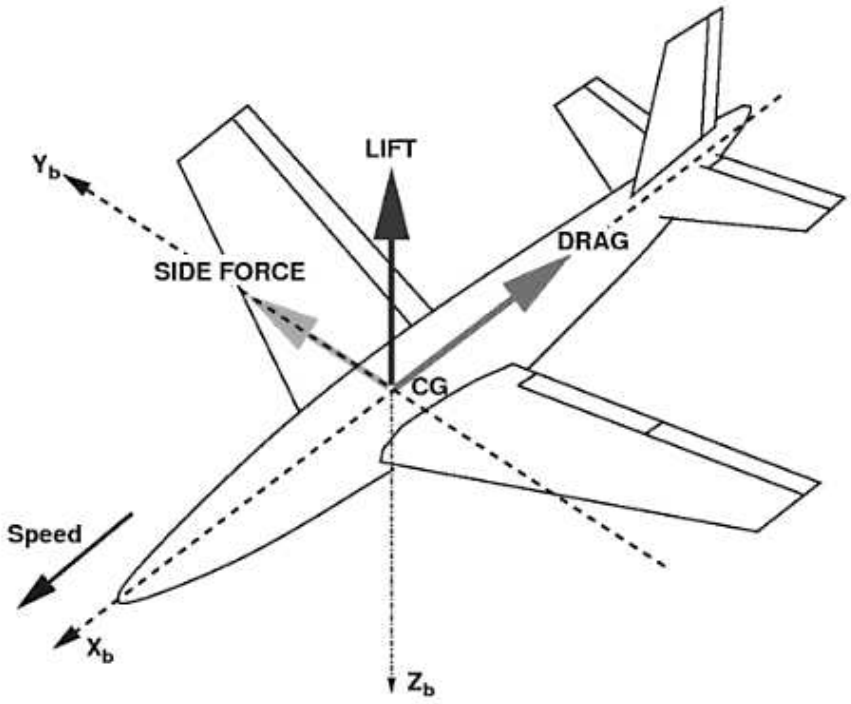

Figure 2.1: Body axis system (Filippone 2006)

Sign convention dictates the direction of positive rotation in a right hand axis system is given by the "right hand rule"; for the body axis system described above, positive moments are counter-clockwise when viewing along the axis in the positive direction (Figure 2.2).

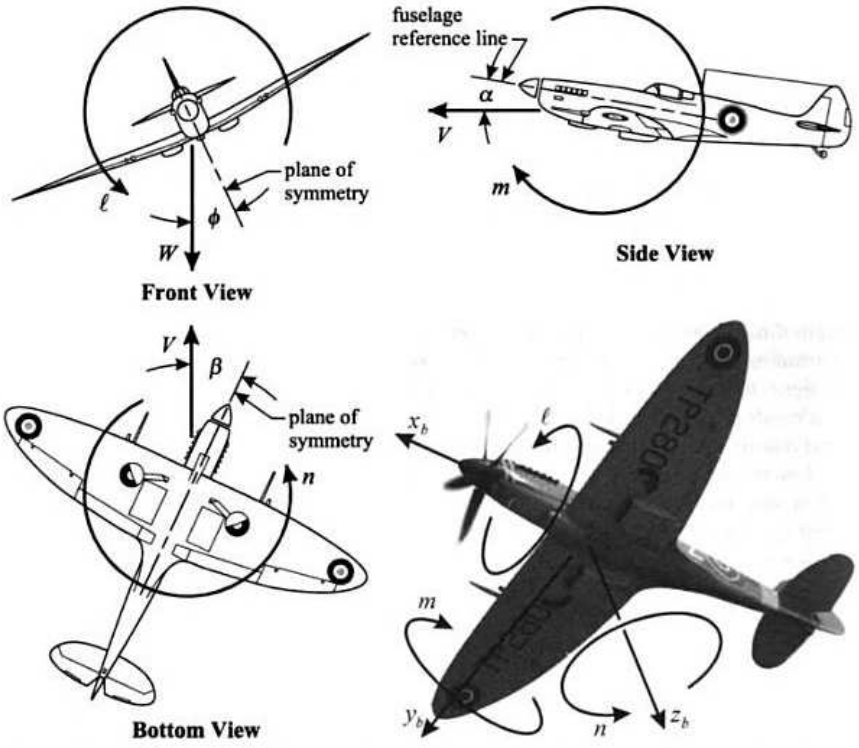

Figure 2.2: Sign convention for forces and moments (Phillips 2004)

The aerodynamic forces acting on a body (of which lift is the vertical component) are primarily dependant on the incidence (or pitch) angle between the mean flow direction and the body (α). Side force acts in the lateral direction in the wind axis system, and is dependant on sideslip, or yaw (β, Figure 2.2).

2.2 Analysis of Turbulent Flows

Turbulent flows can be visualised as flow fields consisting of a collection of turbulent eddies of varying sizes moving with the mean flow. Much of the kinetic energy in the flow is contained in the eddies, dissipated slowly over time due to internal viscous forces within the fluid. The nature of turbulent flows have been reviewed in Chapter 1 and in relevant referenced works. Whilst detailed physical analysis and prediction of the flow is difficult (in many cases impossible), the general nature of turbulent flows can be analysed using a combination of statistical methods and spectral analysis, allowing their categorisation and comparison.

The methods of analysis presented here are suitable for flows where the turbulence can be considered homogeneous and isotropic in nature. In the case of atmospheric flows which are of interest in

this thesis, this is rare; most ABL flows are dominated by local effects such as wakes, thermal effects and gusts. For this work, analysis of such flows is based on samples taken away from these effects such that they closely approximate homogeneous flows, although are generally not isotropic. Analysis of flows containing local wakes is the subject of a preliminary study by Watkins et al. (2008); however, such flows are outside the scope of this thesis.

2.2.1 Taylor's "Frozen Flow" Hypothesis

Whilst time-dependent, direct measurements of eddy size and energy content are desirable in characterising a complete turbulent flow field, such measurements are practically unfeasible. Taylor proposed that in some cases, the turbulence could be thought of as frozen in time as it moves past a fixed point (such as a sensor, illustrated in Figure 2.3). Instead of measuring many different points in the flow field at one time, a continuous measurement at a single point can thus be made over a large sample time, t, and the properties of the whole flow field extrapolated if considered to be unchanging over the sample time.

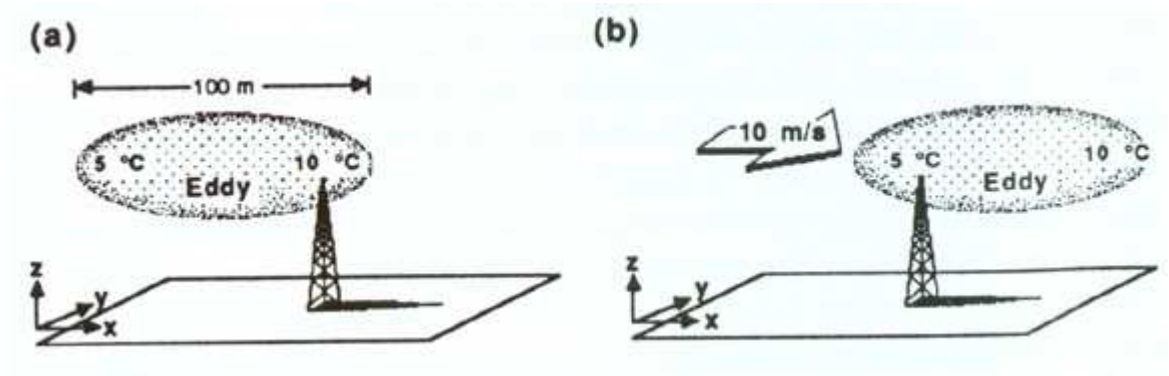

Figure 2.3: Illustration of a turbulent structure moving past a sensor unchanged over time (Stull 1988)

This simplification may only be considered practical when the evolutionary period of the turbulent structures within the flow are significantly greater than the time taken for them to pass the sensor. Subsequently, limitations are encountered in highly irregular flows, or in flows where turbulence intensity is very high. Willis and Deardorff (1976) suggest that Taylor's method is only valid when the standard deviation of the fluctuation in the mean wind speed is less than half the mean wind speed (Equation 2.1).

$$\sigma_{V_M} < 0.5 V_w \tag{2.1}$$

2.2.2 Analysis of Turbulence in the Time Domain

Statistical analysis is used extensively throughout this work in analysing the properties of atmospheric flows, and in comparisons to those generated in the wind tunnel (Chapter 3, p. 48). Like any statistical study, the accuracy of the result is dependant on the sample length (t) required to obtain a result that captures all the significant periodic events in the flow. Long time records are preferable, though in outdoor measurements sample sizes are often limited by practicalities in data storage and environmental conditions. Van der Hoven (1957) measured the wind-speed spectrum (Figure 1.19) and observed a spectral gap separating "micro" (short scale events such as local gusting and turbulence) and "macro" events (large weather driven fluctuations). The macro scale events occur over hours and days and could be considered as quasi-static for any vehicle flying in the atmosphere, which are primarily effected by short scale events. It is noteworthy that these measurements were made at a hight of 100 m above the ground, which is higher then many small vehicles are envisaged to operate.

2.2.2.1 Flow Field Properties

The flow field at a single point can be described by a mean velocity ($\overline{U}$) in the principle axis in the wind axis system. The magnitude and direction of the flow velocity fluctuates with time; the instantaneous velocity components in the longitudinal, lateral and vertical directions are given by u', v' and w' respectively.

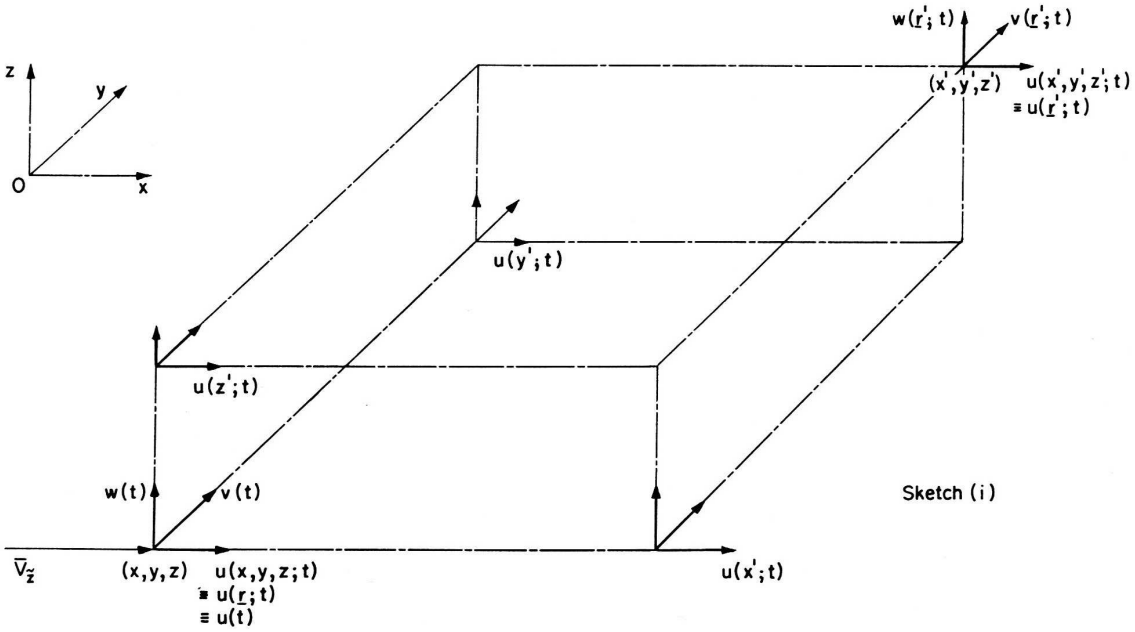

Figure 2.4: Control volume from ESDU datasheet (Anon 1976a)

In a turbulent flow field, the velocity components, measured at a single point fluctuate as turbulent eddies move past, therefore two measurements at the same point separated by a time interval, τ, will have different velocities. Similarly, two measurements taken at two points laterally separated by a distance y' at the same time also have different velocity components. The result is that the flow within a volume (Figure 2.4) shows different properties at different points within the control volume at the same instant in time, and the properties at each point vary with time. Statistical and dynamic analyses characterises these changes both at the one point and between different points, describing the flow field.

2.2.2.2 Statistical Analysis

Statistical functions including means, standard deviations, probability density functions and distributions are used to describe the broad characteristics of the turbulence over an observed time period.

For atmospheric winds the mean wind speed $\overline{U}$ is given by:

$$\overline{U} = \frac{1}{T}\int_{t=0}^{t=T} u' dt \tag{2.2}$$

Where T is the length of the sample. The instantaneous velocity at any point is a vector quantity comparing the wind speed and the fluctuating components in all three directions:

$$\left[\{\overline{U} + u'\}^2 + v'^2 + w'^2\right]^{\frac{1}{2}} \tag{2.3}$$

2.2.2.3 Turbulence Intensity

A measure of the magnitude of the fluctuation is given by the standard deviation of the fluctuation components u', v' and w', expressed as $\sqrt{\overline{u(t)'^2}}$, $\sqrt{\overline{v(t)'^2}}$, and $\sqrt{\overline{w(t)'^2}}$. The standard deviation of each component can be non-dimensionalised by dividing by the mean velocity $\overline{U}$ to give terms called *turbulence intensities* (commonly used in the field of wind engineering). Since a turbulence intensity includes a mean flow speed, its magnitude is relative to the point of measurement (which may be moving relative to the ground). I_i is used to denote the turbulence intensity in atmospheric wind or in a wind tunnel relative to the ground. It should be noted that whilst when measured relative to a point moving with respect to the ground, it is denoted by J_i, described in further detail later later.

$$I_i = \frac{\sqrt{\overline{i'^2}}}{\overline{V_w}} \text{ where i can be u, v or w} \tag{2.4}$$

2.2.2.4 Reynolds Stress

If one considers a turbulent flow where as an eddy passes through a control volume, different velocities act on different sides of the volume. The effect on the momentum flux within the volume is analogous to applying a force on a cube, wherein deformation of the fluid control volume occurs. Just as a difference in forces and resulting deformation results in a stress within a material, a difference in momentum flux within a control volume acts as a stress in a fluid, and is called *Reynolds stress* (Stull 1988). However, it should be noted that although Reynolds stress acts akin to a stress, it is not a true stress as it does not have the units of $\frac{\text{force}}{\text{area}}$.

To define Reynolds stress mathematically, consider air moving upwards in the z direction with a velocity component w' being mixed into the cube at a rate of u': the magnitude of the stress, or momentum flux component is thus $|\overline{u'w'}|$. If a single side of the control volume is considered, then there are three possible stresses given by $\overline{u'u'}$, $\overline{u'v'}$ and $\overline{u'w'}$. A complete matrix of stresses is given in Equation 2.5:

$$\tau_{Re} = \begin{bmatrix} \overline{u'u'} & \overline{u'v'} & \overline{u'w'} \\ \overline{v'u'} & \overline{v'v'} & \overline{v'w'} \\ \overline{w'u'} & \overline{w'v'} & \overline{w'w'} \end{bmatrix} \tag{2.5}$$

In can be recognised that $\overline{u'w'} = \overline{w'u'}$, reducing the number of Reynolds stress terms to six (Equation 2.6):

$$\tau_{Re} = \begin{bmatrix} \overline{u'u'} & \overline{u'v'} \\ \overline{v'v'} & \overline{v'w'} \\ \overline{w'u'} & \overline{w'w'} \end{bmatrix} \tag{2.6}$$

2.2.2.5 Viscous Stress

Viscous stress concerns the shearing motion in the fluid between areas of different velocity, such as in a boundary layer, or at the boundary of a jet. Shear stress is due to the forces between fluid particles at the molecular level. Viscous stress can be laminar (for example a laminar boundary layer) or turbulent. A measure of the viscous stress in a fluid is the viscosity of the fluid (μ). As with Reynolds stress, the viscous stress matrix is symmetric resulting in six possible terms.

2.2.3 Analysis in the Frequency Domain

A time signal is analysed in the frequency domain by taking the Fourier transform of the signal and presenting it as frequency spectra. In the case of atmospheric flows, the apparent frequency of an occurrence measured at a point is dependant on the mean wind speed, for example the mean advection velocity of eddies past the sensor. In some circumstances it is desirable to analyse the frequency content of the signal independent of velocity. By dividing the frequency by velocity ($f/\overline{U}$), the result is a reduced frequency (k), referred to as *wave number*. Further information on signal processing are provided in Appendix C.

2.2.3.1 Turbulence Spectra

Spectra show the distribution of turbulent energy in the frequency domain. They are commonly presented as Power Spectral Densities (PSDs) which give the power of the signal at any given frequency. A signal in the time domain transposed into the frequency domain using Welche's method, illustrated in Figure 2.5, showing spectral peaks corresponding to the frequency components present in the signal.

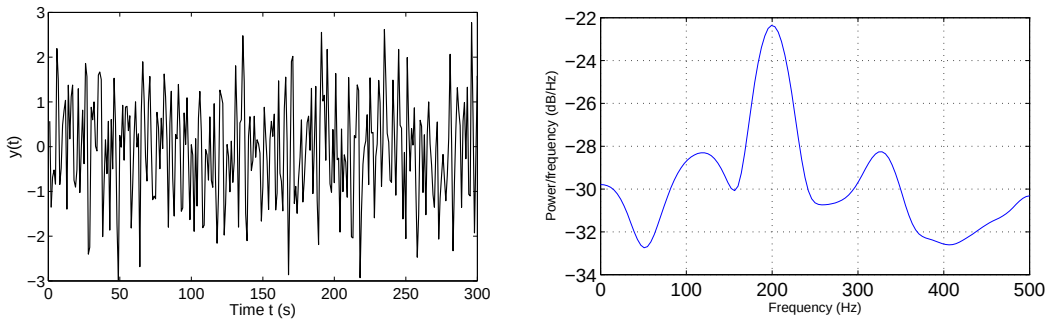

(a) Signal in the time domain

(b) Signal in the frequency domain

Figure 2.5: Signal conversion from time to frequency domain via Welche's method (Proakis and Manolakis 1996)

Welche's method is an averaging method where a signal is divided into blocks of known width. The Fourier transform is taken for each bin, and the result is averaged to give the spectra. Benefits of Welche's method are smoother spectra and the removal of anomalies in the data that arise from sampling errors and spectral leakage (further details are presented in Appendix C); however, the sample size must be sufficiently large to provide for statistically significant averaging whilst still maintaining a sufficiently large bin size for adequate frequency resolution.

2.2.3.2 Energy Cascade and Kolmogorov Hypothesis

Most of the energy in a turbulent flow is contained in the larger scale structures, with progressively less energy in smaller eddies. This concept of an *energy cascade* was introduced by Kolmogorov (1961), who theorised that the kinetic energy in a turbulent flow is introduced by the largest scales (associated with the characteristic length scale in the flow as described above) and is transferred to the progressively smaller scales until at the smallest scales the energy is dissipated through viscous motion and released as heat.

Kolmogorov further showed that the energy is spread in the spectrum within the inertial range, dissipating with a $-\frac{5}{3}$ slope with increasing frequency. This slope has been proven to be accurate through later studies, which is consistent with the hypothesis that the majority of the energy exists in the larger scales.

2.2.4 Characteristic Length Scales

One method for describing turbulent flow concerns a collection of turbulent motions or eddies of different sizes. Each size eddy can be visualised as a single turbulent motion confined within a volume of size l. A length scale term is used to describe the characteristic length or turbulent eddy size in a flow; work by Kolmogorov notes the largest eddy sizes - containing the most energy - to be dominant. In the case of atmospheric flows, the length scale can represent the characteristic size of a gust, which is a large, sometimes periodic deviation from the mean wind speed that exists on a macro scale, rather than an analysis of the micro scale mixing that may be commonly associated with the study of turbulence. Therefore once the largest eddy size and its strength is identified, the energy of all smaller eddies can be deduced from the $-\frac{5}{3}$ slope identified by Kolmogorov. This makes the *characteristic length scale* a useful quantity for characterising the flow. A number of techniques are available for determining the characteristic length scale, with the two major methods being by *auto-correlation* method and by *best fit*.

2.2.4.1 Auto-correlation Method

The auto-correlation methods assumes Taylors frozen turbulence approximation where the constant mean velocity is large with respect to the turbulence fluctuations, thus the eddies do not change appreciably as they pass a given point. The signal measured at this point is compared to a time-delayed (by τ) version of itself. This is known as *auto-covariance*, and provides information on how the fluctuation in mean velocity varies with time. Normalising the auto-covariance by the variance (σ_u^2) gives the auto-correlation $R(\tau)$(Pope 2000).

$$R(\tau) = \frac{\overline{u(t) - u(t+\tau)}}{\sigma_u^2} \tag{2.7}$$

Length scales are thus given by the area under the auto-correlation function ($R(\tau)$). Equation 2.9 gives the length scale function for the longitudinal length scale (L_x), where c is the first zero crossing of the auto-correlation coefficient function ρ_u.

$$L_x = V \int_0^c \rho_u(s).ds \tag{2.8}$$

$$\rho_{uu}(\tau) = \frac{\lim_{x\to\infty} \frac{1}{T} \int_0^T \{u(t) - \overline{u}\}\{u(t+\tau) - \overline{u}\}dt}{(\sigma_u)^2} \tag{2.9}$$

The corresponding longitudinal length scales for the y and z axes, L_y and L_z can be calculated by respectively substituting v or w for u in the above equations. Auto-correlation methods are advantageous as they provide a good result over widely fluctuating signals; however, they require a very long sample length to gain sufficient data to be able to take a reliable average. For flow measurements (for example on-road testing) where the acquisition of a large sample is inherently difficult, length scales determined via this method may give unreliable results. Further details concerning this method are provided in Appendix C.

2.2.4.2 Method of Best Fit by Comparison

Alternately, measured data may be fitted to existing theory via regression. A number of existing theories exist that predict the length scales present in a flow. Two such theories by von Karman and Kauma have particular relevance to atmospheric flow and are provided in the data sheets by ESDU (Anon 1991) and shown in Equation 2.10. The modelling of low frequency gusts may be emphasised with the best fit approach, while the high frequency components converge to Kolmogorov's law. ESDU (Anon 1991) provides standard spectral functions that can be fitted to the data where the peak can be estimated:

$$L_x = \frac{0.146\overline{U_z}}{n_p}, L_y = \frac{0.1066\overline{U_z}}{n_p}, L_z = \frac{0.106\overline{U_z}}{n_p} \tag{2.10}$$

Where n_p is the frequency at which the peak occurs. Characteristic length scale is thus calculated as a function of this and mean velocity.

2.3 Turbulence Experienced by a Flying Vehicle

An aircraft in flight experiences turbulence in the flow field relative to its motion. For a sensor fixed to the ground, the turbulent flow field moves past the sensor at the mean wind speed ($\overline{V_w}$). For an aircraft in free flight, the flow field moves past the vehicle at the mean flight speed (V_f), which is independent of wind speed. Analysis therefore becomes relative to the aircraft and the aircraft's airspeed V_f replacing the mean wind velocity $\overline{V_w}$. This change in reference defines the major difference between turbulence relative to flight vehicles and turbulence in the field of wind engineering, and has important implications on how turbulence is measured and defined for moving aircraft.

2.3.1 Turbulence Intensity Relative to a Flying Vehicle

Turbulence intensity was previously defined as the ratio of the standard deviation to mean wind speed (Equation 2.4). In the case of a moving vehicle, where motion through the air is independent of wind speed, turbulence intensity relative to the vehicle becomes a function of its flight speed. By substituting the vehicle flight speed (V_f) for the mean wind speed, turbulence intensity becomes relative to the vehicle and is denoted by J_i (where i can be u, v or w for the longitudinal, lateral and vertical components respectively) as per Equation 2.11:

$$J_u = \frac{\sqrt{\overline{(u')^2}}}{V_f}, J_v = \frac{\sqrt{\overline{(v')^2}}}{V_f}, J_w = \frac{\sqrt{\overline{(w')^2}}}{V_f} \tag{2.11}$$

For a vehicle with a relatively high airspeed, the mean becomes large compared to the standard deviation (unchanged for a given terrain, elevation and atmospheric wind speed) and the perceived turbulence intensity, J_i, is low. At the other end of the flight spectrum, a vehicle that is hovering has a zero mean velocity relative to the airflow and correspondingly an infinite turbulence intensity. The relative turbulence intensity J_i is not completely independent of wind speed, as the standard deviation of wind speed in each orthogonal component at any given location are themselves dependant on wind speed, and additionally on elevation and terrain. As wind speed increases, so does the magnitude of the fluctuating components u', v' and w'. Therefore even at a constant flight speed, J_i will increase with increasing wind speed (Figure 2.6).

2.3.2 Effect of Turbulence on Fluctuating Flow Angles

As turbulent eddies move past the measurement point, the local value of α varies depending on the fluctuating value of u' and v'. In the case of a moving vehicle, the horizontal component is aligned with the flight direction, becoming a function of flight speed; however, the vertical component is unchanged. This results in a reduction in the instantaneous flow angle variations with increasing flight speed. An indication of the magnitude of the fluctuations in pitch angle is its standard deviation

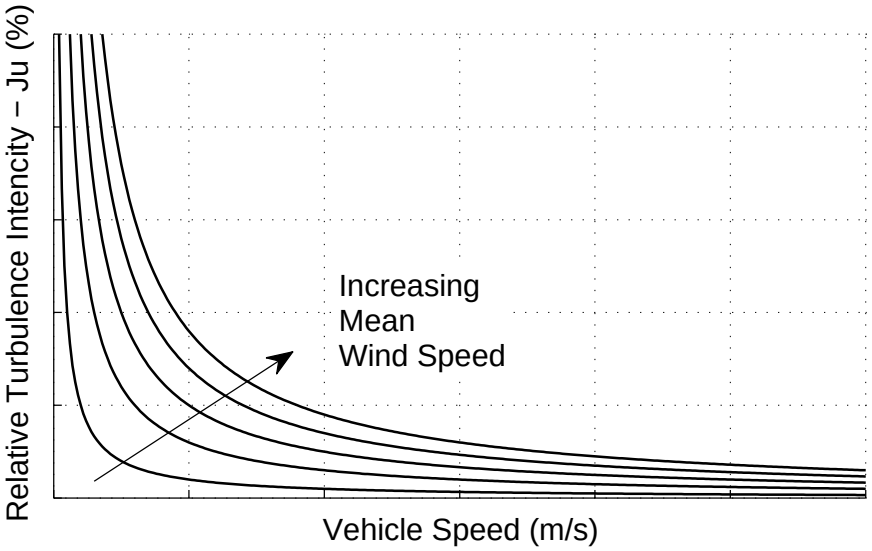

Figure 2.6: Relative turbulence intensity (J_u) as a function of flight speed and wind speed

(σ_α), illustrated in Figure 2.7 as a function of flight speed.

The response of a wing to turbulence is dependent on the influence the turbulence has on the lift distribution of the wing. Ignoring effects of local separations and instabilities (which exist at low Re), the lift distribution can be simply modelled as a series of span wise strips where the lift produced by each strip is a function of the local C_L. As a turbulent eddy passes the wing, α at each strip will be unique, pending the size and strength of the eddy. The difference in local incidence between two points as a function of distance ($\delta\alpha_x$) gives an indication of the difference in lift produced at each spanwise station, and hence the asymmetric loading that produces a response in roll. This is a highly simplified example used to conceptualise the mechanism at work; however, in even more complex flows where local separations may be present, this analysis is still valuable as the magnitude of separation bubbles is still a function of α.

The instantaneous local angle of incidence, or pitch angle (α) at the point of measurement is a vector sum of the instantaneous vertical velocity component (v') and the sum of the longitudinal component (u') and the vehicle flight speed (V_f) given by Equation 2.12.

$$\alpha' = tan^{-1}\left(\frac{v'}{V_f + u'}\right) \tag{2.12}$$

The magnitude of fluctuation in α is a function of flight speed as shown by Equation 2.12. The local fluctuation in pitch angle reduces with increased airspeed, resulting in lower magnitude disturbances. By contrast, the magnitude of pitch fluctuation as a function of environment (for example wind and

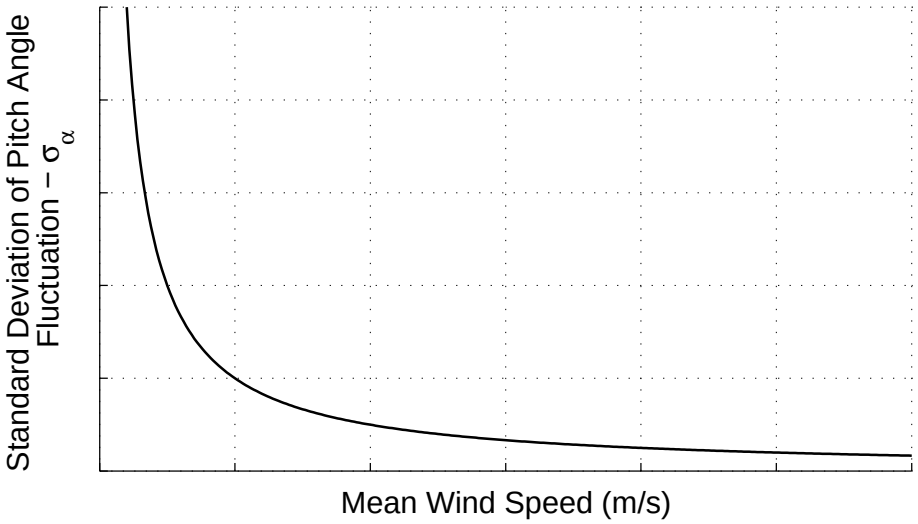

Figure 2.7: Pitch angle fluctuations as a function of mean wind speed

terrain) relative to the vehicle, but independent of flight speed, the term σ_α is produced by dividing by mean flight speed V_f.

$$\sigma_{\alpha_V} = \frac{\sigma_\alpha}{V_f} \tag{2.13}$$

2.3.3 Frequency as a Function of Flight Speed

The rate (frequency) that turbulent eddies move past the vehicle is a function of flight speed. When viewing a spectrum of measurements taken from the vehicle, it is desirable to non-dimensionalise the frequency by the flight speed to enable analysis of the frequency content of a signal under different flight conditions independent of velocity. Dividing the frequency by the flight speed, V_f, produces a reduced frequency term, k, also known as wave number, given by Equation 2.14:

$$k = \frac{f}{V_f} \tag{2.14}$$

2.4 Turbulence Modelling

The prediction and replication of turbulent flows is important for investigating the effects of turbulence on vehicles and structures, since closed-form analytical solutions with exact solutions are not possible. There are a number of methods available depending on the application and area of study, including computational and experimental techniques.

2.4.1 Analytical Methods of Analysis

The problem of turbulence modelling is generally not amenable to analytical solutions, thus statistical analysis and empirical formula are frequently used for the predictions of turbulence properties. Through the use of momentum transfer and energy equations, some general equations of motion can be derived; however, generally these result in more unknowns than there are equations giving rise to closure problems as explored by various authors (Nieuwstadt and van Dop 1981, Panofsky and Dutton 1976, Pope 2000). A number of general solutions are possible if various assumptions about the flow are made; however, these will not be explored here, since their use is restricted to simple flows, not representative of those in the ABL.

2.4.2 Computational Modelling

Computational analyses typically involve a discretisation method where a form of the Navier-Stokes equations are iteratively solved over a set of discreet points forming a grid or mesh have been attempted by numerous researchers. In the most general case the resolution of the flow field is limited by mesh size, which in turn is limited by the computational power available. It becomes clear that to resolve fine scales over a large area, either very powerful computers or long run times are necessary. Several generic type turbulence models, such as Large Eddy Simulation (LES) have been introduced to assist in overcoming this problem (Wilcox 1998); however, running simulations of flows with mesh sizes sufficiently fine to resolve all turbulent scales down to inertial sub scales (required for accurate energy dissipation) is challenging given the computational power available today at most institutions, although this may become feasible in the future.

For the research in this work, Computational Fluid Dynamics (CFD) methods – whilst promising for future work – were not considered presently sufficient nor reliable in the absence of experimental data for verification.

2.4.3 Experimental Replication

Given the impracticality and unavailability of sufficiently powerful computational resources and the inaccuracy of CFD solutions in large-scale free stream turbulent flow simulations. Studies involving

turbulent flows remain an area in aerodynamic research work requiring the use of experimental facilities. Typically, a large wind tunnel is set up to generate turbulence via a system of grids and screens to replicate the desired level of turbulence. Turbulence grids are a common method of turbulence generation, with different turbulence scales being generated by varying grid size and spacing. Generally for the flow to become uniform homogeneous turbulence behind a grid, a distance of some 10-15 times the grid spacing is required (Dryden and Hugh (1936), Walshe (1972), Stalp et al. (1999)), An illustration of grid generated turbulence is shown in Figure 2.8.

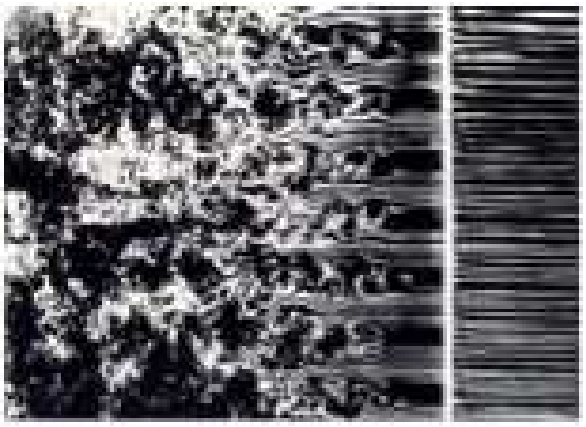

Figure 2.8: Grid turbulence (Pope 2000)

Chapter 3

Measurement of the Micro-scale Turbulence in the ABL

The work contained within this chapter was conducted as part of a team of which the author was a member, funded by the Airforce Office of Scientific Research (AFOSR) during 2005. The results of this study were published as a report (Milbank et al. 2005), available in the public domain. This chapter provides a summary of this work as it is the basis of the remaining work in this thesis and is referred to extensively.

As discussed in Chapter 1, there has been a great deal of work by wind engineers and meteorologists in measuring the turbulence present in the ABL for purposes such as estimating the wind loads on tall structures, understanding pollutant dispersion, the local environments around forest canopies and for many other purposes (Holmes 2001). Much of this research has focused on relatively large scales, hence the size of the instrumentation used has often exceeded the size of actual MAVs. A knowledge gap – identified in Chapter 1 – exists concerning turbulence at small scales and close lateral spacing. An understanding of the statical properties of atmospheric turbulence in the surface layer of the ABL at temporal and spatial resolutions relevant to small MAVs, birds and insects is highly desirable and concerns the initial component of the work presented in this chapter. Specific research goals include:

1. Quantifying the relationship between the standard deviation of relative incidence (pitch angle) between two points in space as a function of lateral separation (a measure of lateral coherence).
2. Determine whether the $-\frac{5}{3}$ slope of the power spectral density curve as proposed by Kolmogorov (1961) is valid higher frequencies (smaller scales) in the ABL surface layer than those measures in previous work by Panofsky and Press (1962), Flay (1978) and other authors.
3. Characterising turbulence levels and scales present in the roughness zone under different wind conditions and different upstream terrain roughness conditions (for example from "open farm-

land" to "city centres") at small scales. This is to focus on more complex terrain close to the surface which is representative of the environments in which MAVs are envisaged to operate.

Relevant data were acquired using a set of small robust pressure probes mounted above a car, a technique developed from earlier work by Watkins (1990) using hot-wire anemometers. This work was reviewed in Chapter 1.

3.1 Experimental Method for On-Road Measurements

A number of wind measurements were made in a variety of terrain and wind conditions using a set of four multi-hole dynamic pressure probes (Cobra probes) laterally separated by either 150 mm or 50 mm depending on configuration. Terrain was categorised by roughness and undulation (hilliness). Existing classification schemes (for example ISO, International Standards Organisation and others) were considered too broad for this work. A new classification matrix was used based on works by Davenport, which were reviewed by Wieringa (1992). The Beaufort wind scale was used to describe wind conditions. Details of the classification schemes are provided in Appendix A. A complete test matrix of "desirable" test conditions was constructed representing a variety of conditions relevant to MAV operations, and is provided in Appendix A.

3.1.1 On-Road Experimental Test Matrix

Unlike measurements in a controlled environment, outdoor testing relies heavily on prevailing weather conditions and available test environments. Accordingly, not every desired test condition was able to be investigated in a reasonable time frame. The final achieved test matrix is shown in Table 3.1.

Table 3.1: Test matrix for on-road measurements within the atmospheric boundary layer (see Appendix A for explanation of terrain classification)

	Wind Speed (Force)					
Terrain (Roughness-Undulation)	0	1	2	3	4	5
4-2	- -	- -	X	X	X	X
5-2	- -	- -	X	X	X	- -
6-2	- -	- -	X	X	X	- -
7-2	- -	- -	- -	X	- -	- -
8-2	- -	- -	- -	- -	- -	- -
4-3	- -	- -	- -	- -	- -	- -
5-3	- -	- -	- -	X	X	- -
6-3	- -	- -	- -	- -	X	- -
7-3	- -	- -	- -	- -	- -	- -
8-3	- -	- -	- -	- -	- -	- -

The desired range of wind speeds for these tests was based around a median global wind speed of approximately 3 m/s (Holmes 2001). On the vast majority of days (>95%), wind speed is less than 10 m/s and only exceeds this under extreme weather conditions. As MAV operation is additionally hampered by winds exceeding nominal flying speed, 10 m/s was considered a upper bound for testing. Based on the wind matrix in Appendix A the wind speed range of interest is between Force 0 and Force 5. Winds stronger than Force 5 are considered to be outside the likely operational capabilities of the aircraft and are therefore not of immediate interest. The majority of wind data acquired concerns wind speeds ranging from Force 2 to Force 4.

Terrain undulation and roughness selections (table A.2) were adapted according to local availability. It is operationally important to be able to operate MAVs in a variety of terrain categories from flat open country to built-up inner city landscapes, with the latter being the most desirable. The majority of measurements were made at locations on the edge of built up areas and in more open terrain characteristic of the rural countryside, forming a useful baseline with which to contrast results from more urban locations. The significant quantity of measurements under these conditions yielded a useful database concerning a large range of wind conditions for the same locations. Finally, additional measurements were made in built-up areas including suburban streets and inner city canyon type terrain. These tests were limited to times of minimum traffic to allow constant vehicle test speeds, as such, a comparatively reduced data set was acquired, resulting in the test matrix shown in Table 3.1.

3.1.2 Measurement Equipment and Data Acquisition

Data were acquired using a set of four multi-hole dynamic pressure measurement probes (Cobra probes) mounted on a mast above a moving vehicle (Figure 3.1). Details of the pressure probes are discussed in Chapter 4. The experimental configuration used for this work is a development of that used in prior work by Watkins (1990).

Mounting the instrumentation on a moving vehicle provides several distinct advantages over more traditional fixed location measurements commonly associated with meteorological measurements:

- The highly turbulent flows present in built up areas, particularly on days with light winds, have a mean pitch and yaw component that fluctuates though large angles (+/- 90°) due to large turbulent eddies passing the sensor inducing high transverse and vertical component velocities relative to the mean windspeed ($\overline{U}$). An extreme example is very low wind speeds where the instantaneous velocity approaching the sensor can swing though 360° as a large eddy passes by. The sensors used in this work have a zone of acceptance of +/-45° from the centreline, therefore some data points would fall outside this range causing null or false readings. By moving the sensor though the air with a mean velocity into the wind, a mean flow component in the U direction is superimposed, the angles of fluctuation are reduced and the likelihood of flows being within the probes' angular acceptance is increased.

- The Cobra probes are an analogue instrument where the pressure on each face is converted to a voltage, which is measured by an analogue-to-digital converter in an attached PC. The manufacturers data on the pressure sensors used within the probe body show that they are most accurate within the mid voltage range of the sensor (effectively for velocities exceeding 3 m/s). Mounting probes on a moving vehicle ensures that the sensor is always operated at a speed range commensurate with high device accuracy.

- By moving through the air at a reasonable speed, a large amount of data are obtained within a shortened time period. Assuming that Taylor's hypothesis (Stull 1988) of a "frozen" flow field holds true over short time scales, moving the probes is essentially the same as taking a long sample from a fixed position. For longer time samples (as per lower frequency analysis) this assumption may break down, though this phenomena is considered outside the current area of interest as large disturbances may be considered as quasi static in terms of their effect on the vehicle, see work by Bearman and Morel (1983). As the Cobra probe is capable of relatively high sample rates, samples can be taken at high driving speeds (more than 10 m/s). The vehicle velocity can then be removed later in post processing to restore the original time history.

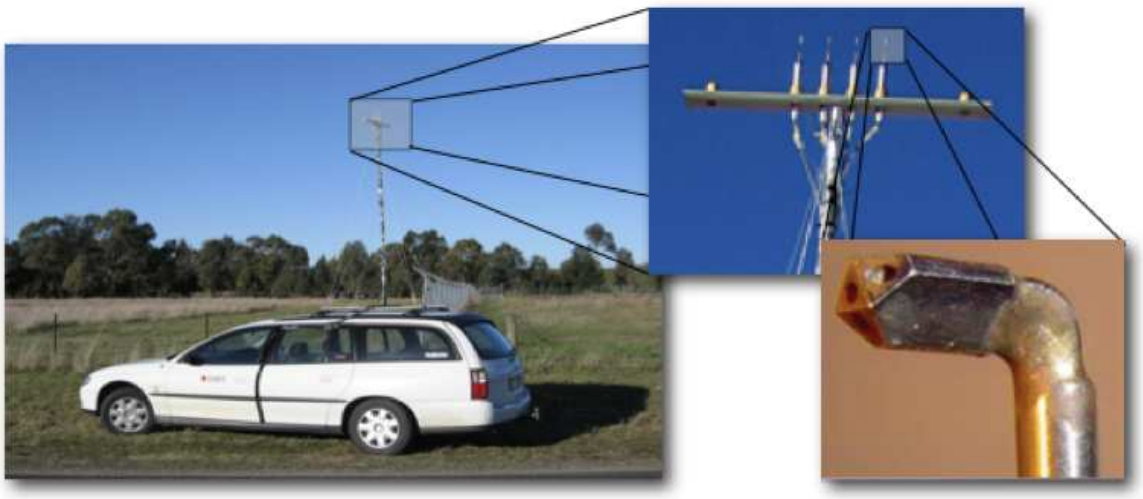

Figure 3.1: Bank of four Cobra probes mounted to a mast above the test car

Data were sampled from the four probes via a National Instruments DAQ card in a laptop PC. The acquisition software is proprietary to TFI and supplied with the instruments (further details anr discussed in Chapter 4). Each probe requires four analogue channels totalling 16 for 4 probes. Data were sampled at a rate of 1,024 Hz on each channel, with typical sample lengths varying from between 2-30 minutes depending on location and prevailing conditions, with longer samples preferable to capture lower frequency content.

Calibration of the experimental instrumentation was performed as follows:

- The Cobra probes are supplied in a pre-calibrated state by the manufacturer and require no in-situ calibration, although their calibration was validated periodically by the supplier both before and after tests. The instruments uses solid state temperature-compensated piezo-restistive pressure transducers which do not exhibit significant drift with ambient temperature changes and over moderate time scales. The manufacturer's data-sheet for the sensors shows very little drift with temperature over testing range (between 15-125° C)[1].
- Between sample sets the instruments are "zeroed" (voltage offsets in a zero wind state are removed from readings).
- The effect of vehicle proximity to the probe mounts was investigated by driving in calm wind conditions. Changes in the vertical velocity component were measured and found to be very low within the relevant speed range. Probe alignment was also measured and corrected during these tests.
- The level of vibration in the mast system was measured using a multi axis accelerometer mounted to the mast. Measurements initially revealed a high degree of vibration in the mast system. Extra stiffness members and stays were added, removing much of this vibration. The effect of the remaining vibration on probe output was investigated. Very little effect was found.

Once a suitably straight and level stretch of road was found with desired terrain and wind conditions, data sampling was commenced and the the car driven along the road at a predetermined speed. Tests were conducted in both cross-wind and head-wind conditions. Ambient conditions (wind speed, temperature and barometric pressure) were recorded for each test. Vehicle speed was measured using a GPS system.

3.1.3 Data Post-Processing

The post-processing procedure involved the following key stages:

- *Velocity corrections* – the velocity of the vehicle, being superimposed on data, is removed.
- *Angular corrections* – data were corrected for crosswind (mean yaw component) and probe offsets established during calibration runs.
- *Signal filtering and spectral analysis* – for spectral analysis, data were filtered to avoid aliasing and to remove any high frequency noise. Details of the spectral methods applied are presented in Appendix C.

[1] See Chapter 4 for further information.

3.2 Results from On-Road Measurements

Results presented include turbulence intensity levels and length scales, frequency spectra, and an analysis of fluctuating pitch angles at the measurement points as a mechanism for directly affecting the forces and moments experienced by a small aircraft wing. All results are presented either independent of velocity in the case of spectra (shown as reduced frequency) or, where this is not feasible, shown normalised to an ideal replicated flight speed of 10 m/s. These statistical descriptions of turbulent flow are common in wind engineering and are summarised in relevant ESDU datasheets (Anon 1976a).

3.2.1 Turbulence Intensities under Different Terrains and Wind Conditions

Turbulence intensity is defined and discussed in Chapter 2. It is for clarity that it is again noted here that there are two values of turbulence intensity used in this work, I_{xx} and J_{xx}. I_{xx} is the turbulence intensity as measured by a fixed point on the Earths Surface. J_{xx} is the turbulence intensity as experienced by a vehicle (such as a MAV) flying through the wind, which itself has a mean velocity with respect to the Earths surface.

The turbulence intensities for a selection of wind conditions in different environments are shown in Table 3.2, and confirm that as wind speed increases, turbulence intensity with respect to the vehicle (J_{xx}) increases: there is more turbulent energy in the airstream in the form of stronger eddies. As the roughness of the terrain upstream is increased there is also a increase in the magnitude of the turbulence. Results are shown for wind speeds up to Force 5 and terrain roughness ranging from open country to inner city.

Table 3.2: Measured turbulence intensities with respect to the vehicle (J_{xx} %) under a range of terrain fetch and wind conditions. (Appendix A for terrain and wind classification)

		Wind Speed (m/s)				
Location	Terrain level	Force 1	Force 2	Force 3	Force 4	Force 5
Open airfield, smooth runway	3-2	2.4	- -	- -	- -	- -
Country, scattered trees / buildings	4-2	- -	7.1	9.3	17.2	- -
Inner city - very built up	7-2	- -	14.2	17.3	20.1	- -

3.2.2 Auto-Correlation and Length Scales

Length scales are a measure of the characteristic length, or size of the"dominant" largest eddy size present in turbulent flow, and may be calculated in a number of ways, as discussed in Chapter 2. In this work, length scales are calculated using the auto-correlation method where the turbulent field is considered frozen and the signal is compared to itself to determine the largest eddy size passing the

sensor. Table 3.3 shows the length scales calculated using this method for different terrain fetch and wind conditions. The results in Table 3.3 show little variation in length scale with wind strength, and only a small variation with change in terrain type.

Table 3.3: Integral length scales calculated using auto-correlation for a range of terrain fetch and wind conditions

		Wind Speed (m/s)				
Location	Terrain level	Force 1	Force 2	Force 3	Force 4	Force 5
Open airfield, smooth runway	3-2	22.4	- -	- -	- -	- -
Country, scattered trees / buildings	4-2	- -	17.1	18.3	21.2	- -
Inner city - very built up	7-2	- -	21.8	19.2	20.3	- -

3.2.3 Spectral Analysis

Whilst turbulence intensity and length scales provide useful information on the relative magnitude of the turbulence fluctuations at the point of measurement, they do not describe how the energy is distributed in the frequency domain (for example the energy associated with different eddy sizes). This information is presented as Power Spectral Densities (PSDs) presented on a logarithmic scale against a reduced frequency (or wave number $k = \frac{f}{V}$), allowing data to be plotted independently of velocity of the mean flow velocity. This concept is illustrated in Figure 3.2 where the data collected from one location at different mean wind speeds are plotted. One can assume from the data presented in Figure 3.2 that the -$\frac{5}{3}$ slope continues on the low frequency end if the sample size were long enough. In Figure 3.2 the data are reduced onto a single line, indicating that the changing in mean wind speed does not have a significant effect on the energy distribution with reduced frequency. Its worth noting that the early cut off on the high frequency end of the spectrum in Figure 3.2 is due to the shorter sample sizes that were available with these tests, due in part to the environment and vehicle speed necessary to gather good data. Analysis of lower frequencies requires longer data samples.

Figure 3.3 presents the PSD for three different locations with increasing terrain roughness at similar mean wind speeds, and shows that with increasing terrain roughness there is a increase in the energy levels present in the flow; however, the $-\frac{5}{3}$ slope discussed in Chapter 1 is maintained.

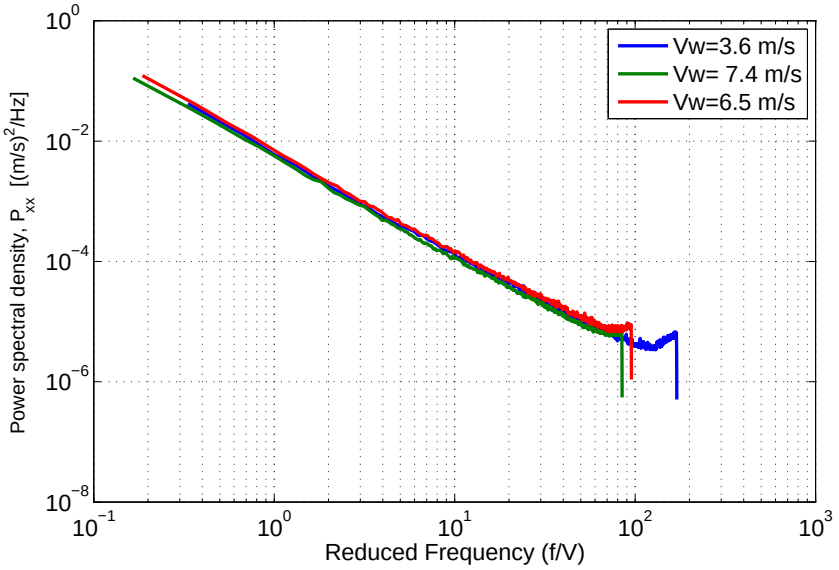

Figure 3.2: PSD showing the effect of increasing wind speed in the same location

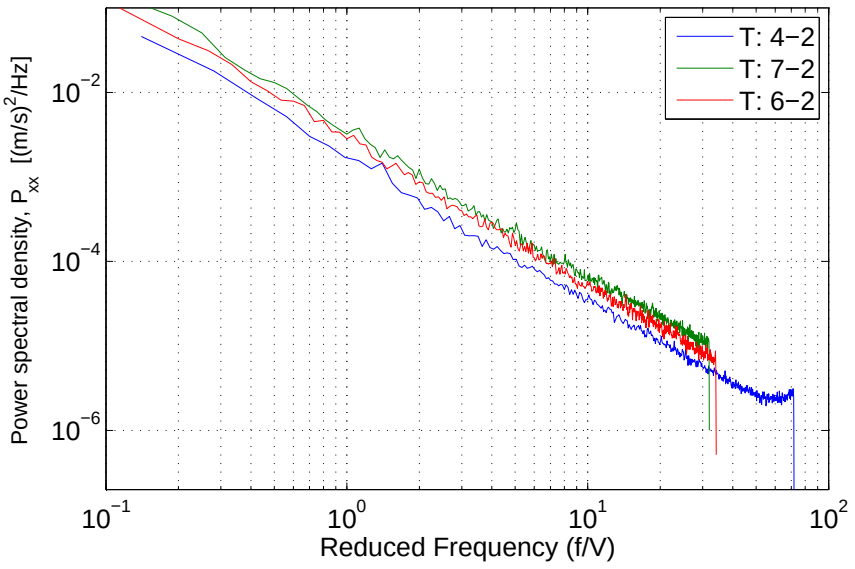

Figure 3.3: PSD showing the effect of fetch roughness

3.2.4 Spatial Analysis Using Multipoint Data

As measurements were made using a bank of four probes, the variation between laterally separated points in space as well as in time can be investigated. One unique quality of these tests was the relatively small separation of the measurement points, allowing investigation of the flow behaviour across the typical wingspan of a MAV, rather than the many meters normally associated with atmospheric data. This provides useful information for considering the influence of spanwise variation in flow velocity and incidence over time as a dynamic input.

3.2.4.1 Pitch Angle Variation with Lateral Separation

Variations in local incidence along the span of a wing as an eddy passes the aircraft induces changes in local lift coefficient and therefore affects the spanwise lift distribution in a time-dependent manner. The variation in lift distribution generates a unbalanced force distribution across the wing and generates a roll input into the aircraft. The response of the aircraft to this input is dependant on the frequency and magnitude of the disturbance and the dynamic characteristics and relative size of the aircraft.

The variation in pitch angle over time (in this case 1 second) is shown in Figure 3.4. A significant high frequency pitch fluctuation is observed, with some larger disturbances superimposed on the signal. Plotting the pitch angle at each location on the one axis shows variation between each laterally spaced point (Figure 3.5). Plotting the the pitch angle at each point as a surface across the span of the MAV and over time, shown in Figure 3.6, illustrates how the local pitch angle at each point in the wing can show significant variation and is a function of the size of eddies passing the wing and the lateral separation of the measurement points. For a particular eddy size - as the lateral separation increases - it is hypothesised that the difference between successive probe the pitch angles also increases. The magnitude of instantaneous variations in the flow environment can thus be examined by plotting the standard deviation of the variation between points (Figure 3.7).

Figure 3.7 shows that the relationship between lateral separation and standard deviation of pitch variation to be approximately logarithmic, with the rate of convergence likely being a function of the mean eddy size, or turbulent length scale of the flow. Further work is required to establish this relationship, and is the subject of several ongoing studies at RMIT University(for example Watkins et al. (2010b).

In addition, the term pitch angle is a function of flight speed; as airspeed increases, the vector sum reduces since the vertical component of velocity remains the same. Therefore vehicles flying faster through the air experience smaller disturbances. The frequency of the fluctuation of pitch angle is expressed as a PSD from one Cobra probe (Figure 3.8). It is shown that for different terrain conditions the slope (energy cascade) remains constant; however, the overall magnitude, or energy content, is higher for rougher terrains. This is expected owing to higher turbulence levels.

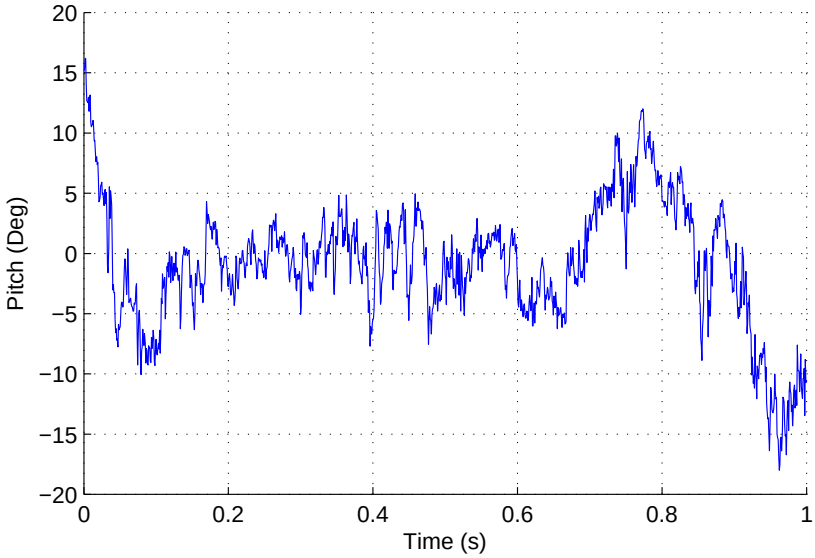

Figure 3.4: Time history showing the fluctuating pitch angle at a single point in space, measured at a flight speed of 10 m/s in built up city terrain

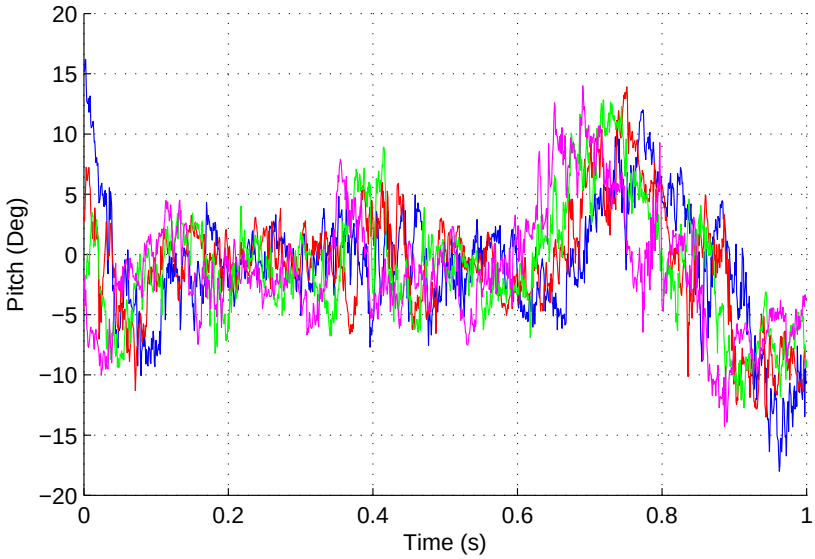

Figure 3.5: Time history showing the fluctuating pitch angle at four points in space (each of the four measurement probes), measured at a flight speed of 10 m/s in built up city terrain

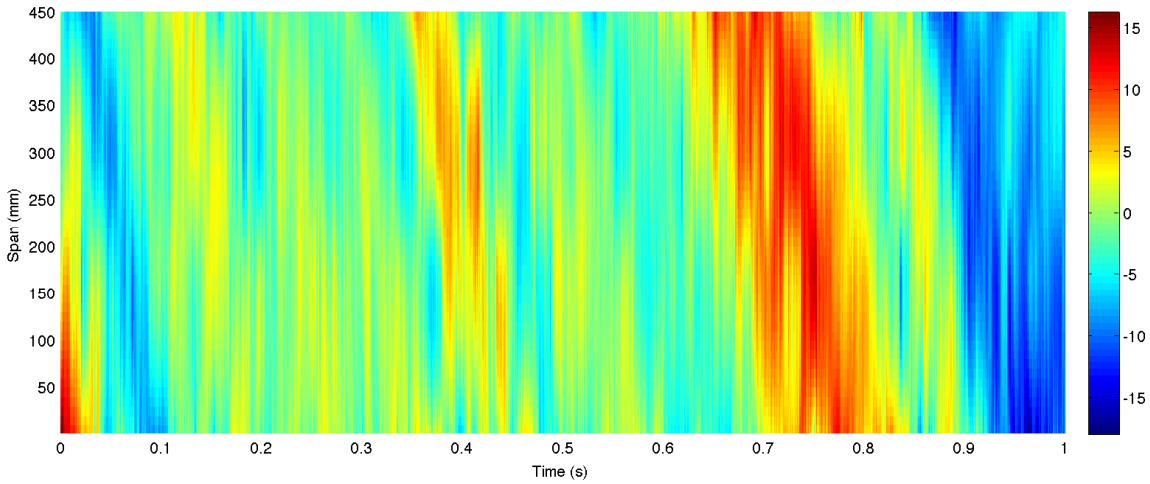

Figure 3.6: Pitch angle of each point in space shown as a surface illustrating the instantaneous pitch angle variation across the span of a small aircraft over time

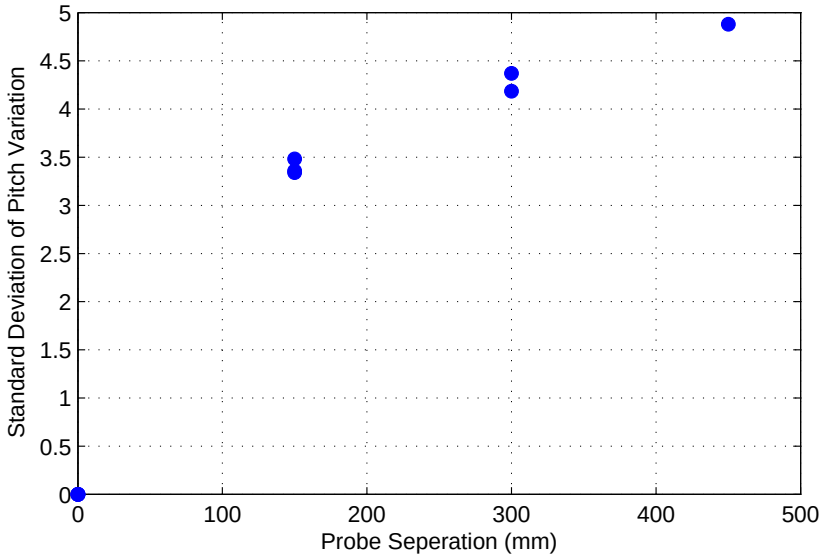

Figure 3.7: Standard deviation of the difference in the local pitch angle between two points in space as a function of lateral separation

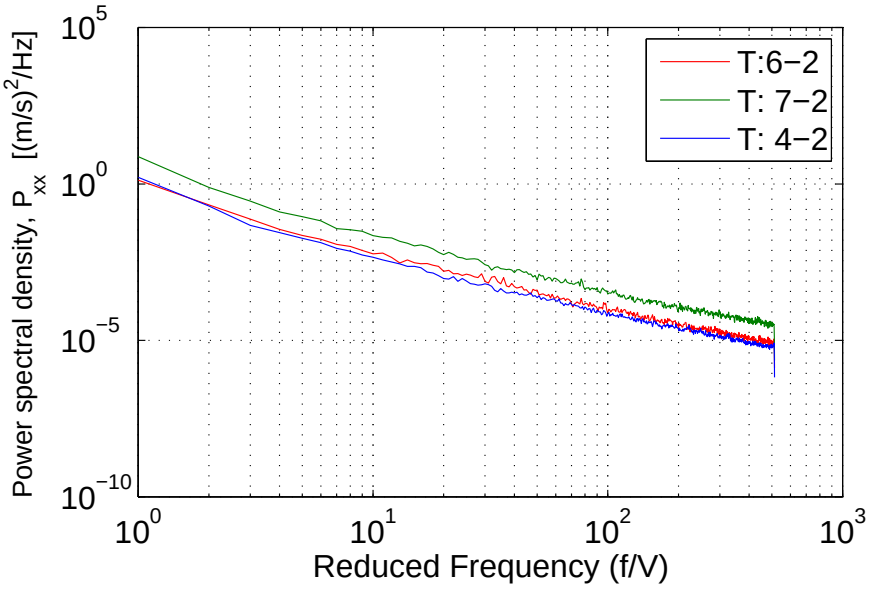

Figure 3.8: Frequency spectra of fluctuating pitch angle with varying terrain roughness

3.3 Conclusions

This work provided useful insight into the properties of turbulent flows close to the ground, and the relationship between wind speed, upstream terrain roughness and the turbulence levels experienced by a flying vehicle moving thorough it; however, it is not a exhaustive study as only a small subset of conditions are investigated, which do not include measurements in the local wakes of large objects such as tall buildings. Specific conclusions can be summarised as follows:

1. At small scales, as for the larger ones measured by Flay (1978) et al, the $-\frac{5}{3}$ slope predicted by Kolmogorov (1961) holds true even close to the ground in the influence of the roughness zone.
2. Mean wind speed has no measurable effect on the magnitude or slope of the PSD when plotted as a function of reduced frequency. Terrain has negligible effect on the slope, but affects intensity levels.
3. The variation in pitch angle increases with lateral separation and is a function of terrain roughness and air speed. The effect of increased flight speed is to reduce the apparent variation in pitch angle since the mean horizontal component is increased whilst the magnitude of the vertical component remains unchanged. Conversely, the effect of increasing wind speed is to increase the pitch angle fluctuation since the mean horizontal component is now fixed, and the vertical component is now increased.
4. The turbulent length scale varies with terrain roughness; however, it remains constant for a particular terrain environment in different wind speeds.

The useful outcomes from this work provide a basis for more accurate simulation of small scale turbulent environments using either numerical computations (in terms of statistically generated control response models) and physical replication in a wind tunnel using a system of grids (to generate turbulence) within the test section. The latter method was employed extensively in subsequent sections of this work.

Chapter 4

Experimental Methods and Instrumentation

In this chapter the equipment, instrumentation and techniques used throughout the experimental investigation are presented. Detailed results and testing procedures follow in later chapters.

4.1 RMIT Industrial Wind Tunnel

Wind tunnel tests were performed to investigate the influence of atmospheric turbulence levels on MAV wings. Turbulence intensity levels that were statistically similar to those measured in Chapter 3 were replicated in the RMIT Industrial Wind Tunnel (IWT) using a system of grids located upstream of the test section. A range of turbulence levels were produced and investigated. Several full-size aerodynamic models of a simplified finite MAV wing of 300 mm span were tested under different turbulence conditions. Measurements of the mean and time-varying surface pressures were made. Flow visualisation was used to investigate the presence and location of flow separation, reattachments zones and to determine the effect of the free wing tip on the flow, particularly near the location of the pressure taps.

4.1.1 Wind Tunnel Configuration

The IWT is a closed-return wind tunnel with a closed 2 m by 3 m square test section of 9 m length with a 2:1 contraction upstream (plan view in Figure 4.1). The maximum empty tunnel speed is approximately 40 m/s (though this is reduced with models and turbulence generating grids in place). Flow quality is good for a facility of this type, the primary purpose of which is to conduct research

on large-scale automotive forms, industrial aerodynamics and aero-acoustics. The empty tunnel has a free-stream turbulence intensity of approximately 1.5% at a flow speed of 20 m/s as measured by Vino (2005). Whilst this is not as smooth as some dedicated aerospace facilities, it should be noted that this work focused on aerodynamic behaviour in turbulent flows. Moreover, the generation of suitably large turbulence scales matching those found outdoors requires a large test section which is not generally available in smooth flow aerospace tunnels. The IWT is used for aero-acoustic testing, and is fitted with acoustically treated turning vanes to reduce mechanical and wind noise. Electrical shielding produces a relatively low electrical noise environment. Further details of the IWT, including flow quality and noise information is provided in Appendix B.

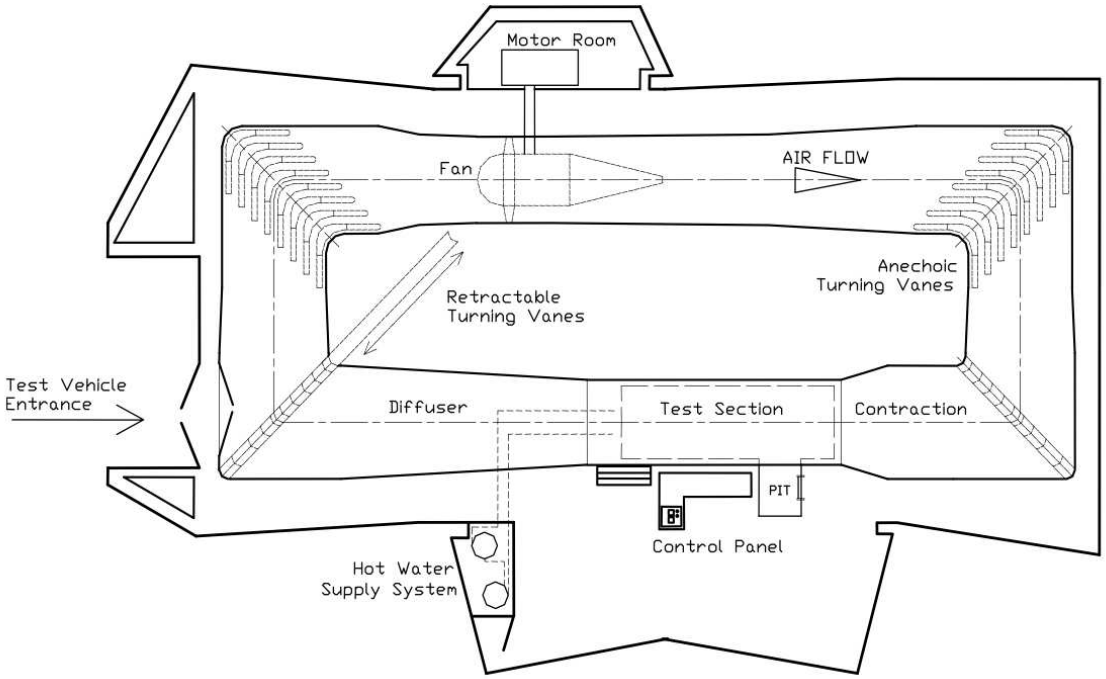

Figure 4.1: Schematic of RMIT Industrial Wind Tunnel (IWT) (Milbank 2005)

4.1.2 Turbulence Generation

Turbulence was generated in the IWT by placing large element grids upstream of the test section. Whilst it was realised that an almost infinitely large range of turbulence intensities can be experienced by an MAV flying at various speeds though various atmospheric winds and terrains, only a limited number of turbulence intensities were replicated in the wind tunnel. In addition, the scale of the grids and test section size dictates the largest integral length scale that can be replicated in the IWT, whereas in the outdoor environment the length scales can stretch to many tens of meters. This aspect of turbulence replication and sensitivity to turbulence length scale is part of ongoing work (Watkins et al. 2010a). However, for this work it was decided to generate length scales as large as practical and

a range of turbulence intensities that encompass some of relative turbulence intensities experienced by a MAV, as measured in Chapter 3. Initial experiments show that very high turbulence intensities (>40 %) could be generated in close proximity to the grid; however, in such a flow there is a very large variation in time-averaged velocity. It was decided to generate time-averaged velocity profiles across the test area of interest that were nominally flat, otherwise any effects would be from a combination of distorted velocity profiles and turbulence.

Various levels of turbulence were achieved by varying grid position both downstream and upstream of the tunnel contraction. The turbulence levels generated in the wind tunnel (measured at the model location) are summarised in Table 4.1 and further details are provided in Appendix B. Turbulence measurements were made using the same configuration of multi-hole pressure probes used in the outdoor tests, described in Chapter 3.

Table 4.1: IWT grid placement and generated turbulence levels

Condition	I_u (%)	I_v (%)	I_w(%)	L_u (m)	L_v (m)	L_w (m)
Empty Tunnel	1.5	1.5	1.2	0.8	0.4	0.2
Grid A (Test Section Grid)	7.0	6.0	7.5	0.25	0.15	0.1
Grid B (Contraction Grid)	13.5	10.0	6.0	0.8	0.4	0.4

Turbulence intensity levels shown in Table 4.1 match well with outdoor measurements presented in Chapter 3. Measured length scales in the tunnel are less than outdoors, indicating that the dominant eddy size (size of the largest eddy present in the flow) in the tunnel are less than that measured outdoors. This is largely due to the turbulence generation where the largest eddy size in the flow is a function of grid element size (Chapter 2). To generate turbulence scales comparable with outdoor measurements very large grids and hence tunnel test sections would be required. Such experiments were performed in a 9 m x 7 m x 50 m tunnel by the author and Milbank as part of this work (Milbank et al. 2005). However, even in this very large wind tunnel the largest scales can not be reproduced entirely due to the physical constraints of the test section. Despite this, the reproduction of the flow field is considered good as the energy content of the smaller turbulence scales match well with those measured outdoors and the spectral roll-off follows the $-\frac{5}{3}$ energy cascade theorised by Kolmogorov (Panofsky and Dutton 1976) and summarised in Chapter 2.

4.1.3 Model Location and Use of a Ground Plane

The model must be mounted sufficiently downstream of the grids such that the turbulence generated is well mixed and statistically consistent across a test plane (defined here as homogeneous). As discussed in Chapter 2, for grid-generated turbulence to become uniform, the grid must be placed at least $10 - 15d$ (where d is the effective grid element spacing) upstream. As the largest element grids used had spacing $d = 0.4$ m, the test article was located at least 5 m downstream of the grid to ensure a reasonably well mixed flow field.

A disadvantage of mounting the model so far downstream is that the boundary layer on the floor (and walls and roof) of the tunnel is relatively thick. Work by Vino (2005) suggests the floor boundary layer to be approximately $\delta^* = 50$ mm thick at this location in the tunnel. Should the model be mounted directly to the tunnel floor, interactions of the tunnel boundary layer would have significant influence on the flow field around the model. To minimise such interaction, a raised ground plane spanning the test section was installed 0.5 m above the tunnel floor and 6 m downstream of the tunnel contraction and turbulence grids, enabling the model to be mounted in the free-stream tunnel flow with minimum interaction with a floor boundary layer (though there remained a relatively thin boundary layer on the ground plane). The ground plane installed in the IWT with a model in place is shown in Figure 4.2.

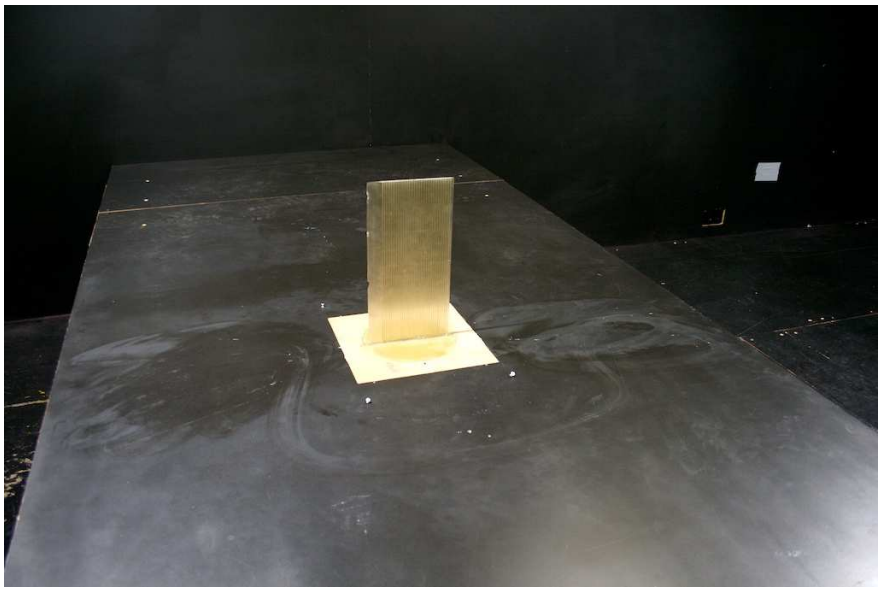

Figure 4.2: Pressure-tapped model mounted on the ground plane in the IWT test section

Velocity and turbulence profiles were measured at the model location on the ground plane using a Cobra probe mounted on an automatic traverse, with measurements taken from the ground plane to a height of 300 mm. Velocity and turbulence intensity profiles are shown in Figures 4.3 and 4.4 respectively, and confirm a close to uniform distribution along the model in the span-wise (vertical) direction, with a minimal boundary layer on the ground plane. The sample length was 30 seconds; the results presented are averaged.

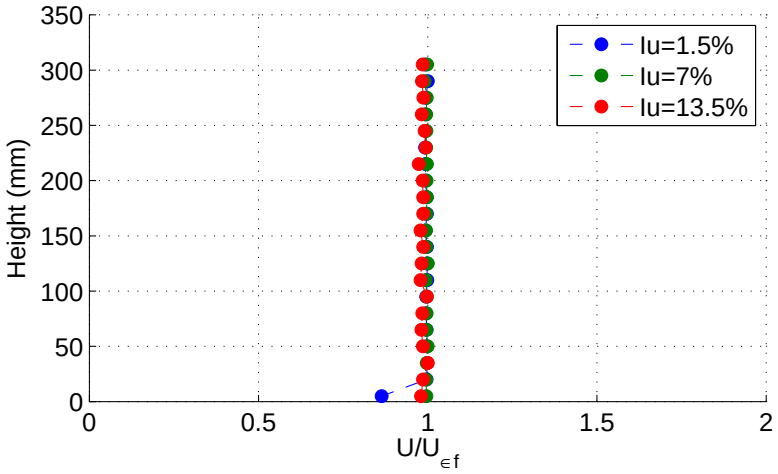

Figure 4.3: Vertical velocity profile ($\overline{U}$) measured above the ground plane at the model location using a Cobra probe from 2 mm above the ground plane to a height of 300 mm for all three turbulence levels

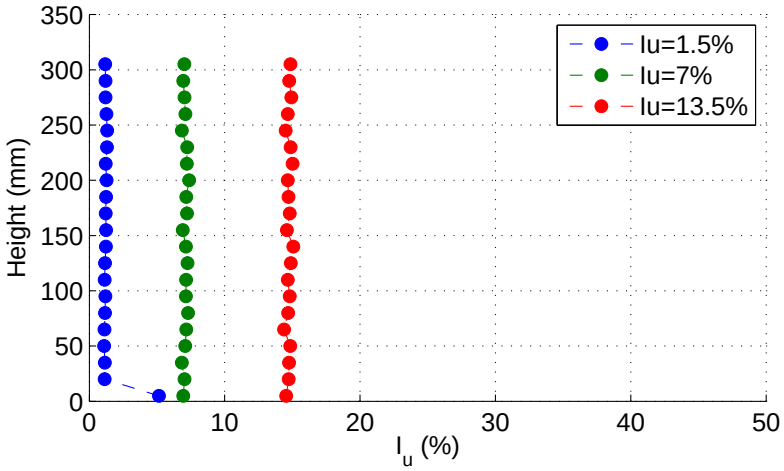

Figure 4.4: Vertical profile of turbulence intensity (I_x) measured above the ground plane at the model location using a Cobra probe from 2 mm above the ground plane to a height of 300 mm for all three turbulence levels

4.1.4 Wind Tunnel Calibration

Wind tunnel velocity was determined by measuring the dynamic pressure using a wall-mounted pitot-static tube connected to a Baratron pressure transducer. Calibration of the Baratron transducer was checked against an inclined manometer tube, which showed negligible difference in calibration compared to that supplied by the manufacturer. Static pressure was measured via the same pitot-static tube. The dynamic and static measurements at this location were calibrated against measurements made via a second pitot-static tube at the model location during a test run (without the model present), showing a difference between model location and the reference pressure location. These measurements were repeated with the turbulence grids present, and the differences taken into account when setting tunnel speed. Detailed information on wind tunnel calibration is provided in Appendix B.

To ensure well mixed turbulence, measurements were taken at a number of locations downstream of the grid using the same configuration of Cobra Probes used in outdoor measurements described in Chapter 3. Turbulence intensity was found to be stable 6 m downstream of the grids, confirming suitability of model placement in this configuration (Grusovin 2007).

4.2 Wind Tunnel Models

A generic flat plate type airfoil was selected for this work based on the work of Pelletier and Mueller (2000). While this geometry provides less than ideal performance in a real aircraft application (since a cambered wing is desirable to optimise lift/drag performance), an extensive body of knowledge exists on its behaviour concerning both low Re performance and boundary layer behaviour (a summary of which was presented in Chapter 1) in relatively smooth flow. Pelletier and Mueller used a flat 0% camber based geometry with a semi-elliptical leading edge and a tapered trailing edge (shown in Figure 4.5) with a chord of 150 mm and a thickness of 2.5%. To enable the verification of this work against those obtained by Pelletier and Mueller, the same geometry and scale of airfoil was used, with results obtained at similar Re. The use of a flat plate with a semi-elipitical leading edge produced well formed separation bubbles which separate downstream of the leading edge.

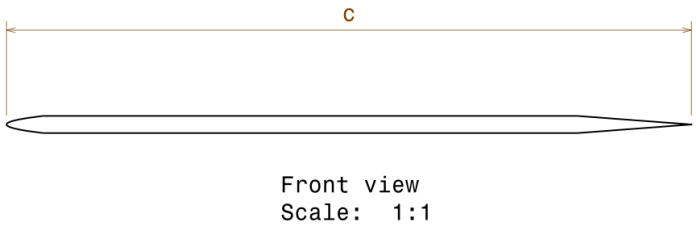

Figure 4.5: Wind tunnel model cross-section showing semi-elipitical leading edge and tapered trailing edge

4.2.1 On the Use of Finite Span as Opposed to "Infinite" Span Wings

Much of the work on low *Re* airfoil performance, including the work by Pelletier and Mueller (2000), makes use of "infinite span" or 2D wings. These models are mounted such that the model spans the tunnel test section, thereby avoiding the effects associated with the pressure discontinuity at a free wing tip. The pressure discontinuity at the tip of a wing at an incidence to the flow causes a tip vortex to form when the flow "escapes" from the higher pressure surface to the low pressure (suction) surface around the wing tip. As a result, the span-wise pressure distribution is non-uniform, causing the flow to move from the higher pressure at the root on the pressure surface towards the wing tip, and on the suction side from the tip towards the lower pressure at the root, resulting in streamlines that do not follow the geometric wing chord and causing finite wings to be referred to as "three-dimensional". Having a model that spans the tunnel test section means there is no free tip and no path for the flow to travel from the pressure surface to the suction surface. The subsequent uniform span wise pressure distribution results in no span wise flow component, and the flow over the wing is assumed to approximate a two-dimensional (2D) section (Houghton and Carpenter 1993).

As previously mentioned, to effectively generate large turbulent length scales in the wind tunnel, a relatively large test section is required to both accommodate the large grids, and the resulting large eddy sizes without interference from the tunnel walls. A model that spans the tunnel may be ideal from an aerodynamic perspective; however, in a 3 m x 2 m test section it would be difficult to fabricate a model of the desired chord and thickness while having sufficient stiffness to avoid model deformation and aeroelastic excitation. This is complicated further when dynamic pressure measurements are to be made, where to achieve favourable tubing system response characteristics, shorter length sections are required. Since there is insufficient internal volume within the wing to house pressure transducers, the length of tubing required in a full-span wing would not allow sufficient frequency response. A full span model could be fabricated and installed in a tunnel with a smaller test section; however, a smaller test section and model would not permit the generation of relatively large scale turbulence.

Despite the disadvantages of a finite span wing with a free tip, the requirement to measure dynamic pressures on a small wing in a large wind tunnel essentially dictate a short span finite wing configuration. The effect of span wise flow and a strong tip vortex are reduced by increasing the aspect ratio of the wing (or maintaining a chord of 150 mm, by increasing span). Hence the span of the model will be a compromise between the length of pressure tubing and the response of the pressure measurement system (a shorter wing has increased frequency response of the tubing system) and the influence of the tip vortex and spanwise flow on the boundary layer and wing performance. Keeping within the constrains of the definition of a MAV in Chapter 1 and using a similar size geometry to Pelletier and Mueller, a wingspan of 300 mm was chosen for the final geometry, which provided an AR of 2:1, and a effective AR of 4:1 when the refection by the ground plane is considered. This provided favourable frequency response with reasonable stiffness and a relatively large AR. It should be noted that real aircraft that fly outdoors have finite wings, therefore it is reasonable to study finite wings in the presence of turbulence in the wind tunnel with a view to understanding the flow patterns on a real aircraft of similar size.

4.2.2 Pressure Tapped Finite Flat Plate Model

Adding pressure taps to a thin (3 mm) flat plate wing at reasonable cost presented a significant manufacturing challenge. A solution was realised using *sterolithography*, a rapid prototyping process where a model is "printed" in successive layers from a CAD model. This enabled tubing channels to be constructed inside the wing. The models (shown in Figure 4.6) were constructed with 40 integral pressure taps, 20 on each surface. The channels were sealed at one end and connected at the other end pressure transducers with silicon tubing. The actual pressure taps were exposed on the mid span of the wing, 150 mm from the end. This was the only spanwise location investigated in this work, though the same process can produce models with pressure taps in any location. The tolerance of the finished assembly was $< \pm 0.1$ mm. Exterior surfaces required light sanding prior to testing to obtain a smooth surface finish. Surface roughness was estimated to be low, in the order of a moulded composite part after being polished.

Figure 4.6: Pressure-tapped wing manufactured with integral pressure taps using sterolithography. Tubing at one end connects pressure taps to the pressure transducers (Note: TE damage occurred occured after testing)

4.2.3 Flow Visualisation Finite Wing Model

Models for use with the flow visualisation were constructed from a carbon fibre foam sandwich allowing a thin yet stiff wing. The construction method used for the pressure tapped models was not considered suitable as the surface finish was not compatible with the solvents used in oil flow surface visualisation. Exterior surfaces were finished with a non-reflecting paint for photographic work with the surface oil visualisation. These wings were built to the same dimensions as the pressure tapped models, with a comparable surface roughness.

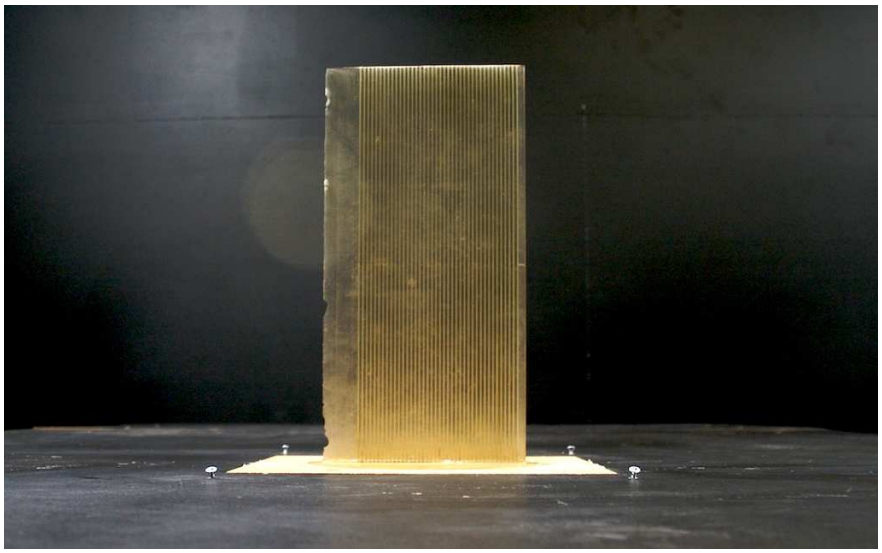

Figure 4.7: Pressure-tapped wing mounted to reflection plane

Figure 4.8: Carbon fibre wing model used for flow visualisation work

4.3 Pressure Measurement System

This work makes use of a digital pressure measurement system to measure pressures on the surface of the wing. Pressure taps were connected to an acquisition module containing discrete pressure transducers using a system of flexible silicon tubing. The direct measurement of fluctuating pressures by the transducers can be distorted by the dynamic response characteristic of the tubing system. For small frequency ranges about the mean signal, amplitude response may be be optimised by using tubing of minimal length and large internal diameter; however, both parameters are in this case constrained by model geometry. A second method is to introduce a restrictor into the system which effectively increases the damping, thereby reducing the frequency magnitude response of the system and maintaining the magnitude of the amplitude distortion within a few percent for a narrow frequency range beyond the mean (Irwin et al. 1979). However, with this approach phase distortion is not corrected.

A third method involves application of an either experimentally acquired or theorised transfer function, which is applied to discretized "blocks" of data as a correction in the frequency domain (Irwin et al. 1979). This method virtually eliminates distortion of both amplitude and phase from the tubing system, and consequentially was selected for this work.

4.3.1 Correcting for Tubing Distortion

The method proposed by Irwin et al. (1979) for predicting the response of a simple tubing system is known as the Inverse Transfer Method (ITM), and is implemented by letting the fluctuating pressure at the pressure tap (installed at the model surface) be represented by $P_0(t)$ (Equation 4.1) and the fluctuating pressure at the transducer be $P_1(t)$ (Equation 4.2). In this notation A_n and B_n are complex Fourier coefficients.

$$P_0(t) = \sum_{n=-\infty}^{\infty} A_n e^{i\omega t} \tag{4.1}$$

$$P_1(t) = \sum_{n=-\infty}^{\infty} B_n e^{i\omega t} \tag{4.2}$$

If the transfer function defining the characteristics of the system is given by T_n, then it follows that:

$$B_n = T_n A_n \tag{4.3}$$

Once the system transfer function, T_n, and the Fourier transform of the signal measured at the

pressure transducer, B_n, are known, the Fourier transform of the signal at the surface A_n can be determined from:

$$A_n = \frac{B_n}{T_n} \tag{4.4}$$

The signal at the surface, P_0, can then be found by taking the inverse Fourier transform of A_n. This can be achieved easily using modern computers and Fast Fourier Transform (FFT) techniques, the implementation of which are presented in further detail in Appendix C.

4.3.2 Analytically Obtaining the Tubing Transfer Function

A method for analytically determining the transfer function of a series of N connected tubes and volumes was proposed by Bergh and Tijdeman (1965). This method derives a system of equations based on a simplified combination of the Navier-Stokes equation, the energy equation and the continuity equation that relate the transfer function of each segment in the system to the pressure ratio between them. The overall transfer function is calculated recursively across the entire system by solving the resulting system of differential equations, while assuming that:

- The overall magnitude of the pressure disturbances are small
- The diameter of the tube is smaller than its length ($d < L$)
- The flow is laminar throughout the system
- The fluid obeys the laws governing ideal gasses.

4.3.3 The Dynamic Pressure Measurement System by TFI

The *Dynamic Pressure Measurement System* (DPMS) supplied by Turbulent Flow Instrumentation (TFI) was used throughout this work. The DPMS consists of a number of modules (Figure 4.9), each of which contains 15 pressure transducers connected directly to pressure tubing on the wing. This system can accurately measure mean and transient pressures without mechanical switching; practically limiting sampling rates to the frequency response of the tubing systems employed. Four modules were used and connected to a multiplexer. This was connected to a National Instruments (NI) 6034E analogue-to-digital card, featuring a single analogue-to-digital converter and an on-board multiplexer.

The acquisition software package "Device Control", supplied by TFI, performs two tasks: it sets the sampling properties and records the data as a time series, saving it to disk in a proprietary format,

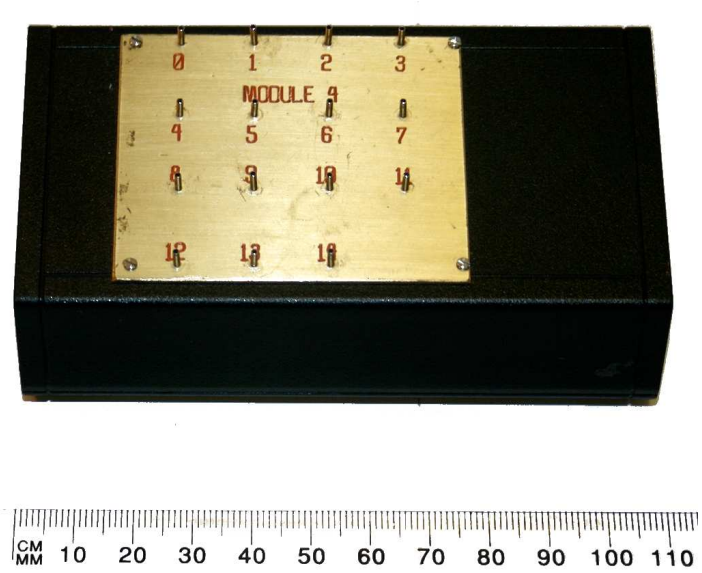

Figure 4.9: TFI Dynamic Pressure Measurement System (DPMS) module (1 of 4 used)

and then calculates the tubing transfer function using the Bergh and Tijdeman method described above, applying it to data as they are sampled (a near-real-time visualisation capability is provided).

The exact methods employed by Device Control to perform this "on-the fly" correction is proprietary and not specified by the manufacturer; however, it is known to follow the following general procedure:

- The data are acquired in blocks, the size of which are specified by the user
- Each block is converted into the frequency domain via FFT and corrected by the tubing transfer function
- The resulting frequency data is transferred back to the time domain via an inverse transform, and recorded to disk.

As this process affects the final time series obtained, and is dependant on the software configuration, the following considerations were made when configuring the system:

- The highest frequency that can be measured by the system is a function of the sampling rate and tubing response
- The sampling rate selected should in practice be at least twice as high as the highest frequency in the signal (Nyquist frequency to avoid aliasing)

- The lowest frequency component that can be discretised is a function of sampling rate and block size (the former divided by the latter). It is therefore favourable to use large block sizes, though this is limited in practice by computational resources as the acquisition system performs calculations "on the fly" as data are sampled.

For the experimental pressure measurement work, the following sampling parameters were used:

- *Sample Rate*: 3,000 Hz (per channel) - this was shown to be high enough to capture all the signal information arising from pressure fluctuations and line noise in the system, both of which occurred < 1400 Hz
- *Block Size*: 131,072 elements - this covers approximately 45 seconds per block, allowing measurement of signal transience of frequencies down to 0.1 Hz
- *Sample Length*: 10 minutes (approximately) - allowing a sufficient number of realisations (blocks) to produce a smooth spectra of sufficiently small sample variance in post processing
- *Mean Tubing Internal Diameter*: 1 mm ($\pm$0.1 mm tolerance)
- *Mean Tubing Length*: 300 mm.

The Bode plot for the tubing system (presented in Figure 4.10) illustrates the distortion of phase and magnitude for the installed tubing system. For frequencies below 100 Hz (approximately the highest frequency of interest) amplitude distortion effects are small ($> 2\%$). Variances in tubing system diameter contributed an additional 2% amplitude error.

Whilst the above theoretical analysis provides a good indication of the expected distortion as a result of the tubing system, the theory applies only to simple tubing systems. The tubing system used in this work is more complex, including branched tubes, connectors, flexible tube with variable internal diameters and a pressure transducer. Experimental verification of the theoretical analysis above is desirable, and was undertaken. The results are presented and discussed in Appendix D, and agreed well with theoretical predictions, showing that for frequencies below 50 Hz the tubing system introduced only negligible errors.

4.3.4 Multi-Hole Pressure Measurement Probes

The Cobra probe, used to measure the velocity (including pitch and yaw angle) of the airstream, is a 4-hole, high dynamic response pressure measurement probe supplied by TFI (Figure 4.11). It has a 2.6 mm head with the 0.5 mm holes on 4 angled faces allowing it to resolve flow velocity and magnitude within a 45° cone of acceptance (Figure 4.12). The exact specifications of the internal workings of the probe are proprietary to TFI; however, it is known to comprise four differential pressure transducers in the body connected to the head by hypodermic tubing. The same issue of tubing distortion exists for

the probe as for the DPMS described previously; however, in this case the tubing transfer function is determined experimentally. The calibration is performed by the manufacturer and supplied with the system. The Cobra probe is similarly connected to a PC via a data acquisition card, with acquisition controlled Device Control software.

The Cobra probe is a sensitive yet robust instrument which (unlike comparable hot-wire anemometers) is easily configurable, relatively insensitive to temperature drift or damage due to flow field debris. It is ideally suited to outdoor measurement work. The Cobra probe has been used (and its accuracy verified) in a variety of flows by Mousley et al. (1998), Hooper and Musgrove (1997) and Vino (2005) in addition to others cited in the mentioned works. It is thus used throughout this work.

4.4 Conclusions

The experimental equipment and techniques used for the work (shown in Chapters 5 and 6) have been presented. The instrumentation and processes chosen are considered suitable.

The following key points are noted:

- Wind tunnel models comprise a 300 mm finite span flat plate wing with a 150 mm chord. Models were produced with integral pressure taps and mounted on a raised ground plane to negate effects of the wind tunnel boundary layer.
- The RMIT IWT has a 3 m x 2 m x 9 m test section; models were mounted 6 m downstream of the contraction to ensure the turbulence generated by grids upstream was well mixed and homogeneous.
- Pressure measurement was by means of the TFI DPMS, connected to the pressure taps by plastic tubes. Distortion effects due to the tubing system are corrected digitally for both amplitude and phase.
- Turbulence and velocity measurements were made using TFI Cobra probes both in the wind tunnel and outdoors. These robust instruments give good accuracy over a wide operating range.

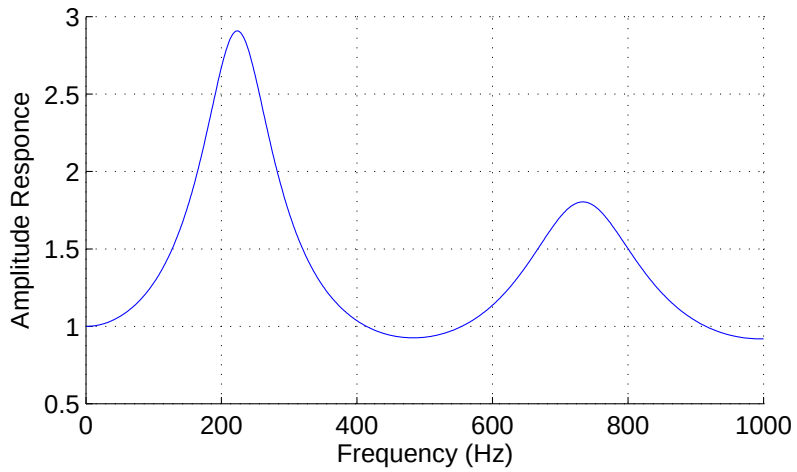

(a)

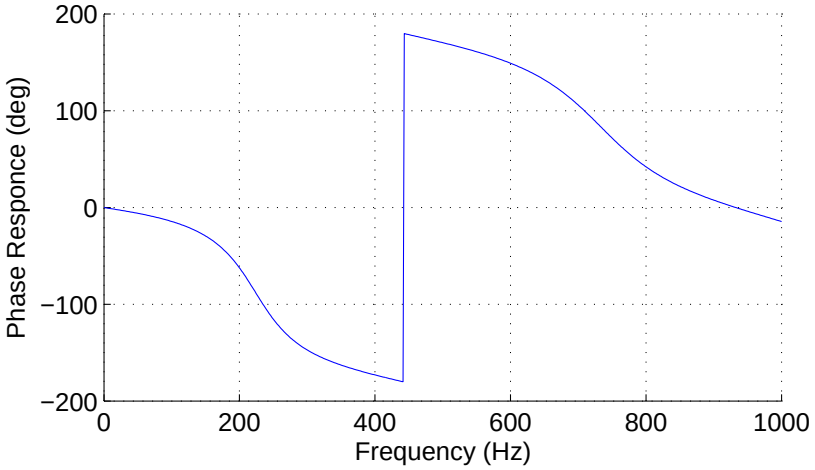

(b)

Figure 4.10: Magnitude (a) and phase (b) distortion of a 300 mm tube of 1 mm diameter

Figure 4.11: TFI 3-hole dynamic Cobra probe

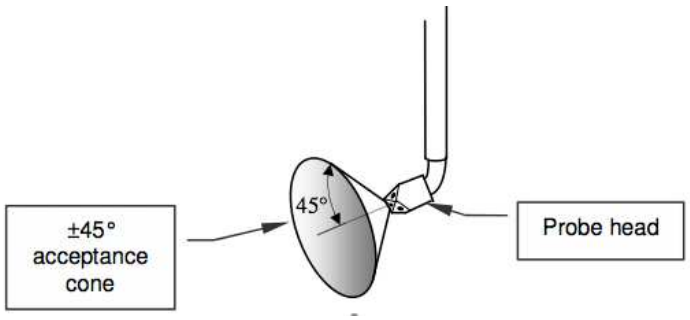

Figure 4.12: Forty-five degree cone of acceptance of the TFI Cobra probe

Chapter 5

Surface Pressure Measurements

This chapter presents experimental results from surface pressure measurements made on a finite flat plate wing (discussed in Chapter 4). Tests were performed in the RMIT Industrial Wind Tunnel at three levels of turbulence replicating atmospheric flows (comparable to those presented in Chapter 3). Turbulence was generated using a series of grids upstream of the test section (detailed in Chapter 4). Time-averaged and dynamic results are presented for pressure coefficients and derived force coefficients.

An overview of instrumentation and procedures used for this work is provided in Chapter 4 and details on the wind tunnel, data post-processing techniques, and spectral analysis can be found in Appendices B to C

5.1 Overview of Data Acquisition and Experimental Procedure

Surface pressures were acquired using a series of pressure taps on the surface of the wing connected to pressure transducers using a known length of tubing. Equipment was calibrated and zeroed before testing and drift was monitored after each test.

Prior to any testing, an extensive procedure was undertaken to ensure the system was free of leaks and that all pressure taps were reading accurately. On completion of initial calibration work, the following procedure was used prior to each test run:

1. Prior to each run (at zero wind) the DPMS sensors were "zeroed"; residual mean voltage on each input channel of the DAQ card was measured and recorded. Zeroing is a function built into TFI DAQ software that ships with the DPMS and is handled internally.

2. On reaching the intended free-stream velocity; ambient temperature, dynamic and static pressure were acquired at a known location within the test section, and pressure data over the flat plate were sampled for 10 minutes at a sample rate of 3 kHz.

3. After sampling, the tunnel was shut down. On returning to the zero wind condition, sensor drift was measured for all channels, and in all cases was found to be negligible.

4. Before, during and after testing the tunnel dynamic and static pressures at the reference location were recorded using spare channels on the DPMS for later analysis.

Measurements were made at incidence between $-20°$ to $+20°$ in $2°$ increments at a wind speed of 10 m/s. The tunnel was stopped between each run and the DPMS re-zeroed. At incidence of $0 - 20°$ in $5°$ degree increments, data were acquired at speeds of 5, 10 and 12.5 m/s to assess the sensitivity of results to changing Re.

The tunnel zero pitch angle was determined by running the tunnel and pitching the model until a symmetrical pressure distribution was obtained. The angle of the mean flow in the IWT at the location of the model was observed to vary slightly depending on the grid configuration used upstream. This point was marked on the ground plane, with all subsequent incidence angles measured from this reference. This process was repeated for each grid and the empty tunnel configuration.

5.2 Overview of Data Post-Processing

Data processing was performed in MATLAB using the procedures discussed in Appendix C; a general overview follows:

1. Once sampled, data were stored by TFI Device Control software in a proprietary format, which was read into MATLAB for processing via a TFI-supplied script. Data were imported into data matrices for each angle of incidence (α), velocity and turbulence level.

2. The local pressure coefficients, C_P, were calculated at each measurement point for each sample in the time series, and then averaged over the sample length to determine the mean pressure distribution over the wing. Lift and moment coefficients were calculated from this lift distribution. Means and standard deviations were calculated for each coefficient time series.

3. Spectral analysis was performed on raw C_P data. The power spectral density of each channel was calculated using Welch's method (detailed in Appendix C).

4. Data were plotted on normalised axes. Contour data are presented using cubic interpolation between points.

5.3 Results and Discussion

Results of tests conducted on flat plate finite wings under a number of turbulent flow conditions are presented and discussed. Results in Section 5.3.1 are shown at a single Re ($Re = 100,000$); the effects of changing Re are explored later in this chapter.

5.3.1 Time-Averaged Pressure Coefficient($\overline{C_p}$)

The mean distribution of C_p was calculated from pressure measurements made at each pressure tap averaged across the 10 minute sample. The $\overline{C_p}$ distribution on the top and bottom surface at an angle of incidence of 6° ($\alpha = 6°$) is shown in Figure 5.1. The results for each of the three turbulence conditions are superimposed on the same plot. In the low turbulence condition ($I_u = 1.5\%$) the results compare well with work by Pelletier and Mueller (2000) (see Chapter 1), although the overall magnitude of the pressure coefficient values are lower, this is likely to be the result of the finite nature of the wing resulting in a local section lift coefficient lower than the 2D case at this chord station. The notable effect of increased levels of free-stream turbulence at this incidence is to reduce the magnitude of the suction peak near the leading edge, whilst producing similar $\overline{C_p}$ values over the remainder of the section downstream.

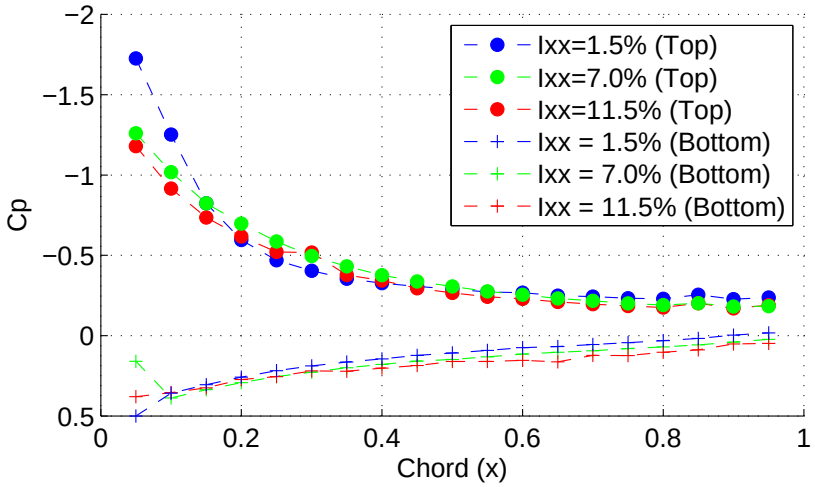

Figure 5.1: $\overline{C_p}$ distribution at $\alpha = 6°$ at three unique I_u

$\overline{C_p}$ distributions for incidence values between +4° and +18° are shown in Figure 5.2. At incidence values below stall, the suction peak appears very close to the leading edge. As incidence is increased, the suction near the leading edge reduces, and in the low turbulence case, a stall condition is reached (defined by reducing C_L) at approximately 8° . The suction peak at <0.05 chord disappears and as

incidence is further increased (for example from $\alpha = 8^\circ$ to 10°). Post stall, the C_p over the suction surface tends to a relatively uniform value of -1. Increased turbulence levels appear to have the effect of delaying the onset of stall (reduction in suction peak) as well as increasing the magnitude of the suction peak at the leading edge.

It should be noted that due to the fineness of the leading edge of the model, there are no pressure taps located near the leading edge within the first 5% of chord. This results in data that does not explicitly show the highest value of the suction peak at low α if it falls within this region. In addition, the stagnation point near the leading edge on the high pressure surface falls within this region at low α hence there is no data point with a $\overline{C_p}$ equal to 1.

To illustrate the change in $\overline{C_p}$ distribution with changing angle of attack, $\overline{C_p}$ is plotted on a contour plot against chord (on the vertical axis) and angle of attack (on the horizontal axis) shown in Figure 5.3. The development of the $\overline{C_p}$ distribution on the suction surface on the wing with increasing angle of attack in the low turbulence (1.5%) configuration in shown in Figure 5.3(a). Figure 5.3(b) and Figure 5.3(c) show medium and high turbulence intensity levels of 7.0% and 11.5% respectively.

Several effects of increasing levels of freestream turbulence are observed in Figure 5.3. Increasing free-stream turbulence intensity delays the onset of stall as characterised by flow separation and reduction of the suction peak near the leading edge at low incidence. Broad chordwise areas of separated flow are indicated in Figure 5.3(a) where after $\alpha = 10^\circ$, C_p values tend to -1. In Figure 5.3(b) this separation is delayed until $\alpha > 15^\circ$, whilst in Figure 5.3(c) separation is not observed at the incidences explored, with a strong suction peak maintained to $\alpha = 20^\circ$. The strongest suction peak at the leading edge is displayed in the highest turbulence case (5.3(c)).

Data confidence in time-averaged data taking into various error sources presented in Chapter 4 is estimated at 0.5%. This is illustrated in Figure 5.4, which shows a single pressure distribution at low turbulence level with data confidence expressed as error bars.

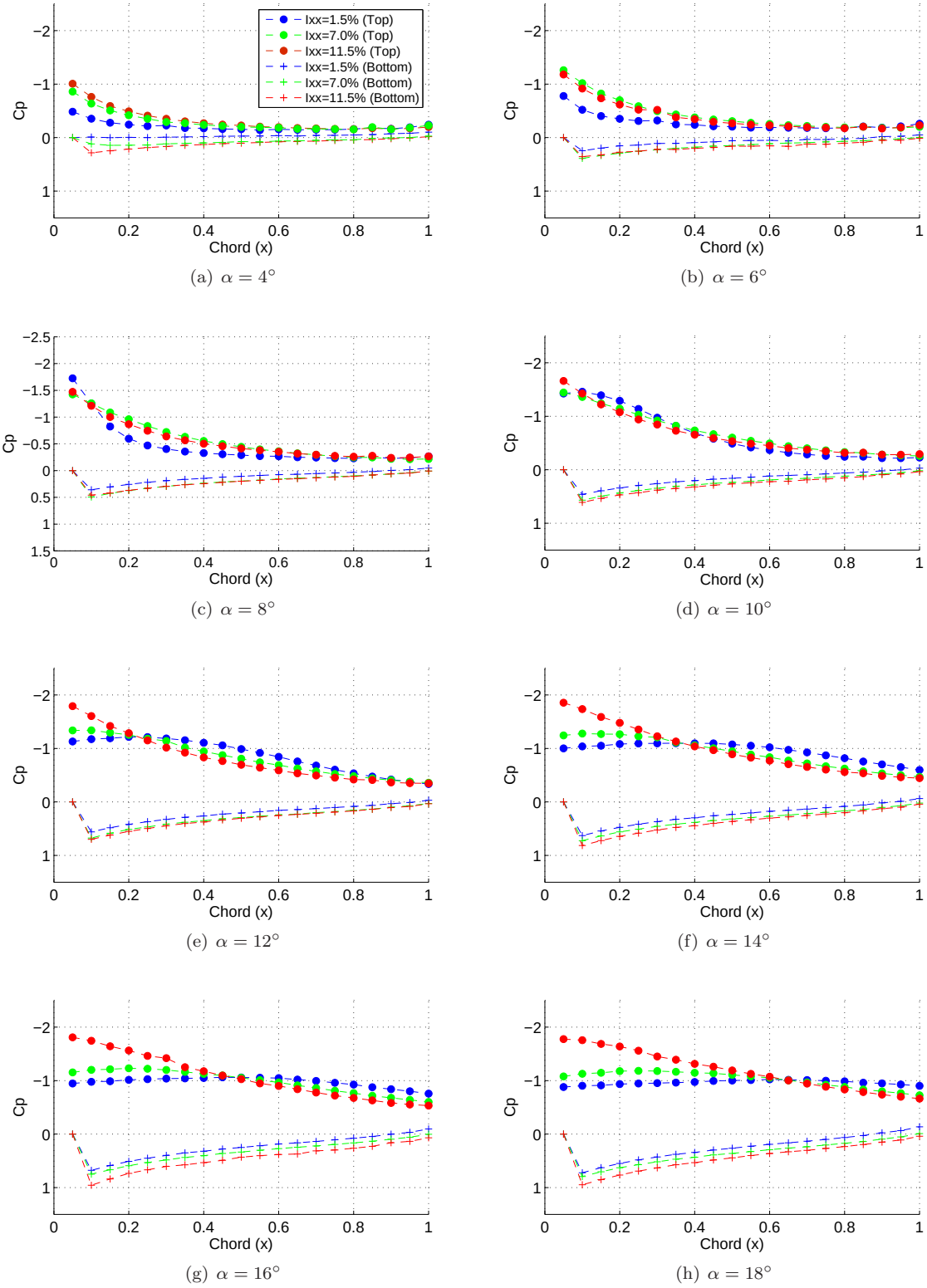

(a) $\alpha = 4°$ (b) $\alpha = 6°$

(c) $\alpha = 8°$ (d) $\alpha = 10°$

(e) $\alpha = 12°$ (f) $\alpha = 14°$

(g) $\alpha = 16°$ (h) $\alpha = 18°$

Figure 5.2: $\overline{C_p}$ distribution on the suction surface plotted against chord and α for turbulence levels 1.5%, 7.0% and 11.5%

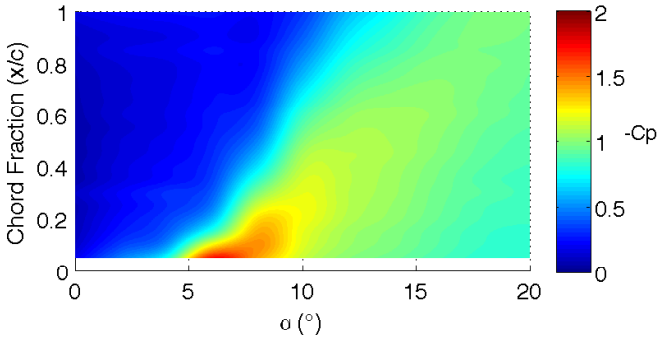

(a) $I_u = 1.5\%$

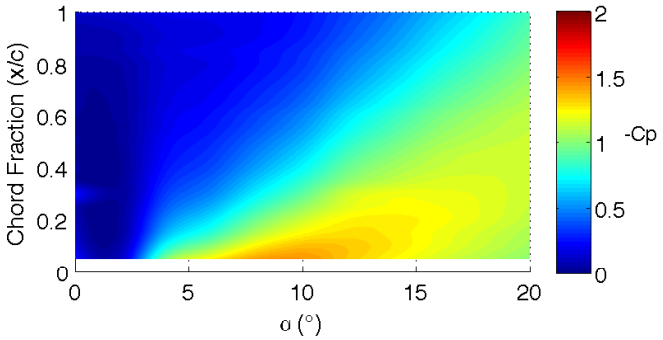

(b) $I_u = 7.0\%$

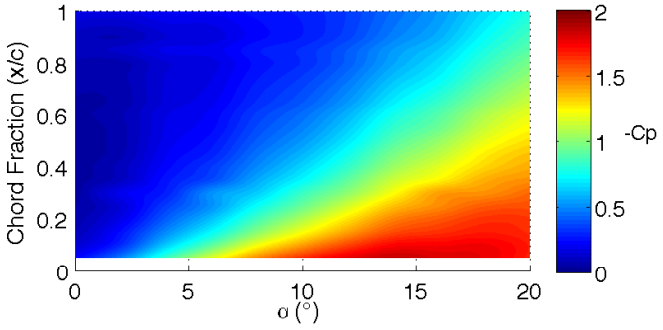

(c) $I_u = 11.5\%$

Figure 5.3: Negative $\overline{C_p}$ distribution on the suction surface plotted against chord and α for turbulence levels (a) 1.5%, (b) 7.0% and (c) 11.5%

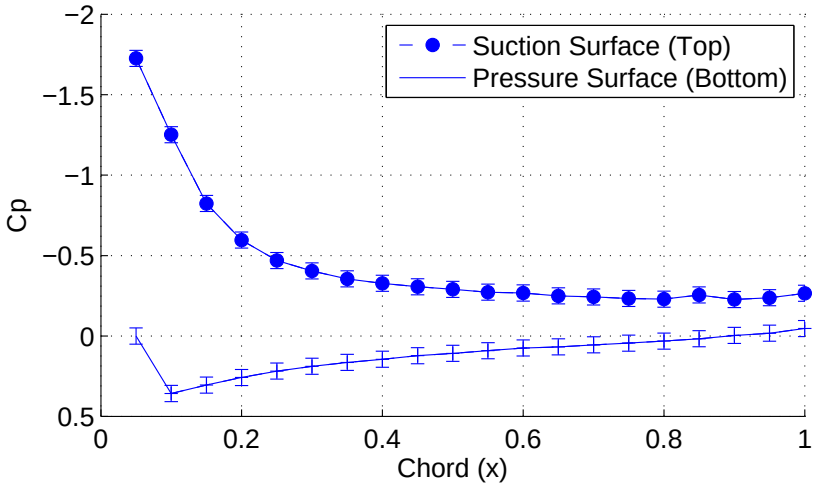

Figure 5.4: Single $\overline{C_p}$ distribution at $\alpha = 6°$ and $I_{xx} = 1.5$ with error bars shown

5.3.2 Standard Deviation of Fluctuating C_p

An indication of the magnitude of fluctuation in surface pressures is provided by the standard deviation of the pressure coefficient (σ_{C_p}), expressed for convenience as a percentage of mean $\overline{C_P}$. Figure 5.5 presents σ_{C_p} at each pressure tap at $\alpha = 6°$ for the three turbulence levels presented in Figure 5.1. The highest standard deviation that occurs is observed close to the leading edge. Increasing freestream turbulence levels increase the standard deviation at all locations on both the suction and pressure surfaces, particularly near the leading edge.

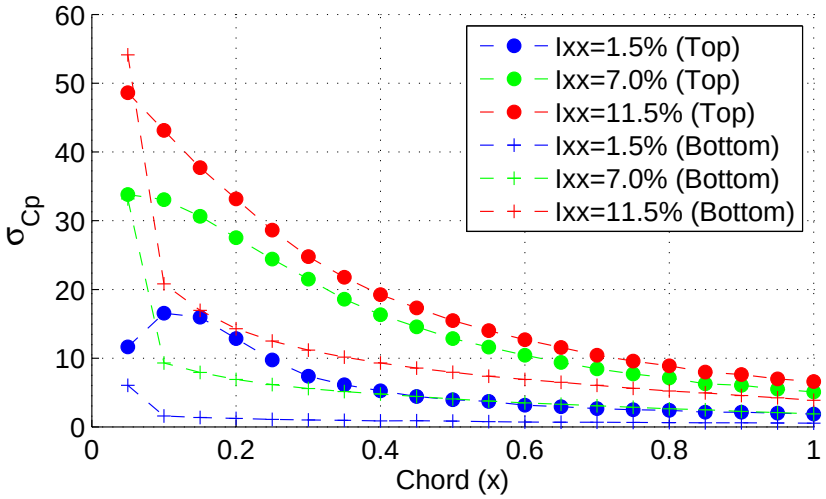

Figure 5.5: The effect of free stream turbulence intensity (I_u) on standard deviation of the Cp distribution (σ_{Cp}) at $\alpha = 6°$ as a percentage of the mean

As with the C_P distribution, the σ_{C_p} distribution is plotted as a contour plot against α and chord. This is shown in Figure 5.6 for the suction surface only, for the three free-stream turbulent conditions.

Figure 5.6(a) shows that only moderate values of σ_{C_p} are observed at the relatively low free-stream turbulence level and that the higher chordwise values of σ_{C_p} are formed close to the areas of high negative C_p. An increase in the intensity of the fluctuating pressure is seen near the leading edge starting at $\alpha = 5°$. As α is increased, the peak moves further aft until approximately $\alpha = 8°$ before it reduces in magnitude and expands to influence most of the wing chord. At the medium turbulence level in Figure 5.6(b) the magnitude of the peak σ_{C_p} is increased, and appears at a lower α (approximately 4°). This peak remains pronounced until $\alpha = 10°$ to 12° and moves slightly aft. Above $\alpha = 10°$ degrees the peak σ_{C_p} reduces and spreads out to a more uniform distribution, consistent with wing stall and separated flow. At the highest turbulence level of 11.5%, shown in Figure 5.6(c), the peak σ_{C_p} starts from $\alpha = 0°$, and remains at the leading edge throughout the test range, increasing in strength and moving aft, characteristic of the delayed onset of stall and separation.

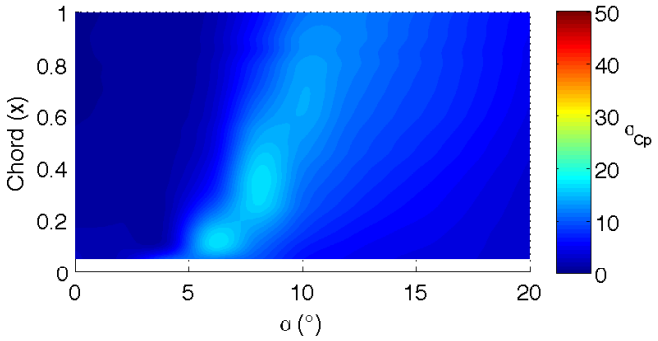

(a) $I_u = 1.5\%$

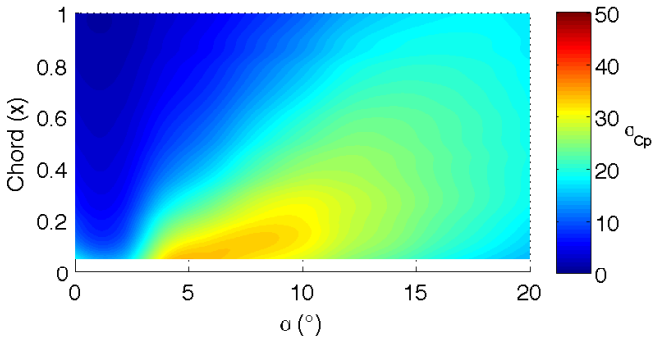

(b) $I_u = 7\%$

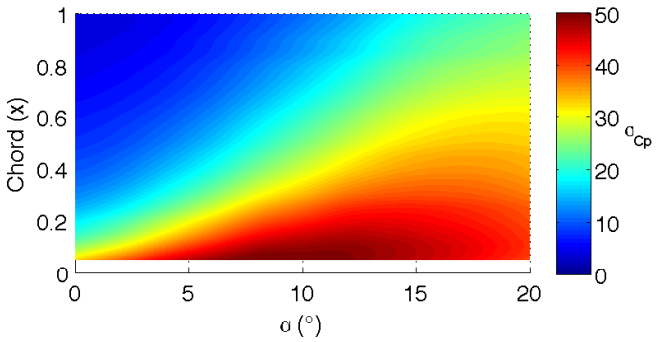

(c) $I_u = 11.5\%$

Figure 5.6: Contours of σ_{C_p} distribution on the suction surface plotted against chord and α for turbulence levels (a) 1.5%, (b) 7% and (c) 11.5%

5.3.3 Analysis of Time-Averaged Forces and Moments

Time-averaged forces and moments are derived by integrating the means of 10 minute samples of pressure distributions. To calculate lift force from the pressure distribution, the wing was numerically divided into a number of discrete segments ($\triangle c$) equal to the number of surface pressure taps (20 on surface). The local mean pressure at each pressure tap was multiplied by each chord segment ($\frac{c}{20}$). The resulting sum of forces gives the total lift produced resolved into the body axis. Using the local C_p at each point, rather than absolute pressure, and non-dimensionalising using a suitable length (chord, c, in this case consistent with convention), the lift coefficient per unit span (C'_L) – as opposed to overall wing lift coefficient – is calculated, as shown in equation 5.1.

$$C'_L = \frac{\sum_{x=c}^{x=0} C_{p_i} \cdot \triangle c}{c} \tag{5.1}$$

The mean section C'_L verses α curves for each of the three turbulence levels (1.5%, 7% and 11.5%) generated in the IWT is shown in Figure 5.7. For the low (1.5%) turbulence condition, the relationship appears to be linear up to approximately $\alpha = 6°$; above $\alpha = 6°$ the gradient of the lift curve increases slightly up to approximately $\alpha = 10$. At $\alpha > 10°$ the relationship becomes non linear and after reaching a peak of $C'_L = 0.97$ at $\alpha = 14°$ reduces slightly. This non-linear behaviour after $\alpha = 10°$ is likely due to flow separation and stall, whilst the increase in gradient at $\alpha = 6°$ is likely due to the presence of a laminar separation bubble, which reattaches to the wing down stream (additional evidence to support this theory is discussed in Chapter 6). For the $I_u = 7\%$ and $I_u = 11.5\%$ cases the gradient closely matches the $I_u = 1.5\%$ upto $\alpha = 6$. The $I_u = 7\%$ and $I_u = 11.5\%$ cases diverge at $\alpha = 12°$. No C'_{Lmax} is observed in either case within the tested range.

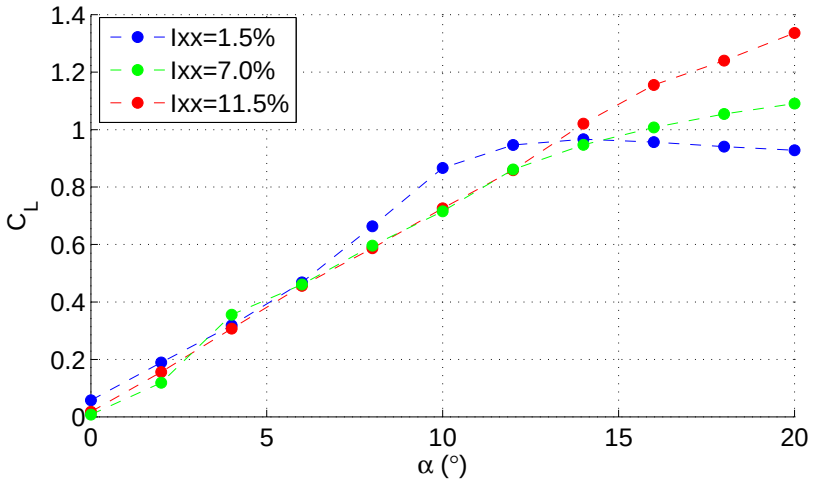

Figure 5.7: Section lift coefficient (C'_L) as a function of turbulence intensity in the body axis system

The section moment coefficient is calculated by summing the force at each location multiplied by the distance of the pressure tap to the $\frac{1}{4}$ chord location (x_i) to give the moment. Summing the individual moments, and dividing by a area ($chord^2$) the moment coefficient is given by, illustrated in Equation 5.2.

$$C'_M = \frac{\sum_{x=c}^{x=0} C_{p_i} \cdot \triangle c \cdot x_i}{c^2} \tag{5.2}$$

The section moment coefficient (C'_M) verses α is shown in Figure 5.8 for all three turbulence levels. In the low turbulence ($I_u = 1.5\%$) case for $\alpha < 8°$, C'_M increases slightly to a maximum negative coefficient of approximately -0.2. At $\alpha > 8°$ the C'_M diverges rapidly to almost -1.4 at $\alpha = 16°$. For the higher turbulence cases, slightly higher overall C'_M at $\alpha < 6°$ is observed, with decreasing moment at $\alpha > 6°$. The rate of change of C'_M at $\alpha > 6°$ is less than that observed in the low turbulence case, suggesting that the flow remains mostly attached to the surface at higher α, although some degree of separation is present.

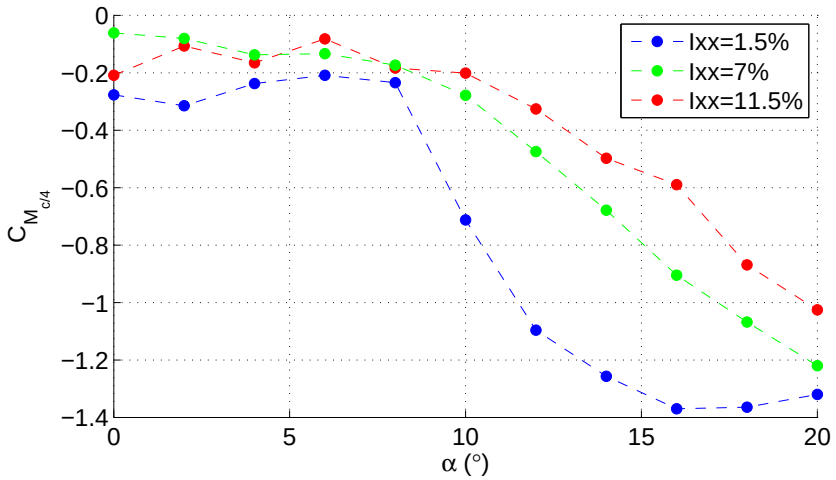

Figure 5.8: Pitching moment (C'_M) as a function of turbulence intensity in the body axis system

5.3.4 Analysis of Time-Variable Forces and Moments

The mean C'_L and C'_M over the entire 10 minute sample length are shown respectively in Figures 5.7 and 5.8, and the standard deviation of C'_L and C'_M are shown in Figures 5.10 and 5.9. Standard deviation gives an indication of the magnitude of the fluctuations in the signal, and is expressed here as a percentage of the mean as illustrated in Equation 5.3. Its worth noting that as the standard deviation (σ) is divided by the mean, as $\alpha \to 0$, $C'_L \to 0$ and $\sigma_{C'_L} \to \infty$, as seen in Figure 5.9(a).

$$\frac{\sigma C_L}{\overline{C_L}} \times 100\% \tag{5.3}$$

Mean section lift coefficients, $\sigma C'_L$, as a percentage of the mean and as a function of α for each of the three turbulence levels are shown in Figure 5.9 . In each case, σ reduces with increasing α, though this is largely a function of the increasing mean C_L as shown in Figure 5.7. In the low turbulence case, from $\alpha = 4^\circ$ the $\sigma C'_L$ in consistant at approximately 10%. With increasing turbulence the $\sigma C'_L$ increases, with levels of 50% at $\alpha = 10^\circ$ for I_u=11.5%. No discontinuities are evident in the relationship between $\alpha = 4^\circ$ and $\sigma C'_L$.

The relationships between $\sigma C'_M$ and α are shown in Figure 5.10, indicating a maximum at $\alpha = 8^\circ$ for the low and medium turbulence cases, and at $\alpha = 6^\circ$ for the high turbulence case. $\sigma C'_M$ is expressed as a percentage of the mean, and shows that variations of three times the mean are present within one standard deviation. The maximum $\sigma C'_M$ corresponds to the transition from relatively stable C_M values to a strong negative gradient in Figure 5.8.

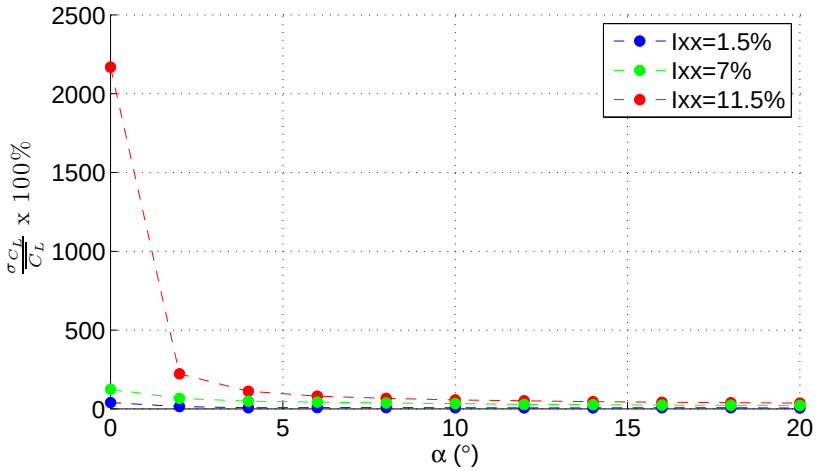

(a)

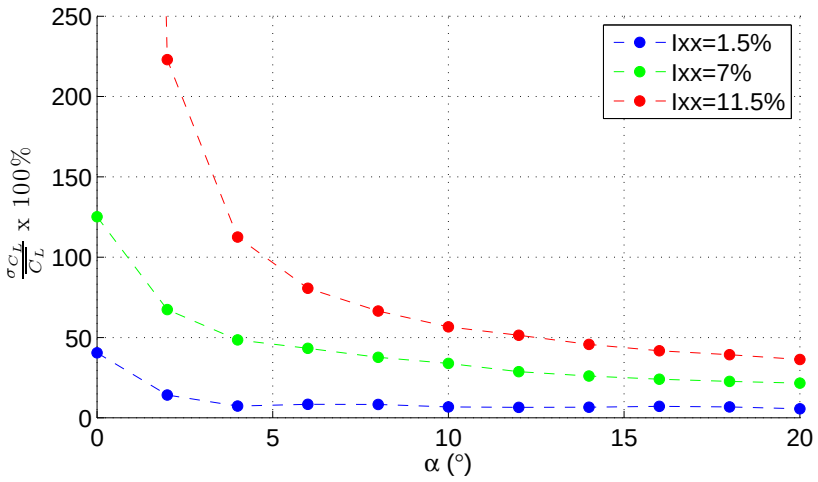

(b)

Figure 5.9: Standard deviation of lift coefficient expressed as a percentage of the mean ($\sigma_{C_L'}$) with α, and three levels of turbulence intensity (I_u). The difference in scale between 5.9(a) and 5.9(b) illustrate how $\frac{\sigma C_L}{C_L}$ tends infinity at low α. ($U = 10$ m/s in all cases)

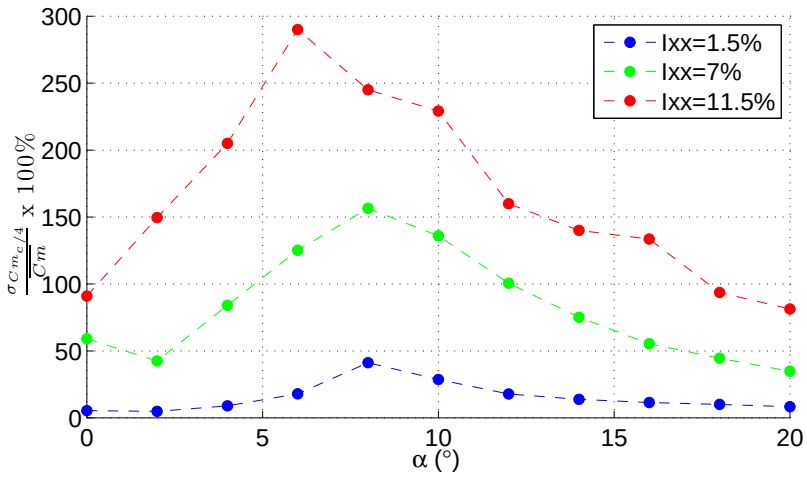

Figure 5.10: Standard deviation of pitching moment coefficient expressed as a percentage of the mean ($\sigma C'_M$) with α, and three levels of turbulence intensity (I_u)

5.3.5 Spectral Analysis of Fluctuating Pressure Coefficient

Power Spectral Density (PSD) presents the energy in a fluctuating signal at different frequencies. It is calculated via Welch's methods, and described in Appendix C. Power spectral density can be calculated for each pressure tap on the wing surface, such as that shown in Figure 5.11. This is a useful in determining the frequency of key oscillations at a given location; however, it is desirable to present this information in a more concise way allowing visualisation of the magnitude of the spectral peak and comparison to other chordwise locations at each incidence and normalised against velocity. Normalised frequency is used to ensure independence of results forom freestream velocity, and is a quantity known as wave number, expressed in Equation 5.4.

$$k = \frac{f}{u} \tag{5.4}$$

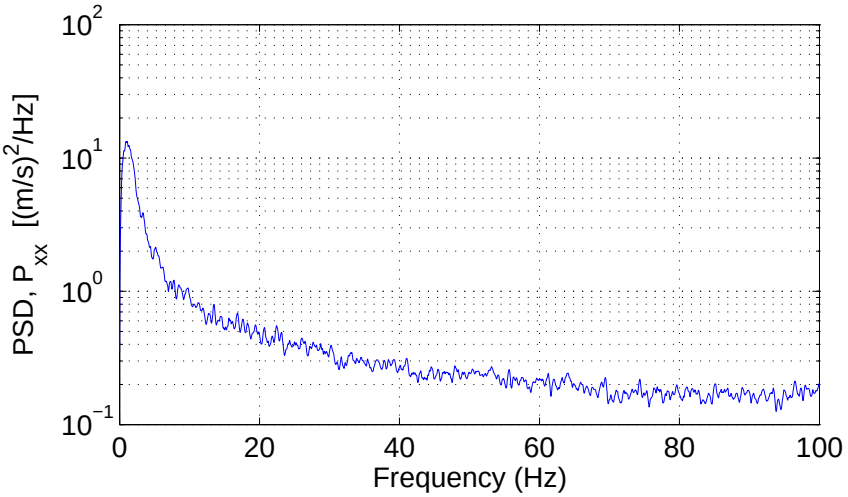

Figure 5.11: Example of a power spectral density plot of a single pressure tap at 10% chord on the suction surface at a incidence of 6°

The PSDs of the pressure distribution from $\alpha = 2°$ to $\alpha = 20°$ in increments of 2° are shown in Figures 5.12 to 5.21. In these figures, power is plotted against normalised frequency (f/u) and presented as a surface plot with chord station on the vertical axis and normalised frequency ($\frac{Hz \cdot s}{m}$) on the horizontal axis. The power level of the signal is given by a colour scale. This presentation allows the visualisation of the amplitude and frequency of spectral peaks in relation to chord position as angle of incidence is varied (as shown in Figure 5.6). The three sub-figures in each figure show the results for each of the three turbulence levels, illustrating the effect of increasing turbulence on the transience in the pressure distribution.

5.3.5.1 Effect of Increasing Incidence (α) in Low Levels of Free-Stream Turbulence

The standard deviations of pressure fluctuations as a function of α and chord are presented in Figure 5.6 and show that in the low turbulence condition as α is increased the σ_{C_p} indicates an initial peak which then spreads and becomes more uniform across the wing chord as α is increased further. Increasing the free-stream turbulence level causes the magnitude of the peak to increase and remain at the leading edge at higher α, resulting in a delay in separation and stall. A similar trend is observed in the frequency domain. A region of high spectral energy is visible in Figure 5.13(a) (highlighted in red) near the leading edge (at the bottom of figure). The energy of this peak is spread between 0.1 Hz and 5 Hz with the peak at approximately 1 Hz. As α is increased this peak increases in power and frequency, and moves aft. Figure 5.14(a) shows at $\alpha = 6°$ the high energy region extends to approximately 40% chord for most of the frequency range, with a maximum at approximately 1 Hz. At $\alpha > 8°$ the spectral peak moves further aft and reduces in power, "detaching" from the leading edge to form a peak at the mid chord point (Figure 5.15(a)). Increasing α further sees this "bubble" move further aft towards the trailing edge before spreading out into a even "noise" at frequencies below 10 Hz.

5.3.5.2 Effect of Increasing Free-Stream Turbulence

At higher turbulence levels, the peak C_p at the leading edge is an order of magnitude stronger than in the low turbulence case at low α as seen in Figures 5.12(b) and 5.12(c). The peak is also broader extending further aft. At $\alpha = 2°$ the spectral peak extends aft to 40% chord at $I_u = 7\%$ (Figure 5.13(b)) and 60% chord at $I_u = 11.5\%$ (Figure 5.13(c)). This peak also extends to a higher frequency range up to 20 Hz at $I_u = 7\%$ and 50 Hz at $I_u = 11.5\%$. As α is increased, the spectral peak broadens and extends further aft; however, it does not show the same "bubble" behaviour as in the low turbulence case, remaining attached to the leading edge and extending over the whole wing chord.

5.3.5.3 Notes on Data Acquisition and Accuracy

Spectral content is shown in Figures 5.12 to 5.21 up to 100 Hz. Data were sampled at a rate of 3 kHz; however, the tubing system connecting the pressure tap to the sensor effectively dampens amplitude response at higher frequencies, limiting the useful frequency response of the system to approximately 300 Hz (discussed in Chapter 4). As there was little spectral power in the signal observed above approximately 50 Hz, the restricted range shown in Figures 5.12 to 5.21 is deemed representative. Some noise beyond this range is attributable to the discrete Fourier transform (implemented as a fast Fourier transform, or FFT) algorithm used to generate the spectral plots.

Welchs' method takes a sample, in this case 10 minutes, and breaks it into discrete blocks. The FFT on each block is calculated and then the average of each block is taken to give a smoother PSD. There is a trade off between block size and smoothness, with more blocks giving a smoother result,

but at the expense of frequency resolution at the low frequency end, which requires long sample lengths. As resolution in the low frequency range is of importance (since initial results showed little energy at high frequency), spectral smoothness was compromised for resolution. Further details of Welchs' method are provided in Appendix C.

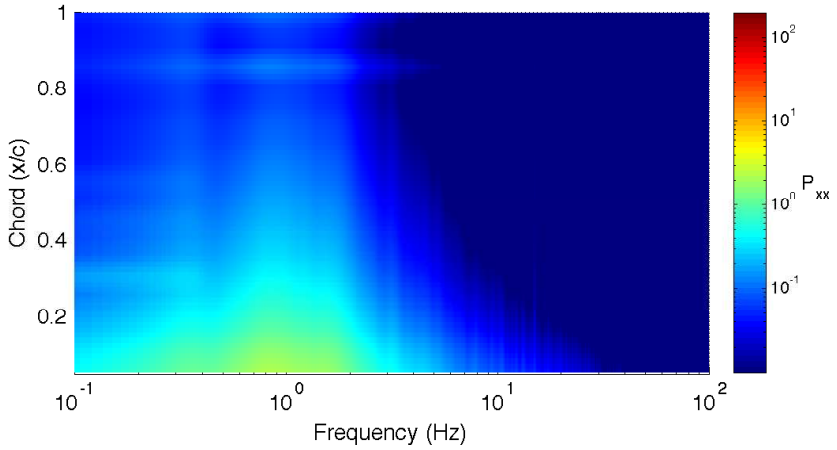

(a) $I_u = 1.5\%$

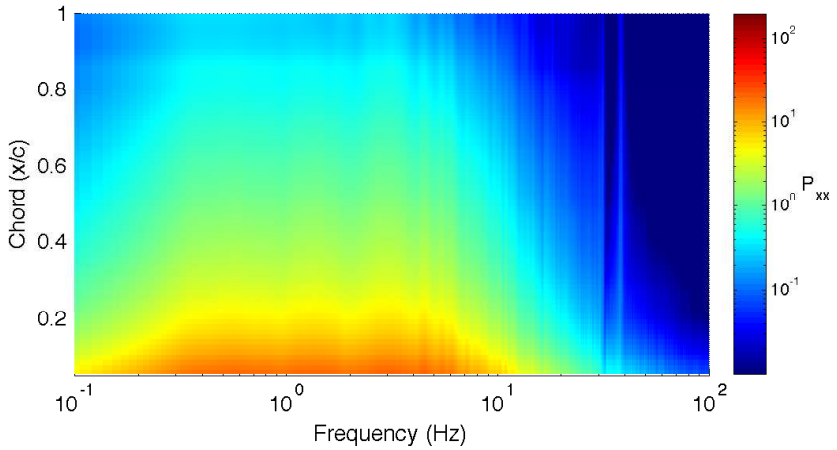

(b) $I_u = 7\%$

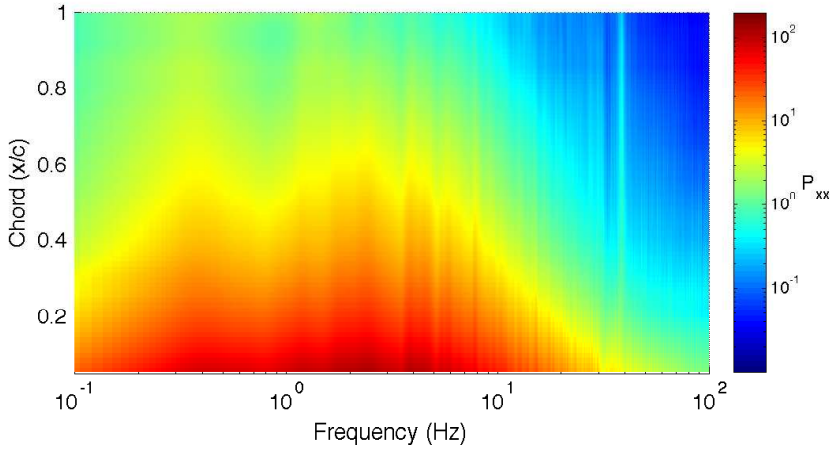

(c) $I_u = 11.5\%$

Figure 5.12: PSD plotted against $\frac{f}{U}$ shown as a surface plot over the wing chord for $\alpha = 2°$

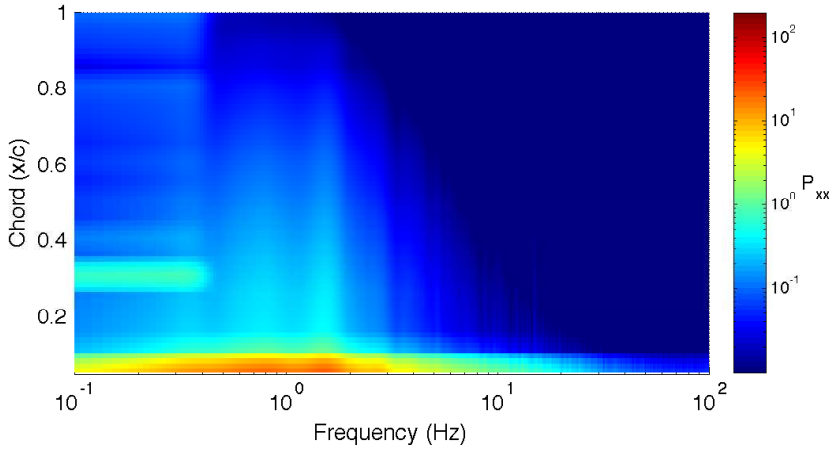

(a) $I_u = 1.5\%$

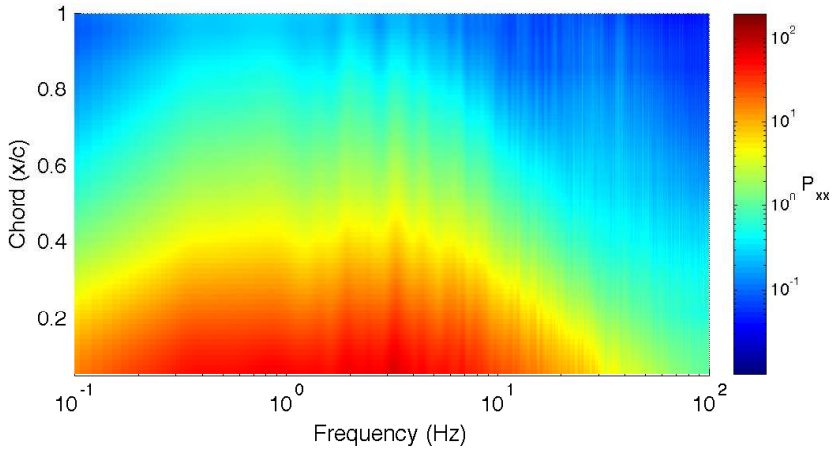

(b) $I_u = 7\%$

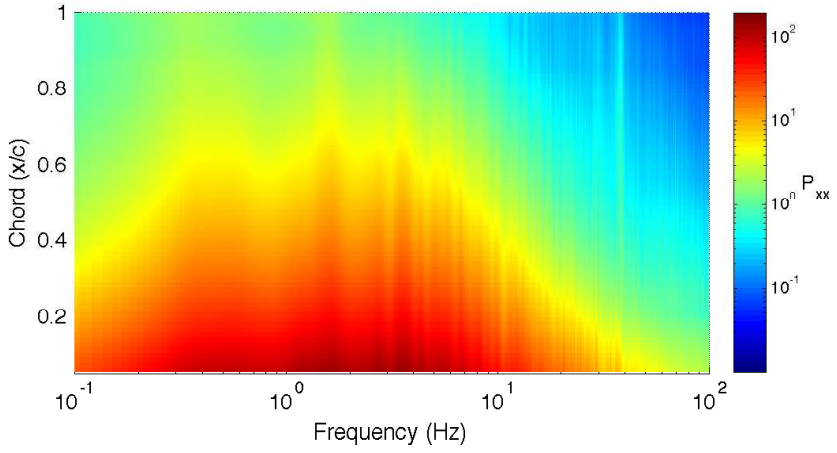

(c) $I_u = 11.5\%$

Figure 5.13: PSD plotted against $\frac{f}{U}$ shown as a surface plot over the wing chord for $\alpha = 4°$

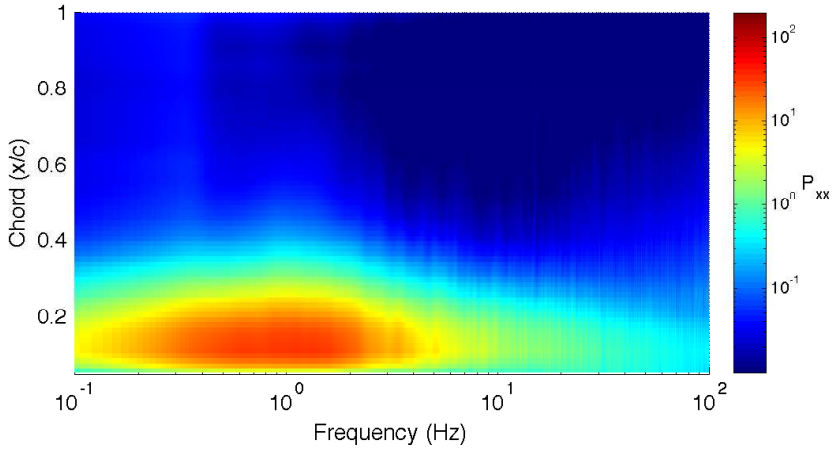

(a) $I_u = 1.5\%$

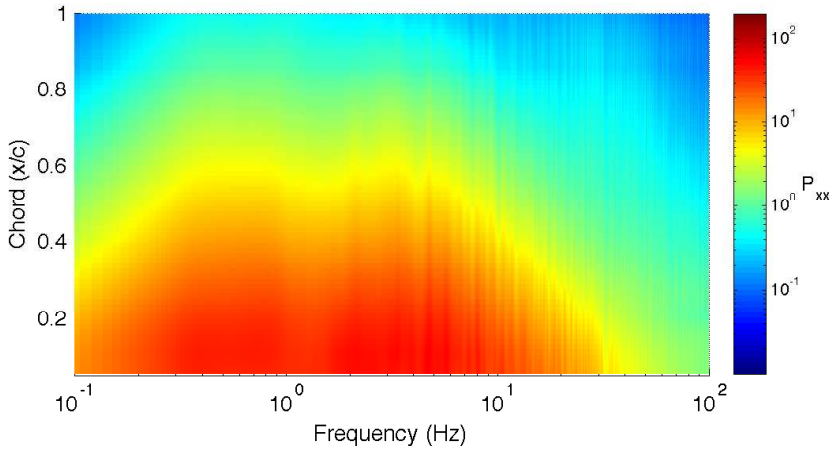

(b) $I_u = 7\%$

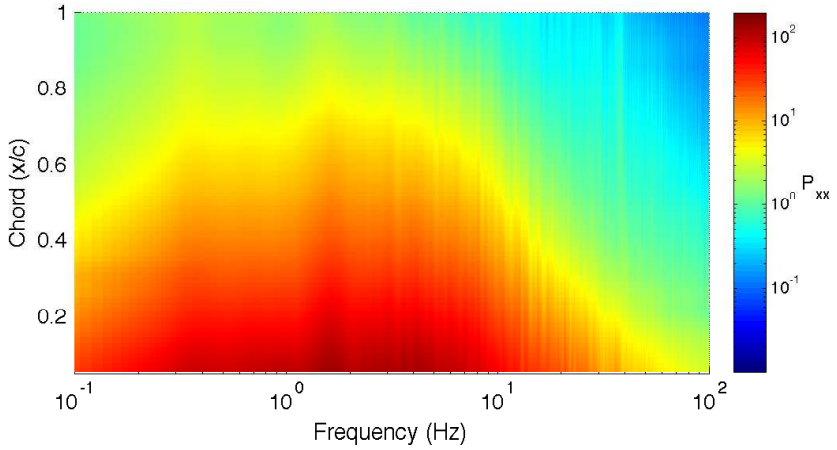

(c) $I_u = 11.5\%$

Figure 5.14: PSD plotted against $\frac{f}{U}$ shown as a surface plot over the wing chord for $\alpha = 6°$

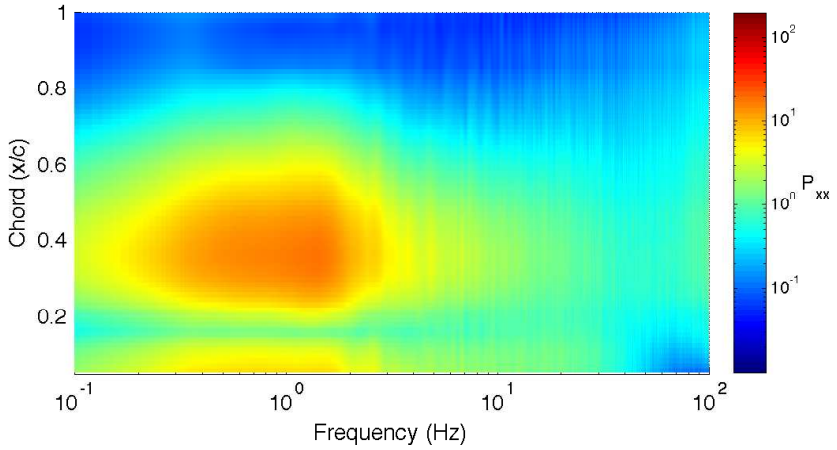

(a) $I_u = 1.5\%$

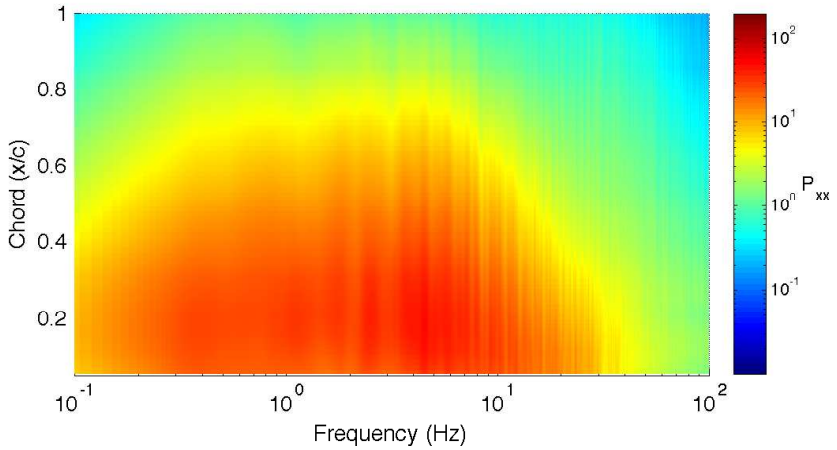

(b) $I_u = 7\%$

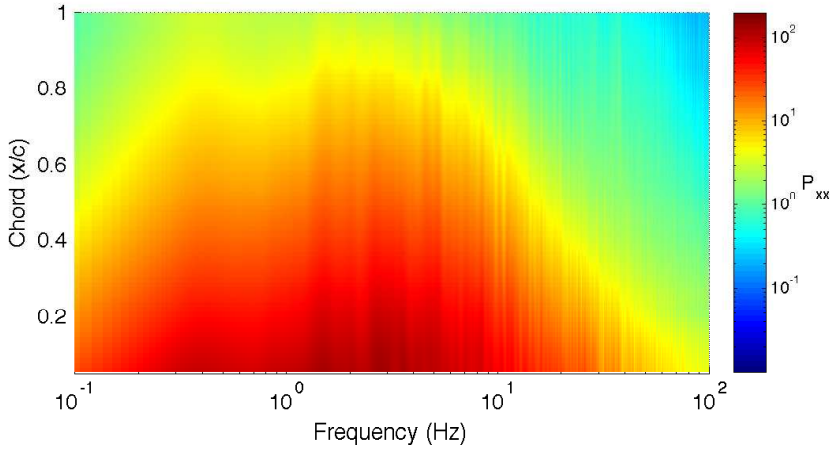

(c) $I_u = 11.5\%$

Figure 5.15: PSD plotted against $\frac{f}{U}$ shown as a surface plot over the wing chord for $\alpha = 8°$

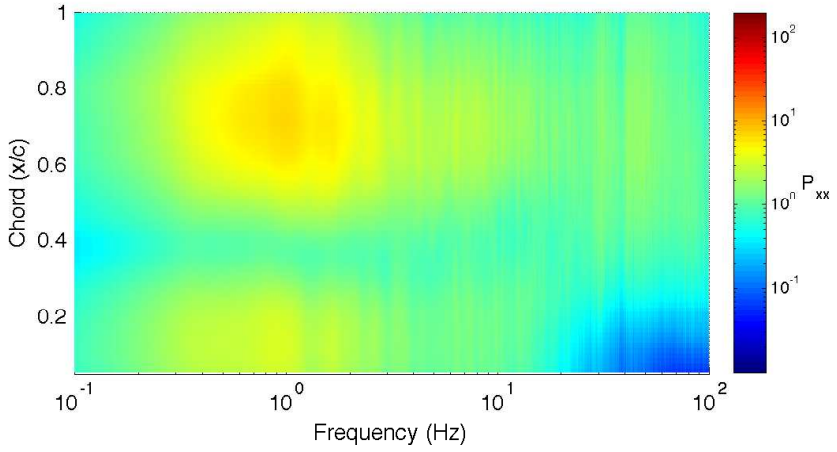

(a) $I_u = 1.5\%$

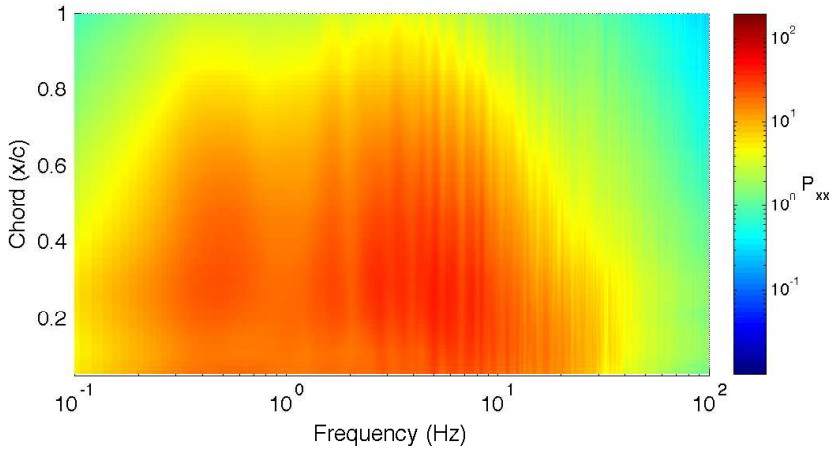

(b) $I_u = 7\%$

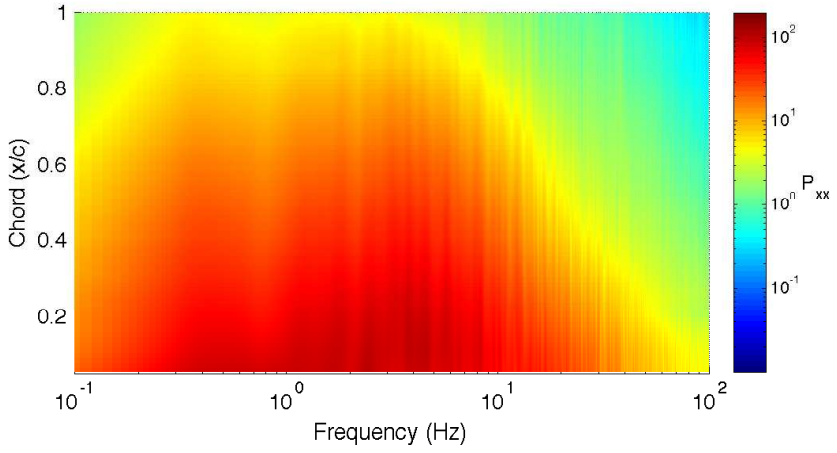

(c) $I_u = 11.5\%$

Figure 5.16: PSD plotted against $\frac{f}{U}$ shown as a surface plot over the wing chord for $\alpha = 10°$

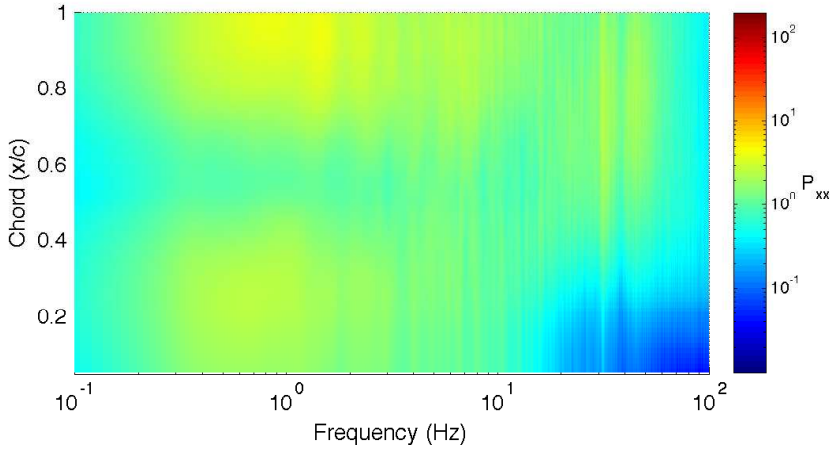

(a) $I_u = 1.5\%$

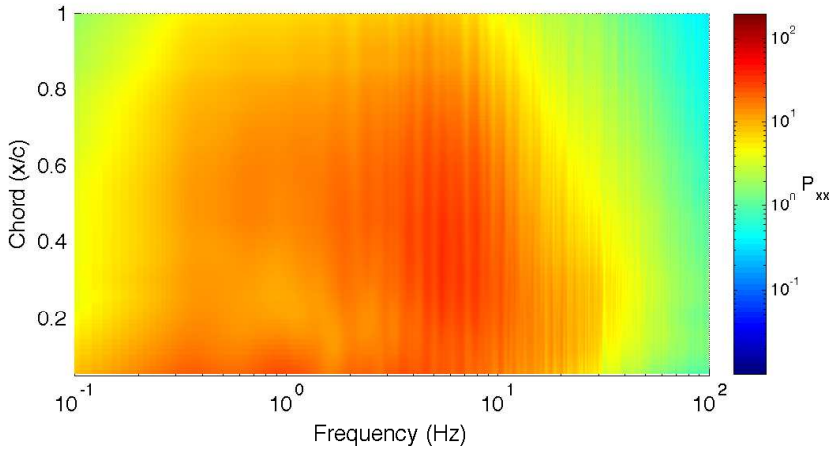

(b) $I_u = 7\%$

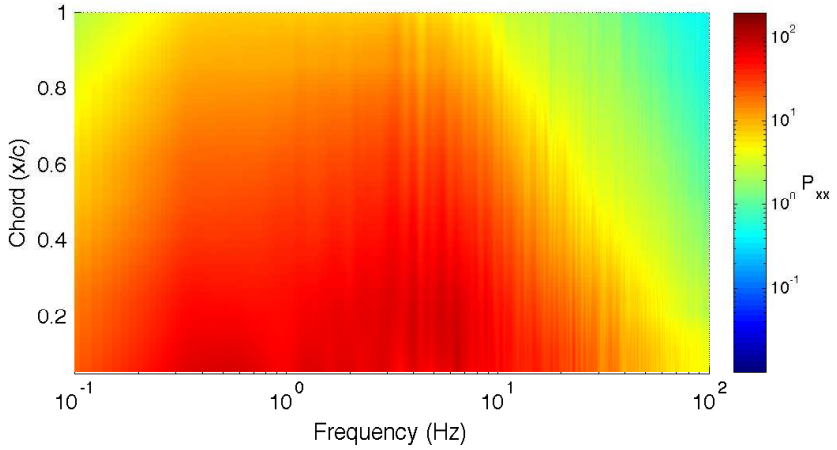

(c) $I_u = 11.5\%$

Figure 5.17: PSD plotted against $\frac{f}{U}$ shown as a surface plot over the wing chord for $\alpha = 12°$

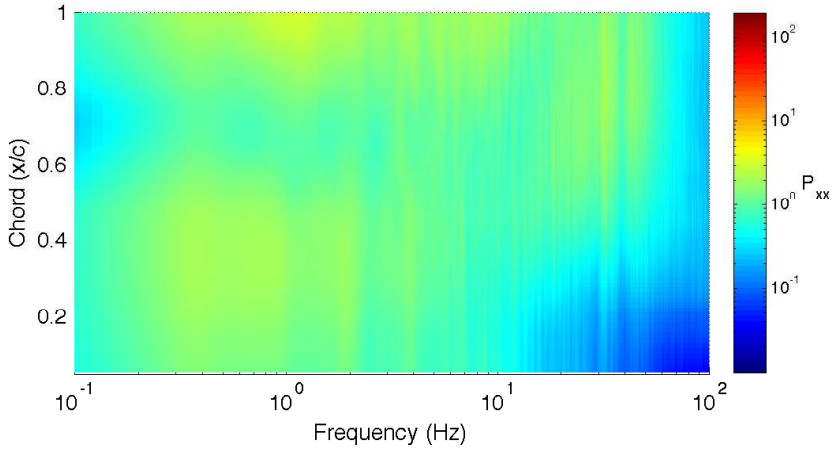

(a) $I_u = 1.5\%$

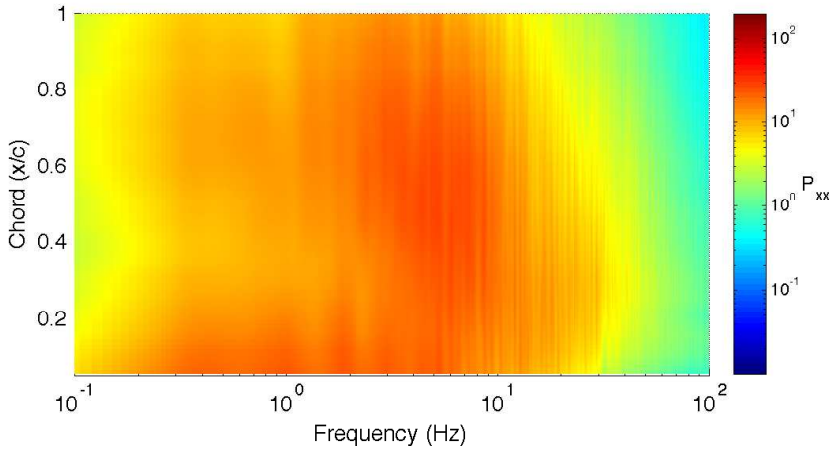

(b) $I_u = 7\%$

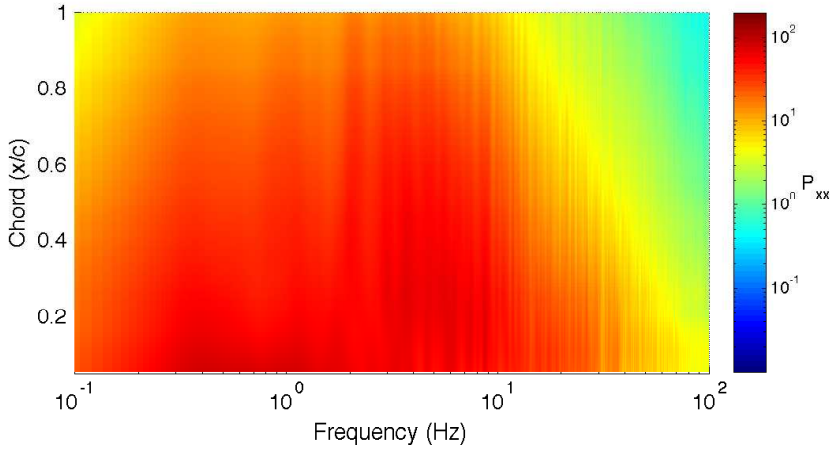

(c) $I_u = 11.5\%$

Figure 5.18: PSD plotted against $\frac{f}{U}$ shown as a surface plot over the wing chord for $\alpha = 14°$

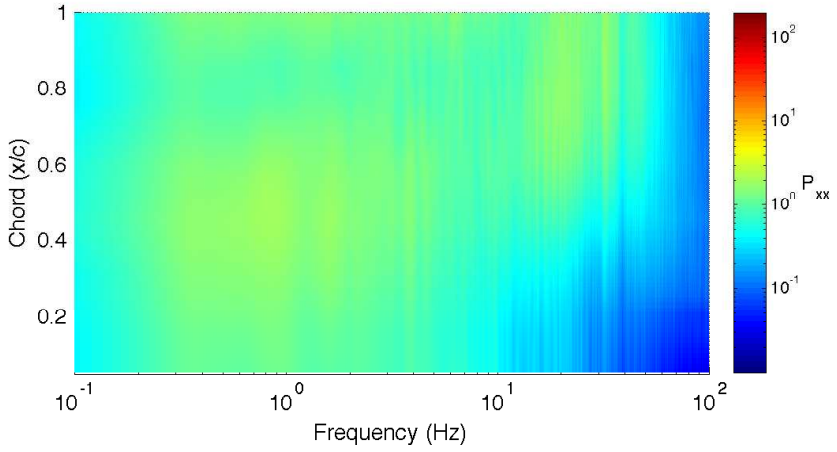

(a) $I_u = 1.5\%$

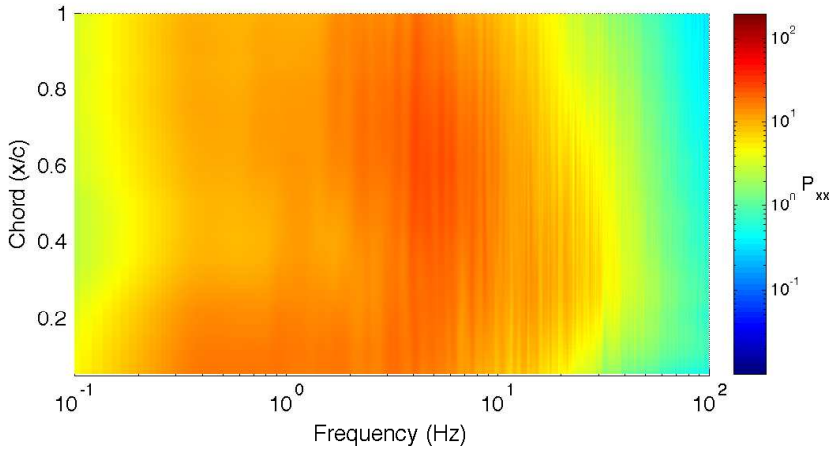

(b) $I_u = 7\%$

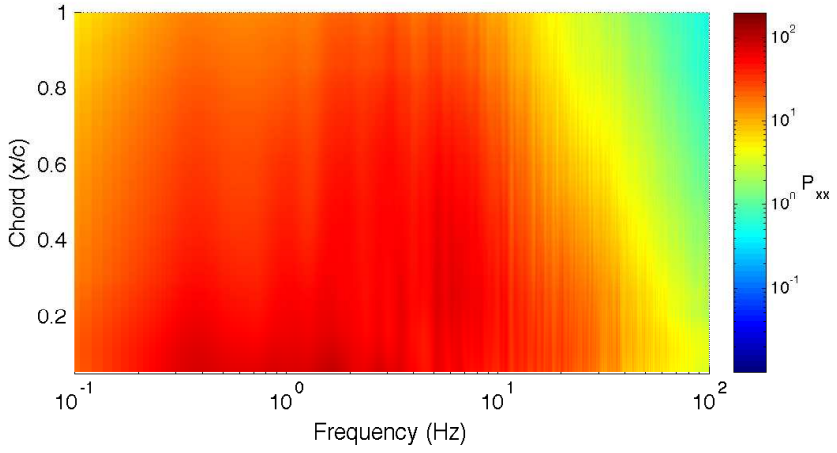

(c) $I_u = 11.5\%$

Figure 5.19: PSD plotted against $\frac{f}{U}$ shown as a surface plot over the wing chord for $\alpha = 16°$

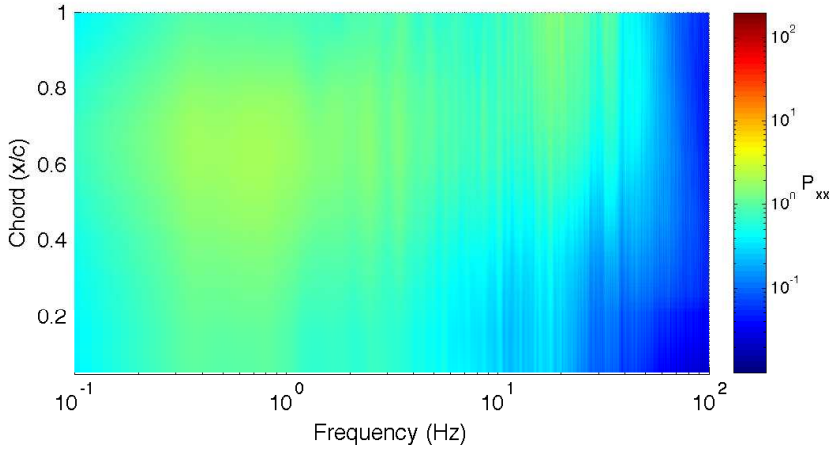

(a) $I_u = 1.5\%$

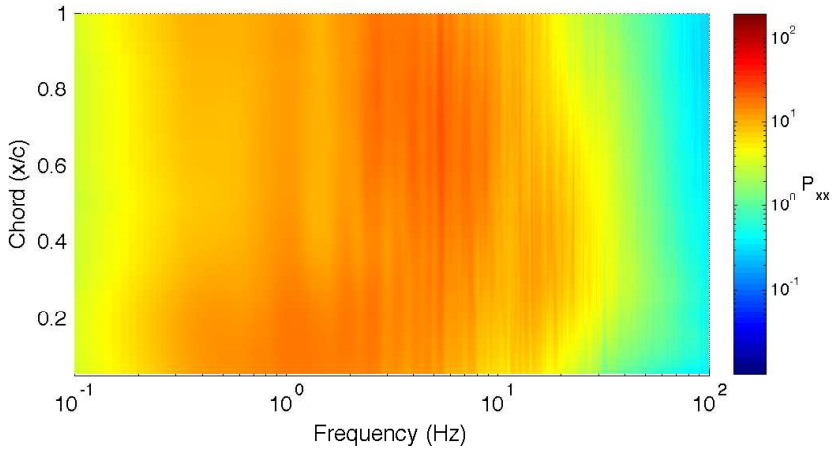

(b) $I_u = 7\%$

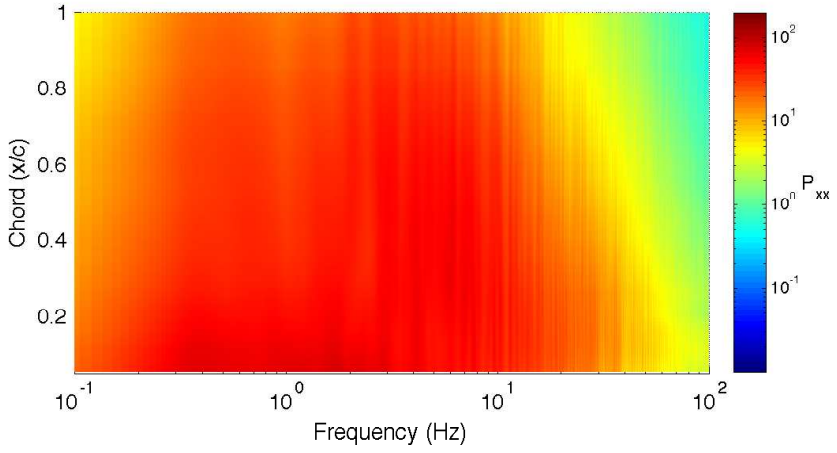

(c) $I_u = 11.5\%$

Figure 5.20: PSD plotted against $\frac{f}{U}$ shown as a surface plot over the wing chord for $\alpha = 18°$

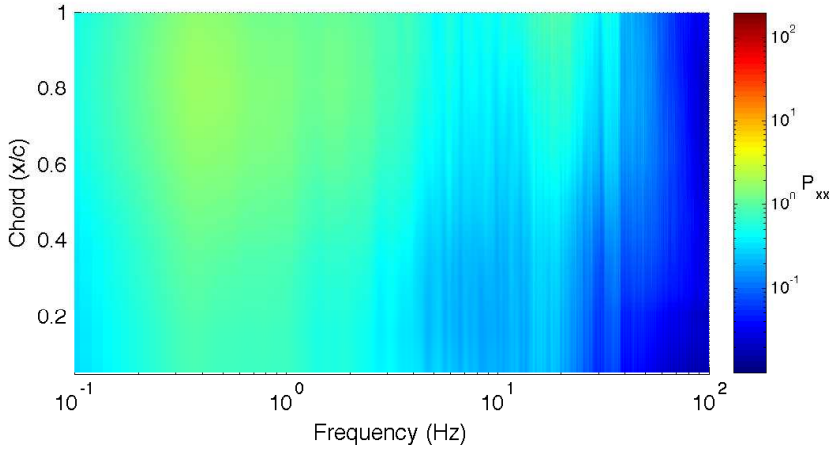

(a) $I_u = 1.5\%$

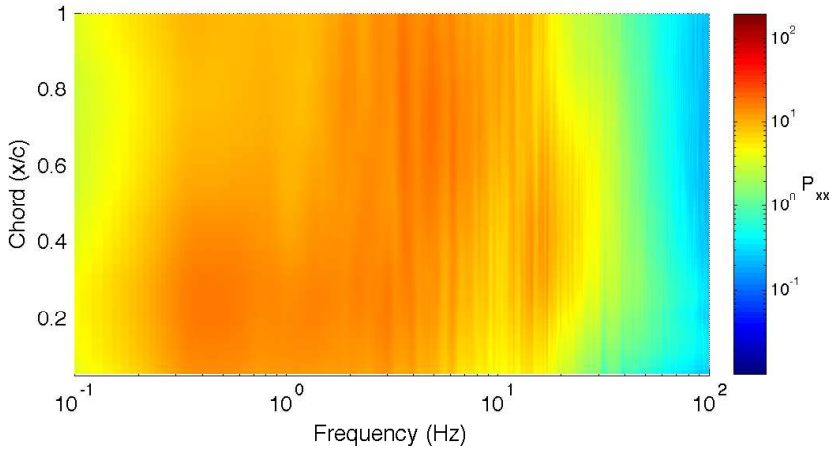

(b) $I_u = 7\%$

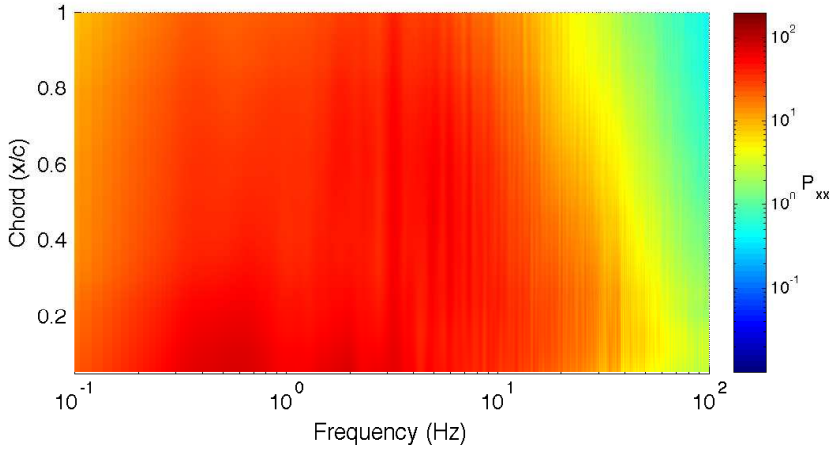

(c) $I_u = 11.5\%$

Figure 5.21: PSD plotted against $\frac{f}{U}$ shown as a surface plot over the wing chord for $\alpha = 20°$

5.3.6 Effect of Variation in Reynolds Number

The operating Re provides an indication of the state of the boundary layer on the surface, and (in smooth flow) specifically indicates if it is likely to be laminar or turbulent. This is of critical concern when studying laminar separation phenomena, as the state of the boundary layer dictates the presence of laminar separation and reattachment.

The results presented in this chapter are based on data taken at a single wind-tunnel velocity (10 m/s) corresponding to a chord Re of the model of approximately 1×10^5. To determine the influence of Re (and hence flight speeds) the sensitivity of results to Re are assessed.

Surface pressure measurements were made at Re of 5×10^4, 1×10^5 and 1.2×10^5, which represent the Re range commonly associated with MAV flight as discussed in Chapter 1. Measurements at higher Re were not made due to structural limitations of the wind tunnel models and the resulting high static loads on the model at higher wind speeds.

5.3.6.1 Influence of Reynolds Number on Mean Forces and Moments

The effect of Re on C_L and C_M is shown in Figures 5.22 and 5.23 respectively. Both C_L and C_M show negligible change over the tested α range indicating that over this range the results are Re independent. Additional α were not tested to reduce the size of the test matrix; however, further testing was done at different turbulence levels, the results of which show negligible Re dependance.

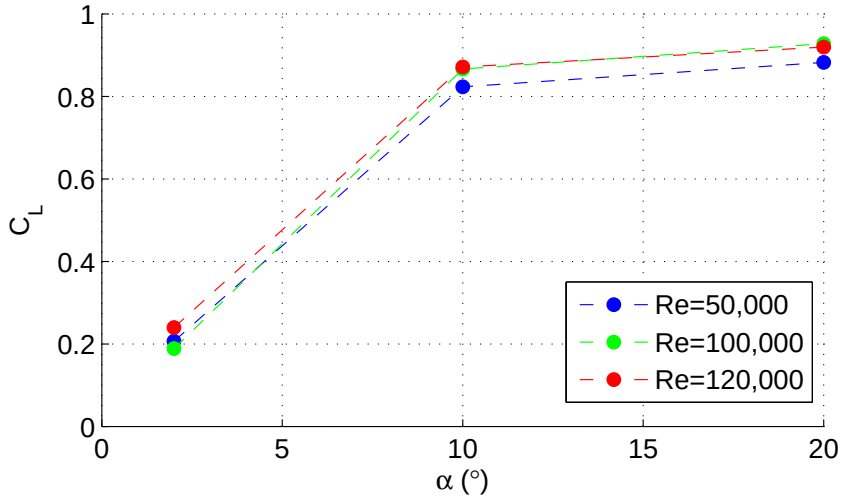

Figure 5.22: C_L for α of 2° , 10° and 20° plotted for Re of 5×10^4, 1×10^5 and 1.2×10^5 in low turbulence conditions ($I_U = 1.5\%$)

5.3.6.2 Sensitivity of Changing Reynolds Number on Pressure Distribution

Figure 5.24 shows the pressure distribution (C_P) for Re of 5×10^4, 1×10^5 and 1.2×10^5 at $\alpha = 2°$, $\alpha = 10°$ and $\alpha = 20°$. In all cases there is little change with increasing Re within the range tested, suggesting that results are independent of Re, at least below generally accepted transitional Re in smooth flow (1×10^6). The only clear variation is in Figure 5.24(b) which shows slight variation at mid chord corresponding to a region of high unsteadiness in Figure 5.6. The variation may be due to either decreased measurable accuracy due to the higher unsteadiness in that region at that α range, or a change in the level of unsteadiness with changing Re.

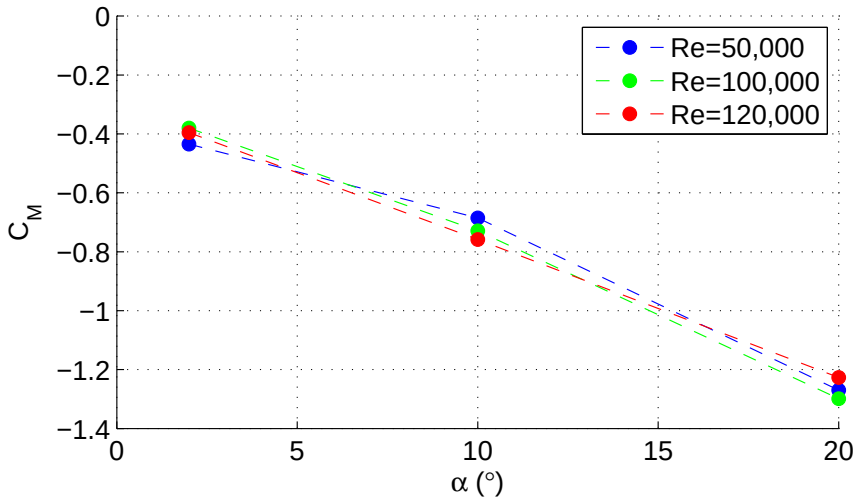

Figure 5.23: C_M for α of 2° , 10° and 20° plotted for Re of 5×10^4, 1×10^5 and 1.2×10^5 in low turbulence conditions ($I_U = 1.5\%$)

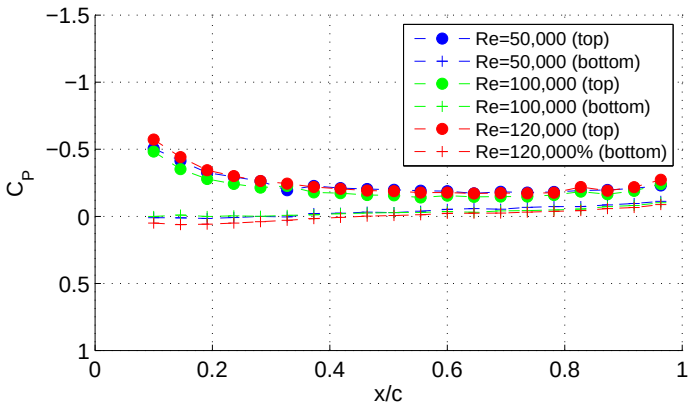

(a) $\alpha = 2°$

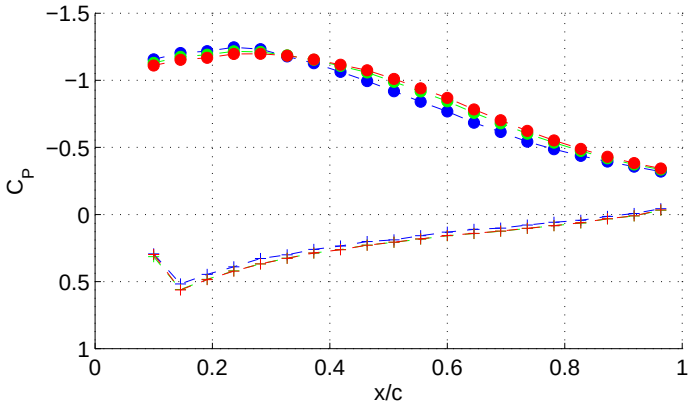

(b) $\alpha = 10°$

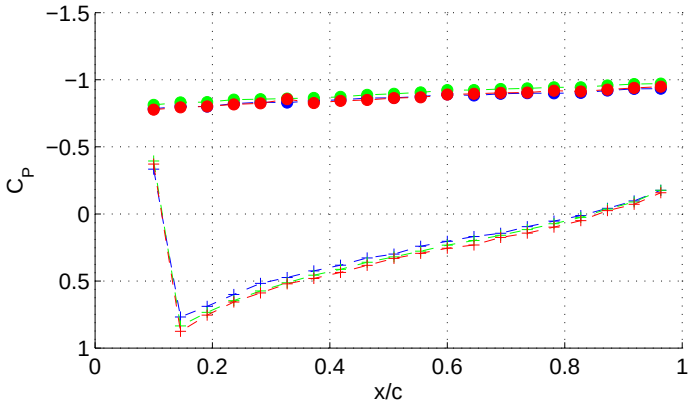

(c) $\alpha = 20°$

Figure 5.24: C_P for Re of 5×10^4, 1×10^5 and 1.2×10^5 at $\alpha = 2°$, $\alpha = 10°$ and $\alpha = 20°$ in low turbulence conditions ($I_U = 1.5\%$) (Legend is shown only in subfigure (a) for clarity)

5.4 Sources of Errors and Influence on Results

Any experimental investigation contains certain errors which effect the quality of the measurements and therefore the accuracy of the results. It is an important part of the experimental process to identify the sources of errors and consider their influence on the results and any subsequent bias that may be placed on the conclusions drawn from the work.

The following are a some of the sources of error identified in this work and their potential effects on the results:

- Wind tunnel flow quality: The quality of the flow in the wind tunnel can have a large influence on the measured results such as forces and moments, as well as dynamic effects generated by unsteadiness in the flow field. Freestream turbulence intensity in the low turbulence case appears to be a critical case as from the results presented in this Chapter it appears to have a significant effect on results. The characteristics of the IWT used are well know and have been examined by multiple sources, as discussed in Chapter 4 and Appendix B, resulting in a well known environment for testing. Furthermore, the main purpose of this study is to examine the impact of high levels of turbulence on performance, comparing these results to smooth flow results in other studies and facilities. Extensive analysis of the velocity profile within the tunnel test section under all flow conditions at the location of the model was made as discussed in Chapter 4. Wind tunnel velocity was measured using MKS Baratron sensor via a Pitot-Static tube in a known location. Manufacturers data gives the accuracy of this instrument as within 0.05% under ambient conditions. The system was checked for leaks, and measured values were calibrated using a fluid manometer prior to testing. Additional details for the IWT are provided in Appendix B. During testing tunnel speed was measured via spare channels on the DAQ card during testing, allowing precise speed to be known for each test.

- Model performance: Manufacturing accuracy of wind tunnel models and the quality of the final product can effect the results, particularly if the model is not manufactured to the required dimensions or is not kept straight and true. Considerable effort was made to produce a model that was dimensionally accurate as described in Chapter 4, with the final model being within +/- 0.1 mm. Model stiffness is also important when working with dynamic measurements as any vibrations or resonance in the model may be seen as a pressure fluctuation on the surface, and significantly influence the unsteady flow fields around the model. The stiffness of the model was investigated and found to not be a serious concern.

- Environmental factors: Whilst the pressure measurement systems used in this work are not as sensitive to their environment as other systems in use, variations in ambient conditions such as temperature and pressure can introduce errors into results and must be monitored. Ambient pressure and temperature were recorded during testing, allowing precise conditions at the time of measurement to be known. Additional ambient conditions such as noise and electrical interference can be introduced into the system, effecting results by appearing as signal spikes

in the waveform. As the IWT is a aeroacoustically treated wind tunnel, noise presented very little concern as sound levels in the test section are low. Electrical interference was assessed by running the tunnel and taking measurements with the pressure ports blocked by tape. In this configuration any signal measured must be induced by electrical interference. Results show that within the frequency range of interest very little noise was evident, with the exception of a 50 Hz spike from main AC power lines. Additional shielding reduced this issue.

- Pressure measurement system: One of the greatest potential source of error in both static and dynamic results comes from the physical pressure measurement system. For static measurements one of the greatest challenges was ensuring the system was free of leaks. A great deal of care was taken testing the system for leaks using a fluid manometer. Particular trouble spots were tubing connections to both the model and the DPMS sensors. With care leaks were eliminated. Errors introduced into dynamic measurements by the frequency response of the tubing system have been discussed in Chapter 4.

- Data acquisition: Errors from data acquisition can be introduced when the signal being sampled falls outside the range of the DAQ card. For example the signal may have a range of +/- 10 V and the card is set to a range of +- 5 V, resulting in "clipping" of the signal when the maximum is exceeded. At the other extreme if the signal power is very low compared to the range of the card, then small changes in the signal may be lost due to the limited resolution of the card or lost in the noise floor of the system.

The effect of the above error sources are varied, and in some cases difficult to quantify accurately without a in depth investigation into each point. The effect of these errors on the conclusions drawn from the results are considered to be small, as the conclusions are based on trends and comparative analysis rather than absolute magnitudes and quantitate accuracy. The experimental measurements used in this work are considered valid in this regard.

5.5 Concluding Remarks

The major conclusions from the pressure measurement work on a finite wing presented in this chapter are as follows:

- In relatively low turbulence, a flat plate airfoil will show signs of early leading edge separation from incidences as low as 6° . Indications of short bubble development on the suction surface near the leading edge are apparent, with subsequent bubble growth, separation and stall occurring quickly. At incidence $> 8°$ the wing appears fully stalled. This behaviour flow is in agreement with prior observations on short bubble formation and bursting by McGregor (1954) and Hu and Yang (2008) (discussed in Chapter 1). This assessment is further supported by the increased levels of unsteadiness present on the upper surface, particularly near the leading edge, and moving rearward in the vicinity of reattachment, with spectral peaks within the 1-5 Hz range.

- Increasing free-stream turbulence levels have a significant effect on the performance of the airfoil section, as well as the behaviour of the separation bubble on the suction surface. The performance of the wing can be assessed by time-averaged C_L compared with α. At higher levels of free-stream turbulence it was observed that the slope of the lift curve does not change; however, a higher $C_{L_{MAX}}$ is reached before stall, effectively delaying the onset of stall. It is notable that there is a significant effect when increasing the freestream turbulence level from 1.5% to 7%; however, when increasing further to 11.5% the magnitude of the change is significantly less indicating that there is a critical point between the first two cases. Analysis of surface pressure measurements indicates that formation of the leading edge separation bubble is delayed or eliminated in the higher turbulence cases.

- Unsteadiness increases significantly on the suction surfaces in the presence of turbulent flow, with energy levels on fluctuating flow several orders of magnitude higher. This indicates that the boundary layer is turbulent in these cases, and that rather than separation bubbles not being present, they may be forming and bursting periodically.

An investigation into the presence and behaviour of separation bubbles and bubble bursting as well as the effect of high levels of free-stream turbulence are the subject of the next chapter, where these phenomena are investigated visually using a number of flow visualisation techniques.

Chapter 6

Visualising Flow Separation in Smooth and Turbulent Conditions

In Chapter 5 quantitative measurements were presented of the surface pressure distribution over a flat plate finite wing for a range of turbulence levels. The results indicated that flow separation and reattachment are present in low turbulence conditions, and that as free-stream turbulence levels are increased the onset and behaviour of flow separation is affected. There is further evidence from dynamic pressure measurements that significant transience is present in the region of flow separation where high levels of free-stream turbulence exist. A useful tool for direct investigation of the behaviour of the flow field over the wing is flow visualisation, enabling direct observation of flow behaviour in regions of interest.

There are a number of visualisation techniques available depending on the particular flow phenomena under investigation and the resources available, these include:

- *Tufting*: A common method of visualising the streamlines near the surface is to place lightweight tufts on the surface, which align in the flow direction. This technique is better suited for larger models, though very fine tufting can be used on smaller models depending on the desired resolution. Tufting provides a good indication of flow direction; however, the presence of the tufts introduce roughness to the surface. In addition, the tufts themselves have inertia and stiffness which restricts their usefulness when visualising dynamic flow behaviour, or flows at fine scales.
- *Oil flow*: Used to visualise surface streak-lines highlighting flows within the boundary layer. An oil film is applied to the surface which is acted on by surface shear stresses. A particulate can be added to the oil, which is left behind on the surface once the oil evaporates.
- *Pressure sensitive paints*: These paints change colour when pressure is applied indicating the

pressure distribution over the surface; however, this technique is most useful when high dynamic pressures are present, such as in high velocity flows or in denser fluids.

- *Particle tracer methods*: Particulate tracers can be introduced into a flow to visualise streamlines. Common examples are smoke and helium bubbles, which can be illuminated and photographed. For complex flows a laser sheet can be used to illuminate just a slice of the flow. Particle image velocimetry (PIV) uses a similar technique, and uses computer algorithms to analyse successive frames to determine flow velocity and direction within the plane.
- *Optical methods*: In some cases flows can be analysed by measuring changes in the refractive index of the fluid with a change in density. This technique is useful for compressible high speed flows in the presence of shock waves.

The primary goal in this work was to investigate regions of flow separation and reattachment and how these alter with changing levels of free-stream turbulence as well as the transient behaviour in these regions. A secondary goal was to investigate the extent of the influence of the free wing tip, and the two dimensionality of the flow at the pressure tap locations described in Chapter 5. This is important as the wing in Chapter 5 was mounted in the wind tunnel with only one end plate, and the other tip free.

Given the above goals, the relatively low flow velocity and available resources, two visualisation techniques were chosen for this work:

- Oil flow carrying an iridescent dye and china clay particulate to visualise time-averaged surface flows,
- Smoke for the visualisation of separation and reattachment regions, including structures with transient properties.

Both these methods were used extensively in this work. Details of the equipment used and techniques employed are presented in this chapter, as well as results showing the separation and reattachment points, how these are affected by free-stream turbulence levels, and significantly the dynamic formation and bursting of separation bubbles on the suction surface.

6.1 Experimental Procedure

Obtaining good results from flow visualisation work requires careful attention to detail in preparation and execution. The following procedure was developed to give the results presented in this chapter.

The same incidence range ($0 > \alpha > 20$ at intervals of 2°) that was used for the pressure measurement work were used for the visualisation work for comparison. Results were obtained for each of the three free-stream turbulence levels as used in previous work, of $I_u = 1.5\%$, $I_u = 7\%$ and

$I_u = 11.5\%$. Tunnel speed was set to 10 m/s for a working Re of 10^5, matching that used for previous measurements. Models were geometrically identical to those used in the pressure measurement work in Chapter 5 and described in detail in Chapter 4.

6.1.1 Surface Flow Visualisation

The surface flow images (presented and discussed later in this chapter) clearly show features such as flow separation and reattachment points, flow direction, and vortex impingement, although not all of these features were present in every case. As surface visualisation highlights the behaviour of the surface shear layer, it is a useful tool in understanding the flow field at the surface and interactions with the boundary layer. Surface flow visualisation was performed using the following procedure.

1. High intensity lighting was installed to provide sufficient light for the photography, while having minimal impact on flow quality. Trial images were shot to confirm adequate lighting for images and to determine camera settings such as shutter speed, aperture and ISO settings.
2. A clay dust was mixed with a light oil (kerosene) with a fluorescent pigment added to aid photography under UV lighting. The mixture was sprayed onto the surface, the wind tunnel was then started and run at 10 m/s until the oil dried. As the carrier evaporated, the powder was left on the surface tracing out streak lines.
3. A Canon 400D SLR digital camera with a EF 50 mm f/1.8 prime lens was used for the still photography work. The resulting patterns were photographed under UV lights to illuminate the pigment in the tracer. The exact mixture of the oil and powder was determined through a process of trial and error until the desired result in terms of image quality was obtained.

6.1.2 Smoke Visualisation

Smoke visualisation was used to visualise the features present in the flow away from the surface. It also has the advantage of enabling the visualisation of rapidly changing flow features such as the formation and bursting of regions of separated flow. The process and methodology used for smoke visualisation in this work is summarised below.

1. Smoke was injected into a 5 m/s airstream using a smoke wand at a number of locations around and upstream of the model at the same spanwise location as the pressure taps described in Chapter 5.
2. Images were captured from a number from different perspectives around the model using Canon HV20 high definition (HD) video camera set to capture progressive frames at 25 fps at 1080 x 1900 resolution (PAL standard format 1080p). The use of 1080p HD video allowed the imaging of dynamic flow structures around the model at high resolution. Strong lighting allowed a

variation of shutter speed from 1/25,000 of a second to as slow as 1/25 of a second giving a range of averaging effects in the image. Very fast shutter speeds allowed visualisation of details in the flow, while slower speeds allowed blurring of the smoke highlighting larger flow features and mean directions.

3. Wind speeds were reduced to 5 m/s for the majority of the tests to reduce smoke dispersion, and to enable the 25 fps frame rate of the video to capture progressive frames containing the same flow features within successive frames. At a frame rate of 25 fps, and a tunnel speed of 5 m/s, the distance the flow traverses between frames is 200 mm, which is within the field of view of the camera for at least two successive frames although still larger than the chord of the wing. A higher frame rate would be desirable as a better temporal and spatial resolution could be achieved. This would have meant that the tunnel could be run at a higher speed to match the Reynolds number of other tests; however, the cost of the equipment required would be prohibitive and outside the available budget for this research work.

6.2 Visualisation of "Mean" Flow Phenomena

Mean flow phenomena can be thought of as flow structures that persist and are largely unchanging over time; features that do not exhibit a high degree of transience. Examples of such structures would be strong tip vortices, flow separation points and boundary layer transition points. This first set of visualisation work was aimed at investigating the prevalence and placement of these structures on the wing, and how there features were affected by the introduction of high levels of turbulence such as that found outdoors in the ABL.

6.2.1 Low Turbulence Conditions (1.5%)

There is a large prior body of work (discussed in Chapter 1) regarding the investigation of flows around thin wings in smooth flow. While the lowest level of turbulence achievable in the IWT facility is $I_u = 1.5\%$ it is considered sufficiently low that it provides a useful comparison point for the high turbulence work which is the focus here.

Shown in Figure 6.1 is an image of the top surface of the wing at $\alpha = 6°$, taken using surface oil flow after the oil has evaporated, illuminated using a UV light source. In this image, a number of distinct features are visible. Flow separation points are characterised by dark lines which appear near the leading edge. The region appears dark in the images as the oil has not fully evaporated due to the very low local velocity at the surface. (It should be noted that these features have been corroborated with the smoke images in Figure 6.3). Significantly, the separation line is not located at the leading edge which can be the case for flat plates at low Re with rounded (non-sharp) leading edge geometry as discussed in Chapter 1, rather it is located at approximately 5% chord. Further downstream, at approximately 30% chord there is evidence of flow reattachment over a broad area,

with streaklines flowing towards the leading edge forward of this point, indicating flow reversal and the presence of a separation bubble. Downstream of reattachment, the streaklines flow towards the trailing edge indicating the flow is reattached to the surface. Additional features are visible at the wing tip (top of image) where a vortex impingement is visible. The tip vortex appears to reduce the size of the separation bubble towards the tip and promote flow attachment in this region.

Surface visualisation is shown in Figure 6.2 for a series of images cropped to focus on the mid span location, corresponding to the location of the pressure taps in Chapter 5. In each frame α is varied from 0° to 10° in 2° increments. From $\alpha > 4^\circ$ a separation point is visible downstream of the leading edge (right of image). Images for $\alpha > 10^\circ$ were obtained; however, as they show significant flow separation, which shows up poorly on the surface as streaklines, they are not shown here.

It was observed that in Figure 6.2 as α is increased, the separation point moves rearward slightly, and appears to become more defined (darker). A well defined reattachment becomes visible from $\alpha = 4^\circ$, becoming broader and also moves rearward with increasing α. At $\alpha = 6^\circ$ and $\alpha = 8^\circ$ there appears to be a region of reversed flow moving from the reattachment zone towards the separation point. At $\alpha = 10^\circ$ the separation point has moved to the trailing edge, indicating complete flow separation, proceeding stall.

Whilse the expanse of separation might appear large from the surface flow in Figure 6.2, this can be deceptive as demonstrated by investigating the thickness of the separation using smoke visualisation (shown in Figure 6.3) which shows a smoke stream introduced just upstream of the leading edge as the incidence is increased from $\alpha = 0^\circ$ to $\alpha = 20^\circ$. Close inspection of the image at $\alpha = 6^\circ$ shows a small region just aft of the leading edge where the smoke stream is lifted from the surface, then reattaches downstream, corresponding to the same features in the surface flow in Figure 6.2. As α is further increased this detached region grows in size and extends further downstream. At high incidence there is evidence in the smoke stream of circulation and reversed flow near the surface. At $\alpha = 16^\circ$ flow reversal is observable within the separated region, a phenomenon which likely exists at other α as well, and is clearly illustrated in this image. At $\alpha < 14^\circ$ the flow no longer reattaches to the surface downstream of separation, indicating full separation. At incidence levels above $\alpha = 10^\circ$ there is visible unsteadiness in the flow, which is illustrated and discussed later.

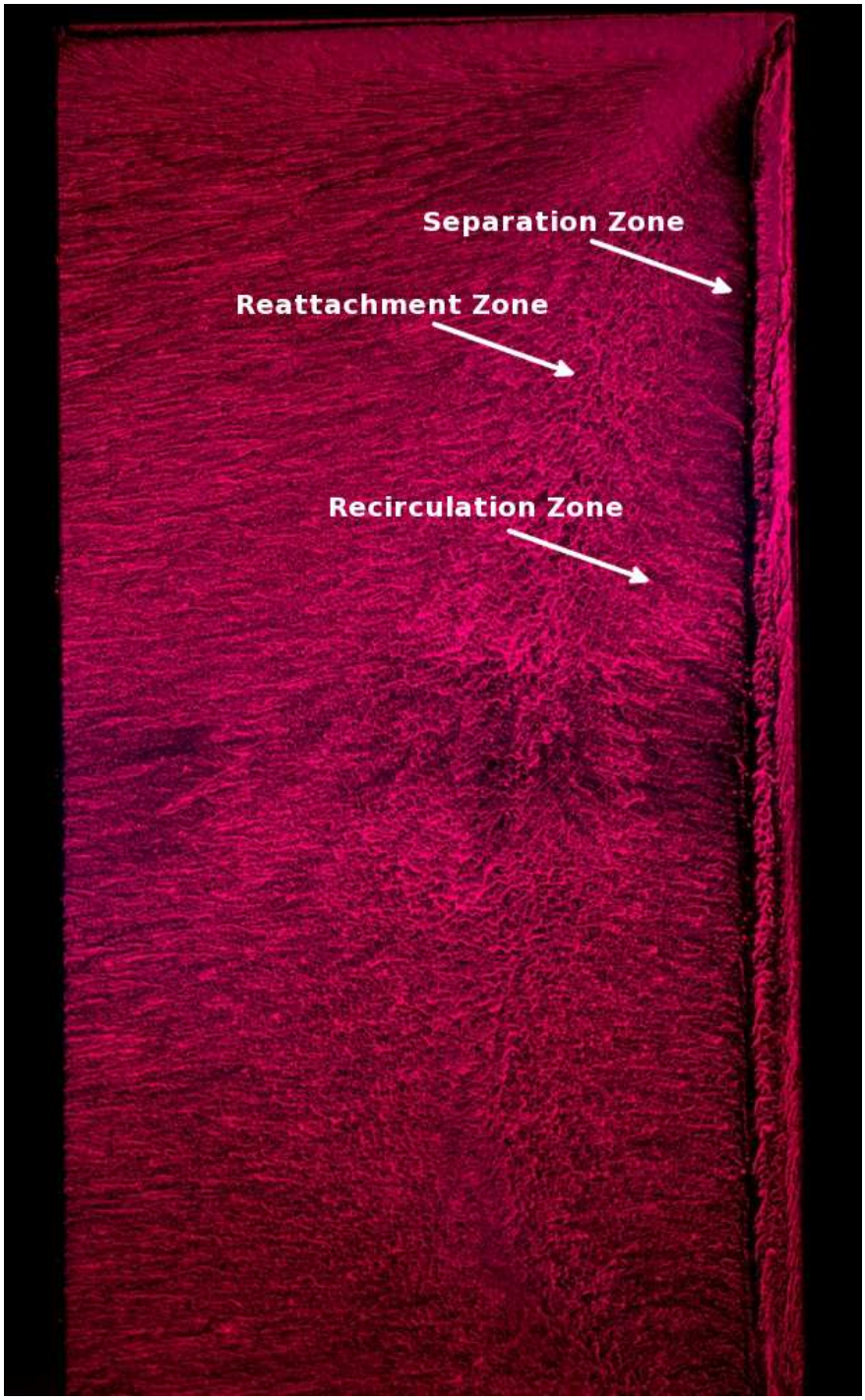

Figure 6.1: Oil flow visualisation of entire wing at $\alpha = 6°$ with a low free-stream turbulence condition of $I_u = 1.5\%$ (the leading edge is to the right of the image, and the trailing edge to the left)

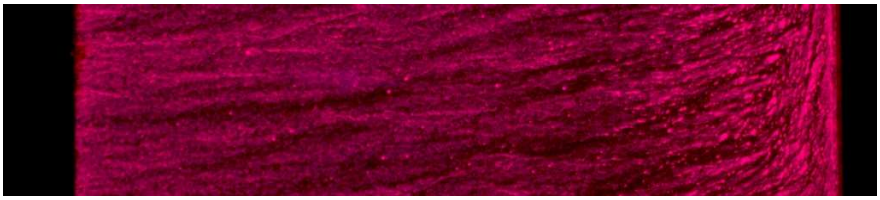

(a) $\alpha = 0°$

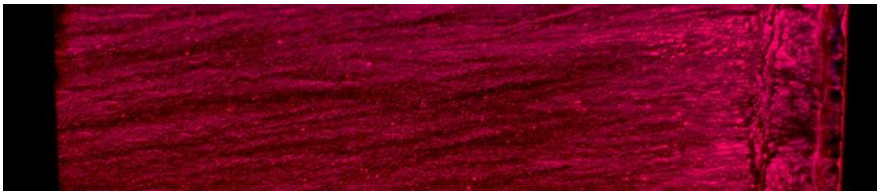

(b) $\alpha = 2°$

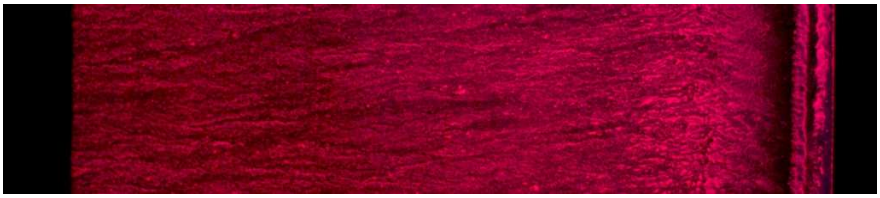

(c) $\alpha = 4°$

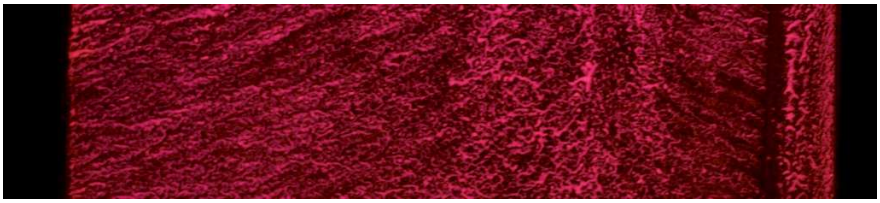

(d) $\alpha = 6°$

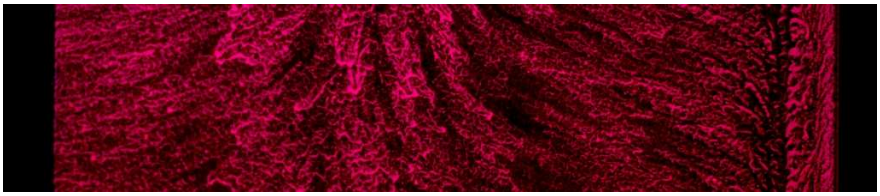

(e) $\alpha = 8°$

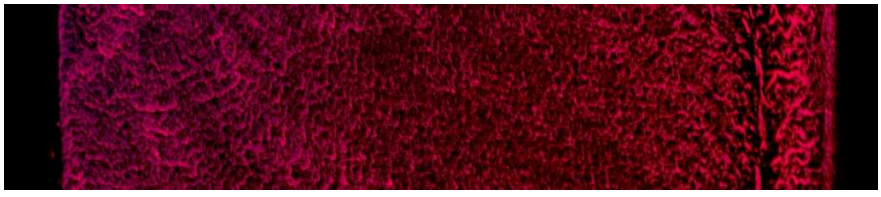

(f) $\alpha = 10°$

Figure 6.2: Surface visualisation using oil flow at $I_u = 1.5\%$ at $0 < \alpha < 10°$, images show wing section at the span-wise location of the pressure measurements in Chapter 5 (approximately mid semi-span)

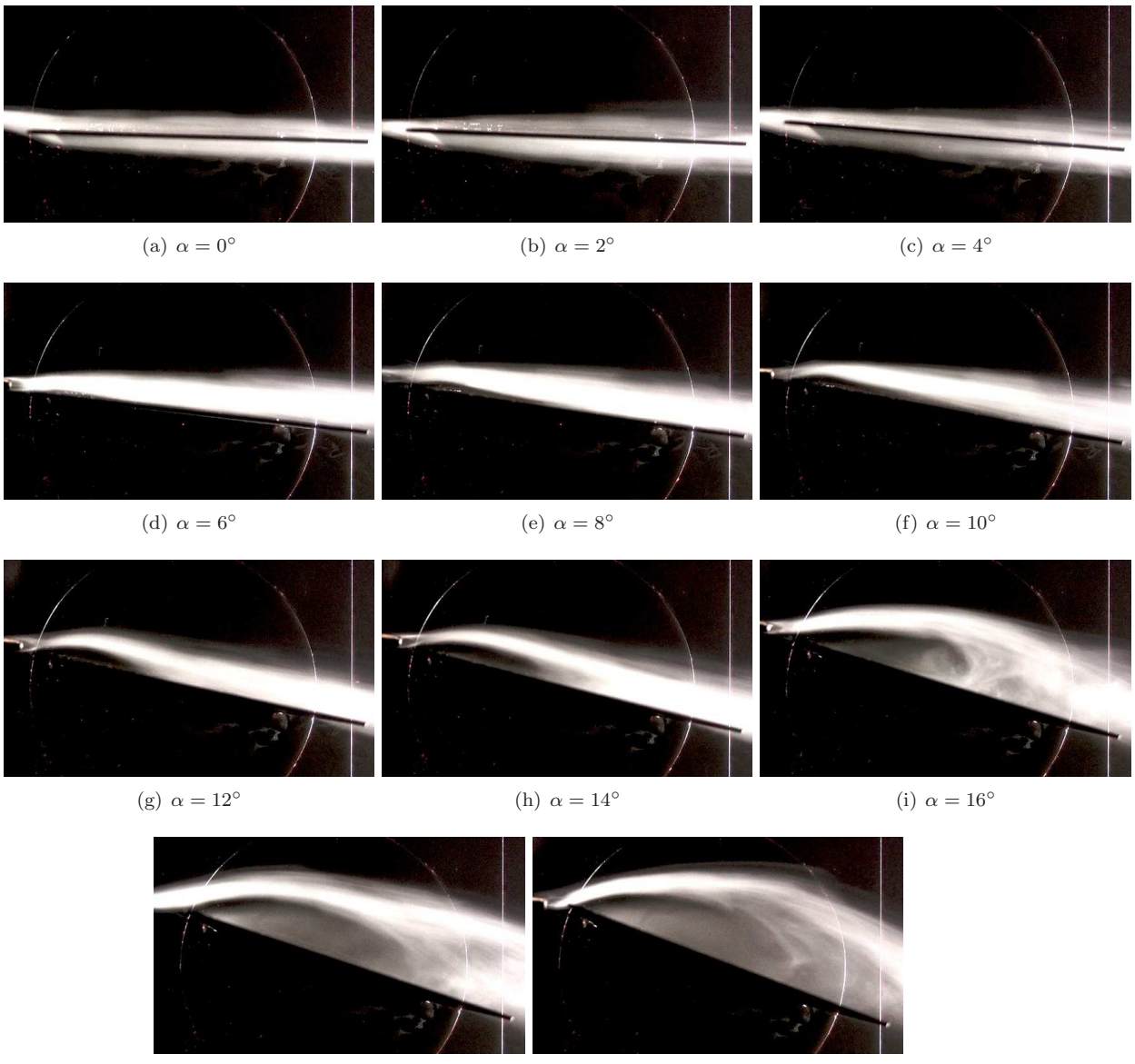

(a) $\alpha = 0°$ (b) $\alpha = 2°$ (c) $\alpha = 4°$

(d) $\alpha = 6°$ (e) $\alpha = 8°$ (f) $\alpha = 10°$

(g) $\alpha = 12°$ (h) $\alpha = 14°$ (i) $\alpha = 16°$

(j) $\alpha = 18°$ (k) $\alpha = 20°$

Figure 6.3: Smoke visualisation showing development of separation region and reattachment for the low turbulence case (I_u=1.5%, $\overline{U}$=5m/s)

6.2.2 Flow Under Increased Levels of Free-Stream Turbulence

Analysis of pressure data discussed in Chapter 5 indicated that as free-stream turbulence is increased, the onset of flow separation with increasing incidence is delayed, and the size of the separated region is reduced. Visual verification confirmed both these results.

Presented in Figures 6.4 and 6.5 are surface flow images for free stream turbulence levels of $I_u = 7\%$ and $I_u = 11.5\%$ respectively. Compared with the low turbulence case presented earlier in Figure 6.2, the appearance of a reattachment is delayed. At a free-stream turbulence level of $I_u = 7\%$ a reattachment point appears to occur just rear of the leading edge at $\alpha = 4^\circ$ just as it does in the low turbulence case; however, rearward movement with further increasing incidence is not as great, only reaching mid chord by $\alpha = 10^\circ$. In the high turbulence case, $I_u = 11.5\%$ this is further delayed, with a well defined attachment point not appearing until an α between 6° and 8° , and only moving rearward to approximately 40% chord at $\alpha = 10^\circ$.

Apparent separation lines still exist near the leading edge in the higher turbulence cases, shown in Figures 6.4 and 6.5. The only visual effect of increasing free-stream turbulence levels is to cause the appearance of these separation lines at lower angles, including $\alpha = 0^\circ$.

Presented in Figures 6.6 and 6.7 are smoke flow images at free-stream turbulence levels of $I_u = 7\%$ and $I_u = 11.5\%$, respectively at incidence $0^\circ < \alpha < 20^\circ$. Each frame has a exposure time of 1/50 of a second, with the smoke source placed just upstream of the leading edge. Compared to the low turbulence case shown in Figure 6.3, the higher free-stream turbulence levels appear to show a reduction in both the size and extent of flow separation. Figure 6.6 shows a small separation region at $\alpha = 10^\circ$, which grows in size as α is increased. Reattachment occurs downstream and does not exhibit the large scale separation without reattachment shows in Figure 6.3 at high α. Figure 6.7 shows that at the highest level of turbulence generated in the tunnel, the appearance of the bubble is further delayed until $\alpha = 12^\circ$.

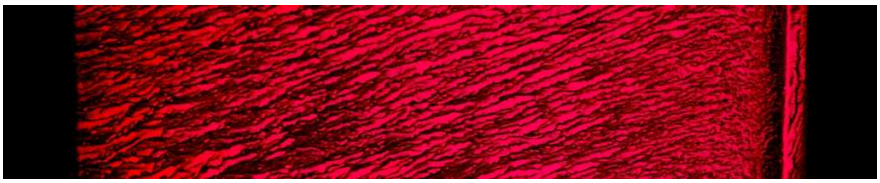

(a) $\alpha = 0°$

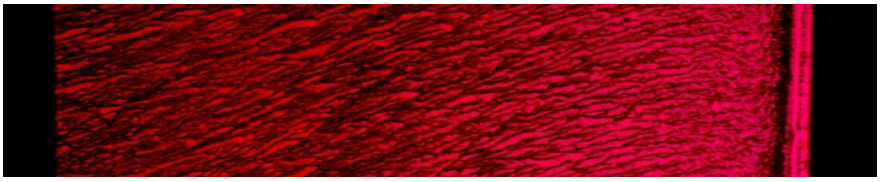

(b) $\alpha = 2°$

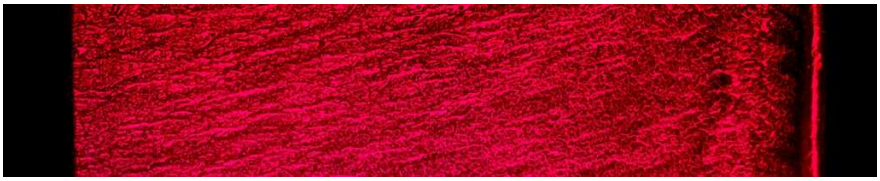

(c) $\alpha = 4°$

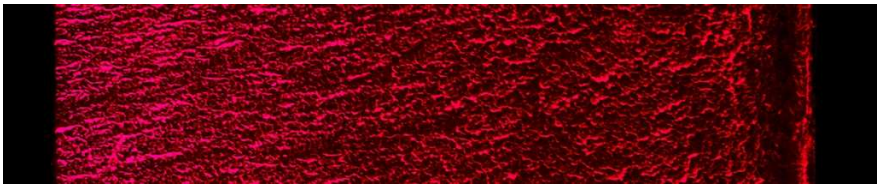

(d) $\alpha = 6°$

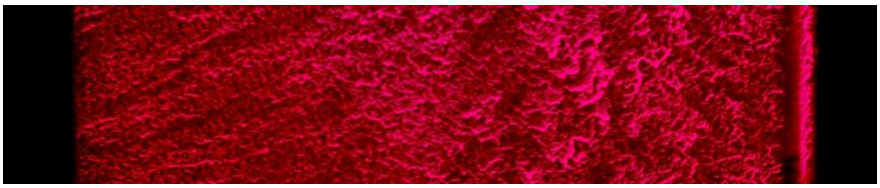

(e) $\alpha = 8°$

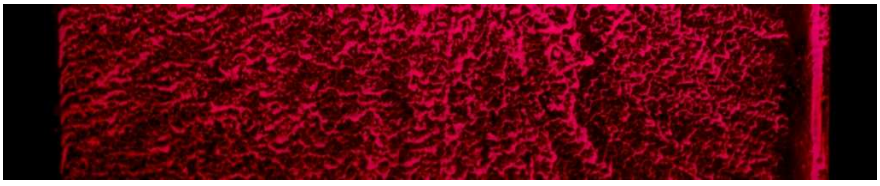

(f) $\alpha = 10°$

Figure 6.4: Surface visualisation using oil flow at $I_u = 7\%$ at $0 < \alpha < 10°$ (images show wing section at the span-wise location of the pressure measurements in Chapter 5, approximately mid semi-span)

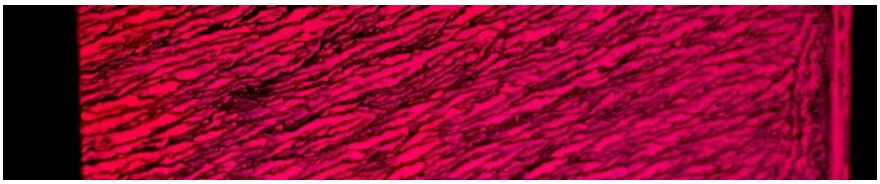

(a) $\alpha = 0°$

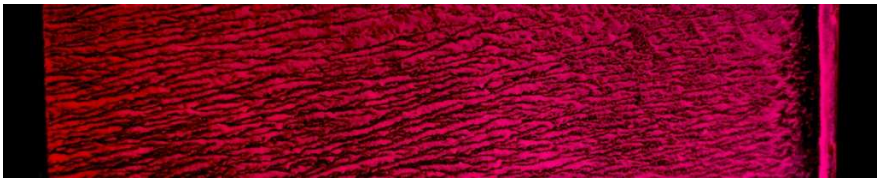

(b) $\alpha = 2°$

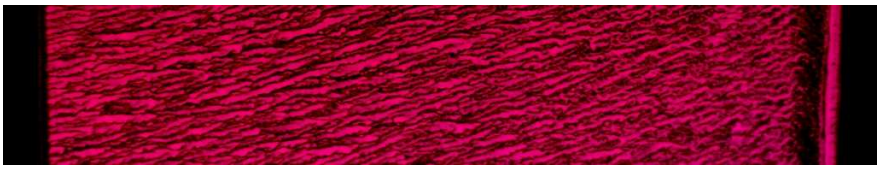

(c) $\alpha = 4°$

(d) $\alpha = 6°$

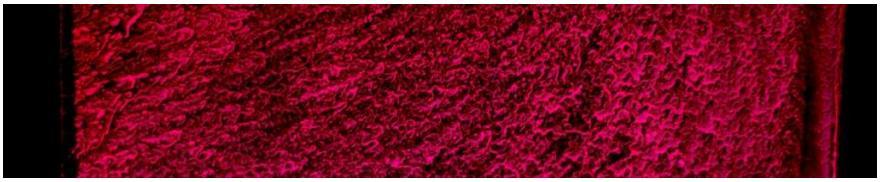

(e) $\alpha = 8°$

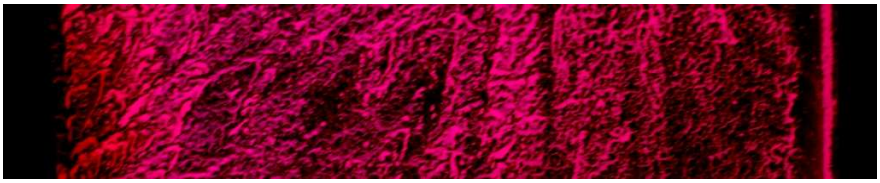

(f) $\alpha = 10°$

Figure 6.5: Surface visualisation using oil flow at $I_u = 11.5\%$ at $0 < \alpha < 10°$ (images show wing section at the span-wise location of the pressure measurements in Chapter 5, approximately mid semi-span)

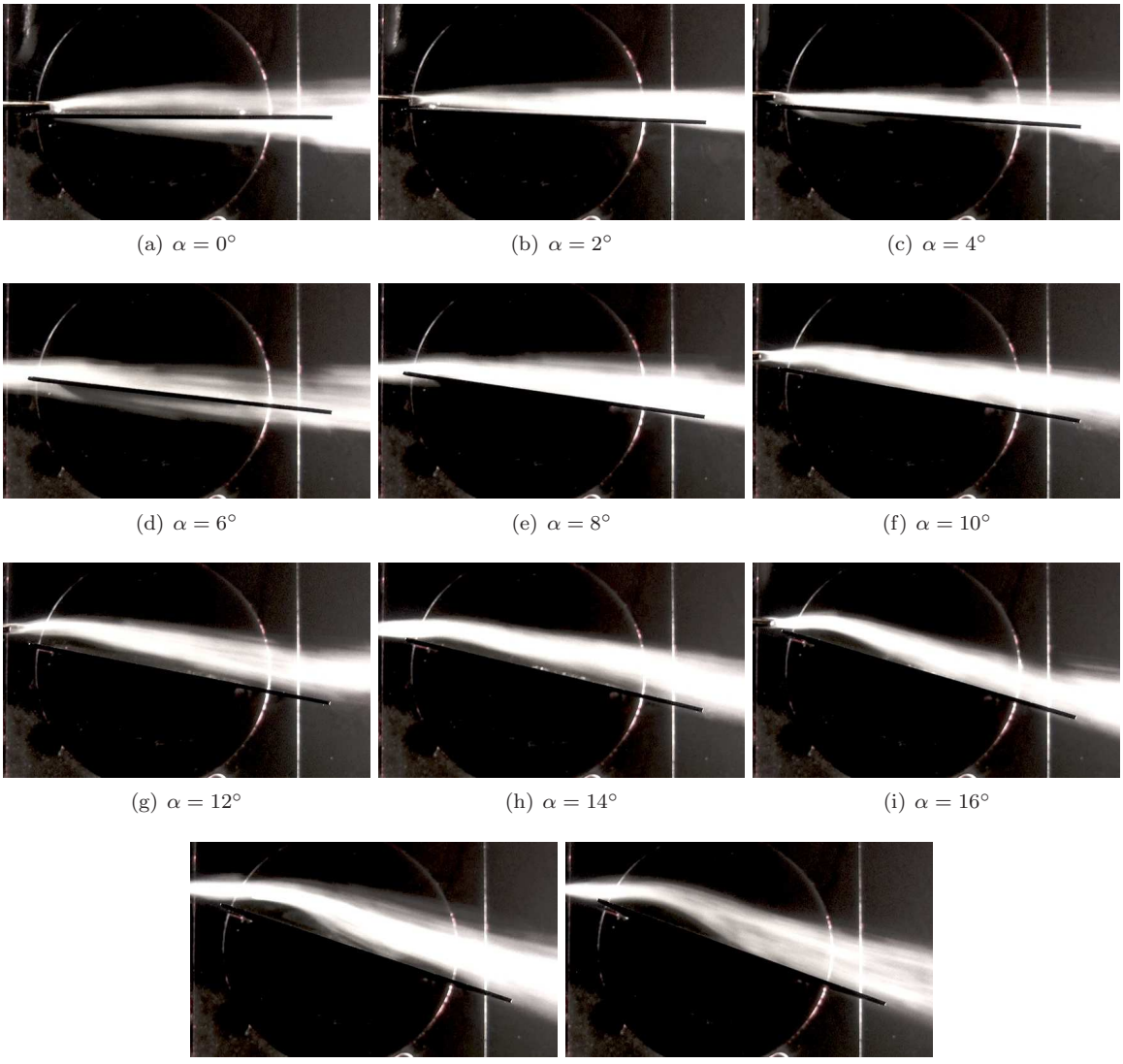

(a) $\alpha = 0°$ (b) $\alpha = 2°$ (c) $\alpha = 4°$

(d) $\alpha = 6°$ (e) $\alpha = 8°$ (f) $\alpha = 10°$

(g) $\alpha = 12°$ (h) $\alpha = 14°$ (i) $\alpha = 16°$

(j) $\alpha = 18°$ (k) $\alpha = 20°$

Figure 6.6: Smoke visualisation showing development of separation region and reattachment for the medium turbulence (I_u=7%, $\overline{U}$=5 m/s)

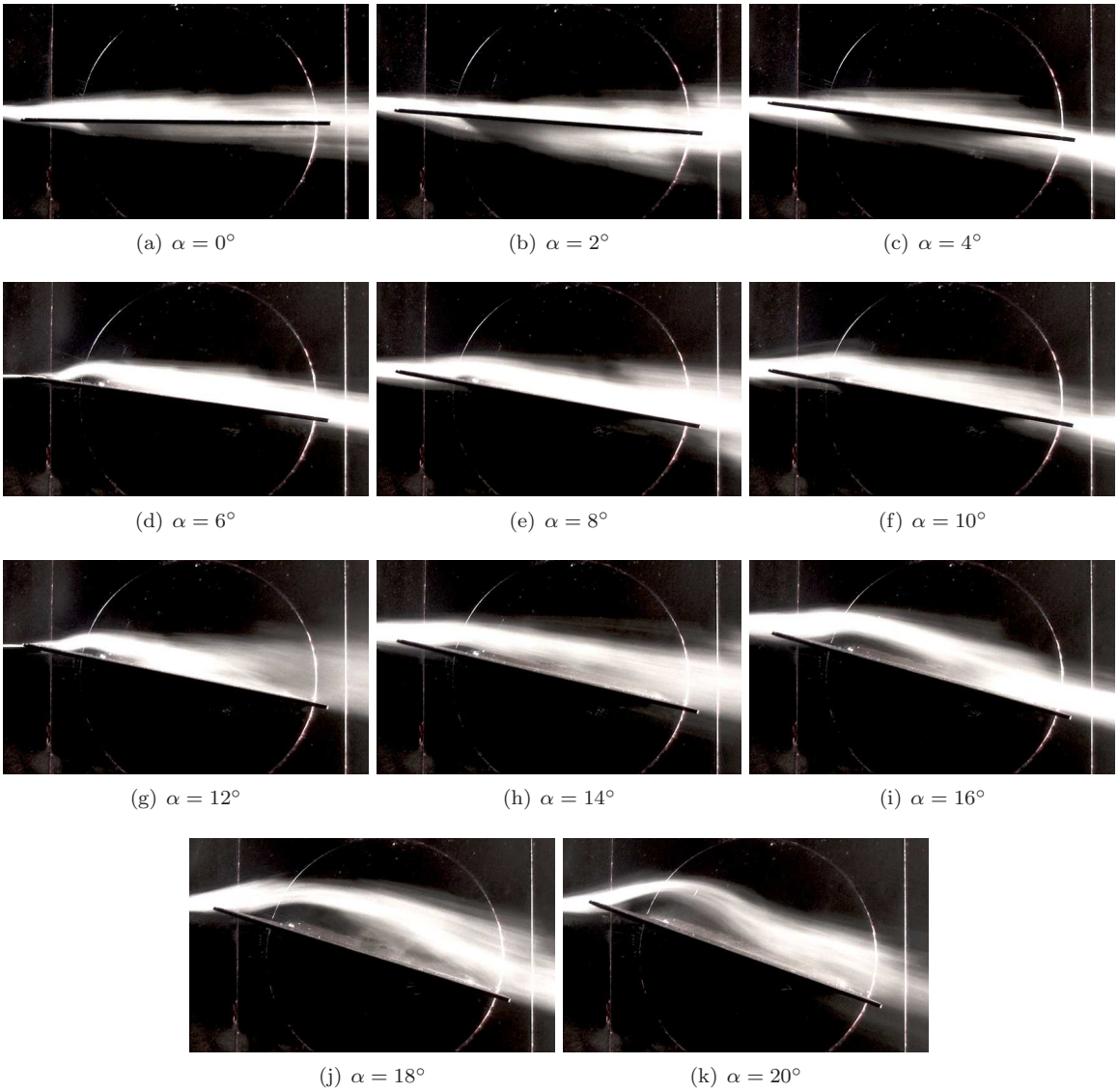

(a) $\alpha = 0°$ (b) $\alpha = 2°$ (c) $\alpha = 4°$

(d) $\alpha = 6°$ (e) $\alpha = 8°$ (f) $\alpha = 10°$

(g) $\alpha = 12°$ (h) $\alpha = 14°$ (i) $\alpha = 16°$

(j) $\alpha = 18°$ (k) $\alpha = 20°$

Figure 6.7: Smoke visualisation showing development of separation region and reattachment for the high turbulence (I_u=11.5%, $\overline{U}$=5 m/s)

6.3 Visualisation of Dynamic Flow Phenomena at High Free-Stream Turbulence

Dynamic flow was visualised using HD video shot at 25 progressive frames per second. Analysis of the resulting image stream shows considerable transience in the flow field, particularly at higher free-stream turbulence levels.

In the high turbulence cases (I_u=11.5%) there is significant transient behaviour observed in the image sequences. This transience is illustrated in Figure 6.8 and 6.9 which show a sequence of 9 frames covering approximately 0.4 seconds at $\alpha = 0°$ and $\alpha = 10°$ at the highest turbulence level. At $\alpha = 0°$ the sequence in Figure 6.8 shows a typical smoke pattern as an "eddy" moves past the wing. In this sequence each frame is separated by 1/25 of a second, giving approximately 0.4 seconds for the whole sequence. The α range at the leading edge as it moves past is clearly visible and in the order of +/- 20° . At $\alpha = 10°$ (Figure 6.9) a sequence over the same time frame shows how the transience in α effects the formation of a separation bubble in the third image. By the forth and fifth image the bubble has expanded and appears to "burst", before the flow again reattaches without any bubble present by the end of the sequence. Whilst only covering once "cycle", the sequence repeats itself at a resulting frequency of 3 Hz.

When observed looking down at the top surface of the wing, a similar sequence of bubble formation and bursting is shown in Figure 6.10. From this viewpoint it is seen that the bubble bursting extends out along the span, and causes turbulence separation over a significant portion of the wings surface, regardless of where the initial separation point originated. This pattern is typical of many observed, occurring at regular intervals, and highlighting how the bubble formation and bursting cycle occurs over the entire wing.

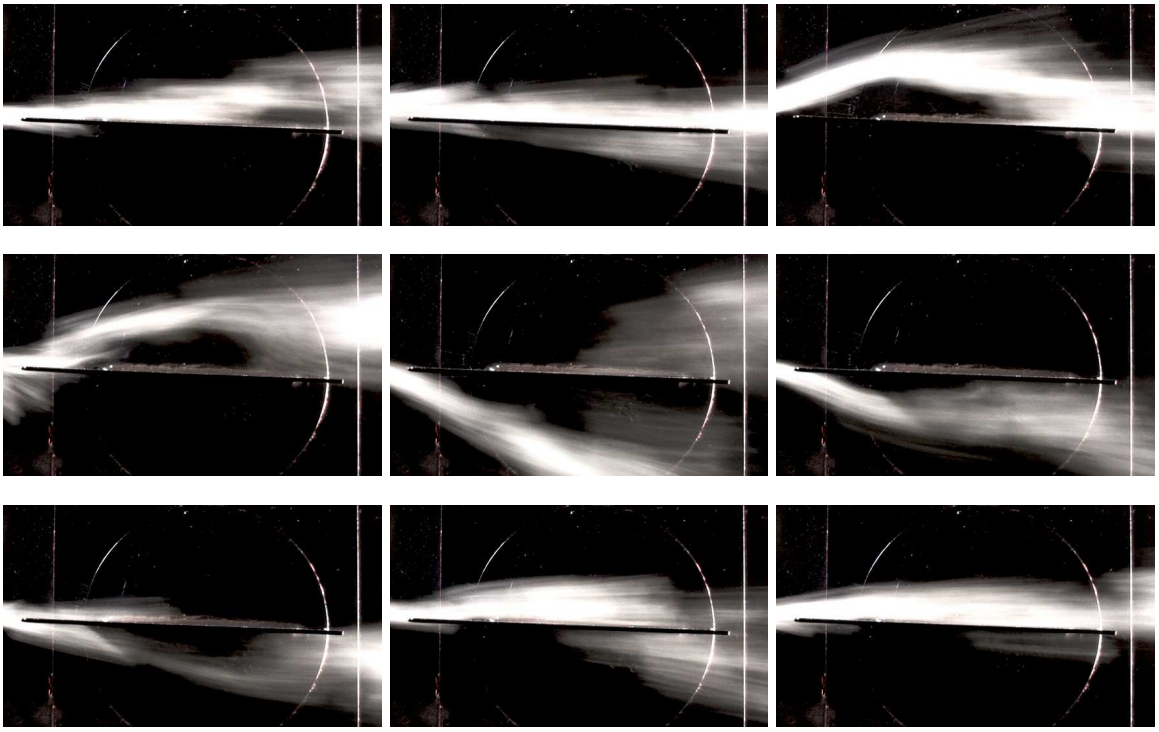

Figure 6.8: This image sequence shows the large local variations in pitch angle as a turbulent eddy moves past the wing (I_u=11.5%, $\overline{U}$=5 m/s and α=0°)

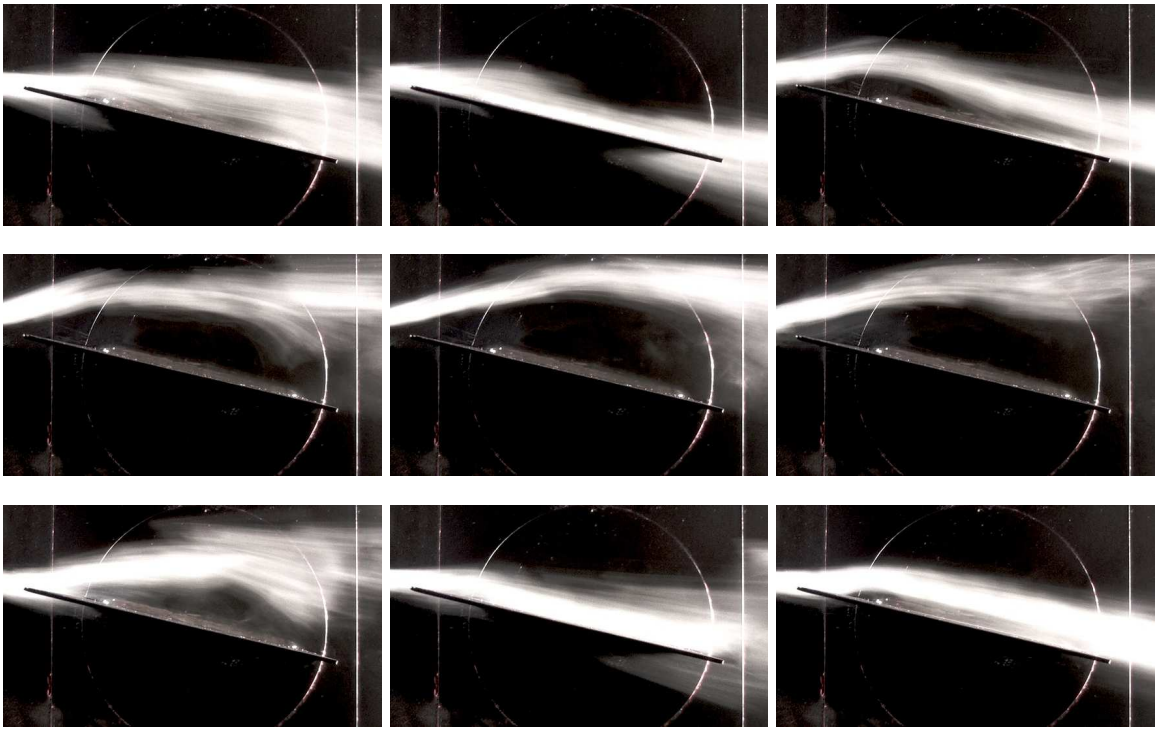

Figure 6.9: In this sequence the formation and bursting of a separation bubble is visible as a turbulent eddy moves past the wing, resulting in changing local pitch angles (I_u=11.5%, $\overline{U}$=5 m/s and α=10°)

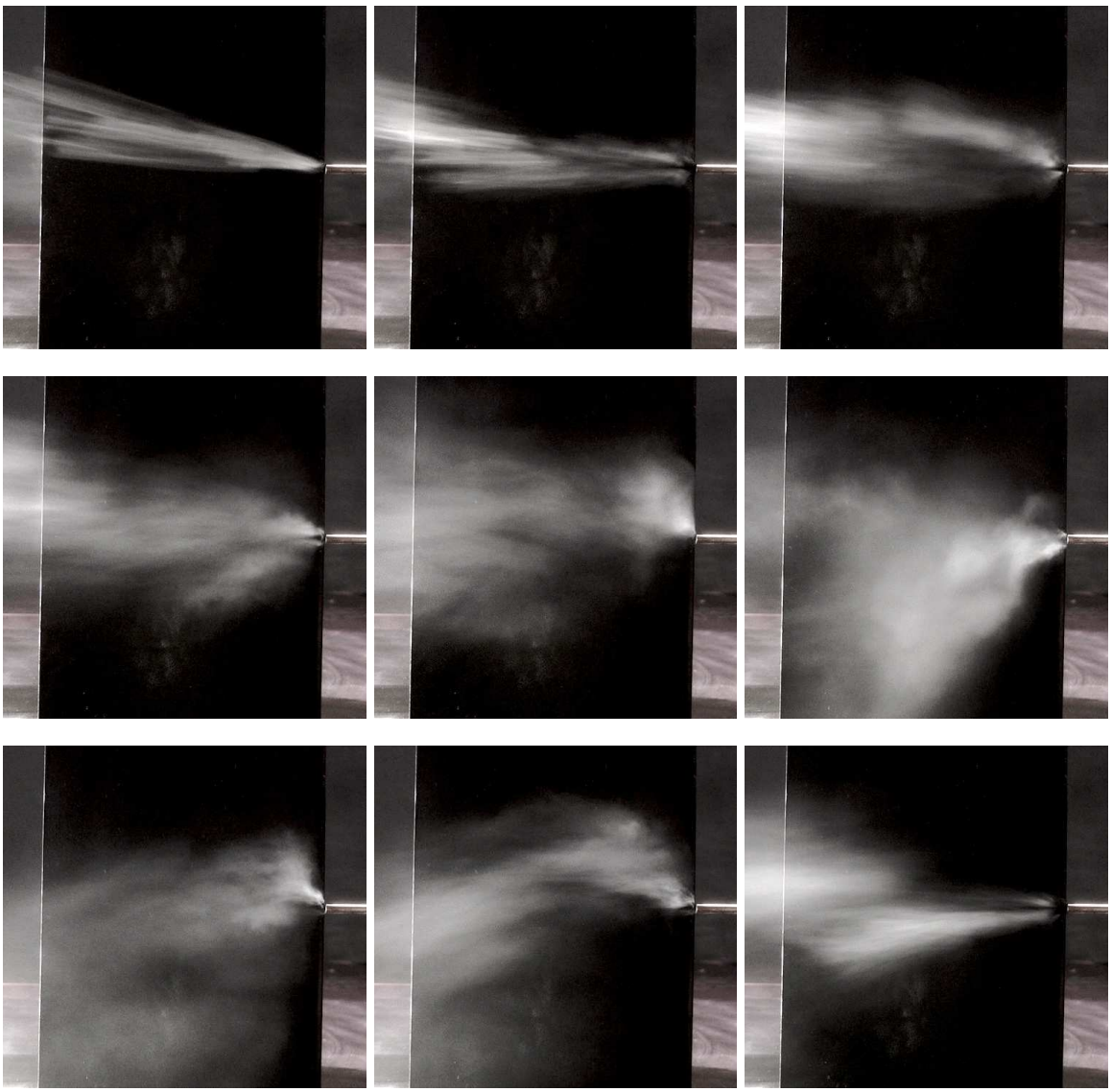

Figure 6.10: This sequence shows the effect of a eddy moving past the wing and the change in local pitch angle causing a bubble to form and shed from the surface (I_u=11.5%, $\overline{U}$=5 m/s and α=10°)

6.4 Investigation of the Influence of the "Free" Wing Tip on the Finite Wing

The influence of the free wing tip on flow features of a wing of finite span is an important part of this investigation. The influence the tip vortex has on the flow field around the wing, particularly at the location of the pressure measurements in Chapter 5, is one of the key questions that can be addressed through surface visualisation. Of interest is the extent, if any, of the span-wise flow component present at the span-wise station where the pressure measurements were made, and how this influences the formation and behaviour of the separation bubble on the surface.

The surface visualisation images for the whole wing at $\alpha = 6^\circ$ are shown in Figure 6.11. In the low turbulence case (1.5%), a clear vortex impingement line is visible just inboard of the wing tip indicating the presence of a tip vortex (as expected). The reattachment line which exists at 50% chord mid-span is drawn towards the leading edge in the outboard portion of the wing, meeting the leading edge at the wing tip. As the turbulence level is increased the reattachment line moves further towards the leading edge as explained above; however, the vortex impingement line remains unchanged. In the high turbulence case there is no visible reattachment line. In all three images, the dark separation line is visible just downwind stream of the leading edge, and appears constant across the span.

At the pressure tap location, which is at the mid span point (half way between tip and root) the flow appears to be well developed in all three cases, with no direct influence of the tip vortex in terms of separation and reattachment locations. It should be noted, that to make an accurate estimation of the influence of the finite span wing, a direct comparison should be made with a infinite case, or a wing with endplates. Such a comparison is complicated in turbulent flow as the presence of the endplates affects the turbulence in the flow by effectively constraining the large eddies present. Such a comparison was not made in this work, although could be the subject of a future investigation.

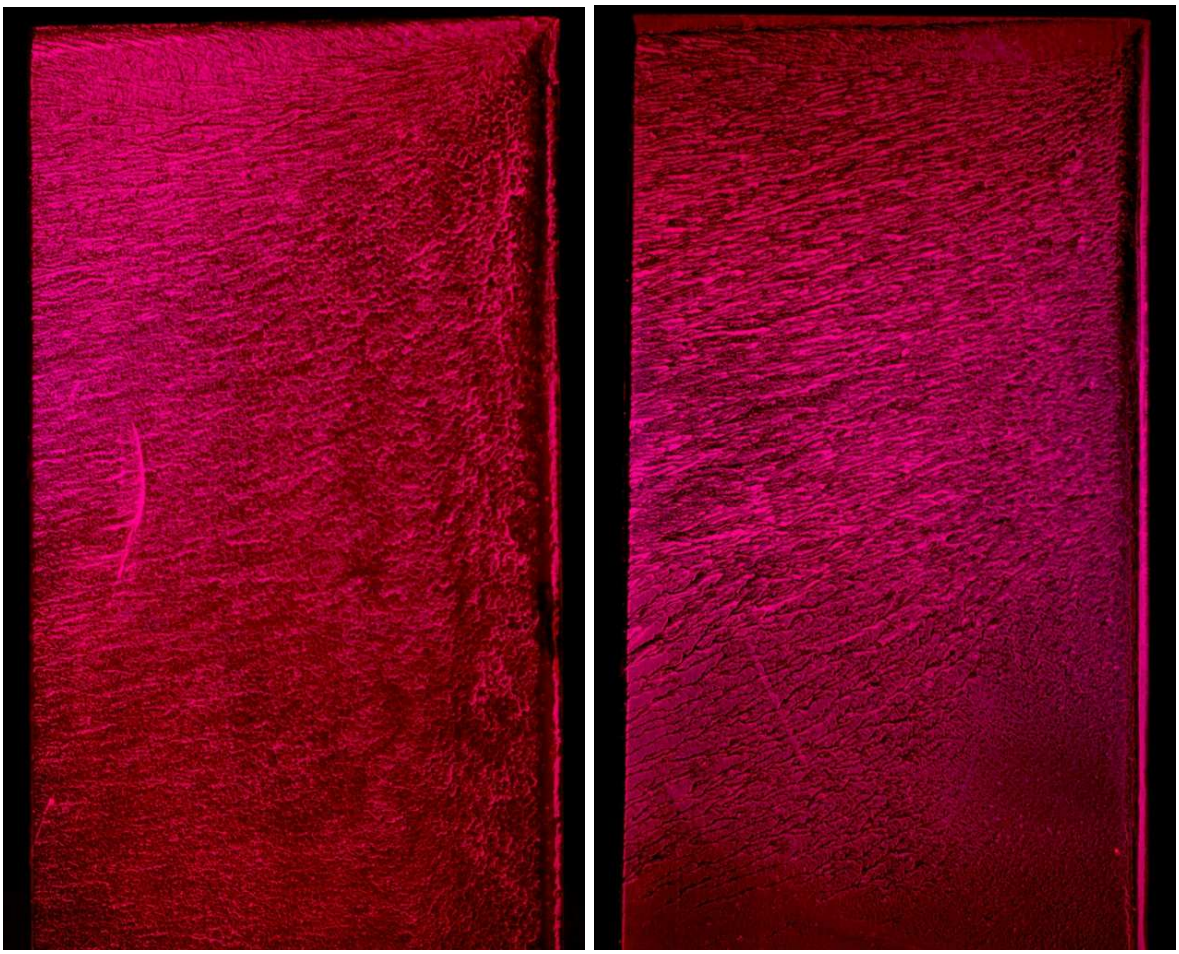

(a) $I_u = 7\%$ (b) $I_u = 11.5\%$

Figure 6.11: Oil flow visualisation of entire wing at $\alpha = 6°$ and turbulence levels of 7% and 11.5%

6.5 Implications of Variability in Oil / Powder Mixture for Surface Flow Visualisation

It was found that the quality of the resulting pattern was sensitive to the quantity of oil / powder mixture applied to the surface. Too little and the mixture would dry quickly and evenly leaving only a smooth residue layer with no streaking. Too much and it would not dry quickly enough and flow down the span wing. The wing was mounted vertically as per the pressure measurements to maintain similarity to these experiments in terms of tunnel location; however, this resulted in some spanwise movement of the fluid due to gravity drawing the fluid along the wing rather than a flow phenomenon. This is observable in Figure 6.2(b) for example. It was determined this effect was not due to the fluid flow, by comparison with smoke flow and also by a trial run where the wing was mounted horizontal in another part of the tunnel (secured to the tunnel wall for example).

6.6 Smoke Visualisation Limitations

Smoke visualisation is useful tool for analysing the structures in the flow away from the body, and for investigating how the flow changes over time. However, several important limitations in the method as used in this work:

- The smoke was injected into the airstream upstream of the body by a smoke wand, which has a heated tip (6 mm in diameter) to burn a light oil to produce the smoke. The presence of this wand directly upstream of the region being investigated by the smoke has a direct influence on the flow being observed, by the interaction of the wake from the wand with the boundary layer on the wing. The full influence is difficult to quantify as it would require measurement of a unaffected boundary layer, which is difficult to achieve as any measurement introduces its own disturbances. It is likely that the presence of the wake alters the behaviour of the transition and separation points as it would disturb the (if any) laminar flow regions present on the surface. At very high shutter speeds, evidence of vortex shedding in the wake of the smoke wand was observed. As the smoke flow here is used primarily to investigate larger events in the flow, it is still considered valid and useful.
- As the camera used for the photography was a consumer camcorder, the frame rate was limited by the standard high definition format (in PAL) of 25 frames per second. A much higher frame rate is desirable to capture more rapid fluctuations in the flow. A higher frame rate would also allow better tracking of a single disturbance as the flow moves less distance between frames.
- Tunnel speed was 5 m/s for two reasons; firstly due to the relatively low frame rate of the camera, to reduce the flow distance between successive frames and secondly to maintain sufficient smoke density, which dissipates at higher speed. The lower tunnel velocity has disadvantages when

comparing the results to those taken at 10 m/s due to potential Re dissimilarity; however, this effect is shown to be minimal from the work on changing Re in Chapter 5.3.6.

6.7 Conclusions

Flow visualisation was successfully conducted using smoke and surface techniques with the following conclusions:

- Surface flow indicated that in low turbulence flow, separation and reattachment points are present at incidence above 4° . At this turbulence level as incidence in increased the reattachment point moves rearward reaching the trailing edge by $\alpha = 10°$
- At higher levels of free-stream turbulence, the onset of significant flow separation illustrated by the appearance of a separation line is delayed, and the downstream progression of the separation line with increasing incidence is reduced.
- Smoke visualisation confirmed the presence of a separation bubble in the low turbulence case that increases in size with increasing incidence. As the free-stream turbulence level is increased, the size of the bubble is significantly reduced.
- Analysis of 25 fps video sequence at a high turbulence level visualised the formation and bursting of the separation bubble on the suction surface, occurring at a rate of approximately 3 Hz.

Chapter 7

Conclusions

This thesis has sought to build on the understanding of the effects of high levels of free-stream turbulence on low Reynolds number flight via a series of wind tunnel experiments, involving both measurement and observation. In the first Chapter the topic of low Reynolds number flight was explored and from a study of the state of the art, two broad areas of work were identified. These were:

1. The flight environment of small aircraft within the ABL is not well documented nor understood at relevant scales. The current body of knowledge contains significant work characterising the ABL on a mesoscale and at scales relevant to wind engineering and road vehicles. Within this, further knowledge is required to better elucidate sensitivity to terrain effects.

2. The effects of turbulence on aerodynamic performance is not well understood, particularly with respect to the behaviour of the boundary layer and laminar separation bubble existing at low Reynolds number flow regimes. It is likely that turbulent eddies approaching MAVs in flight induce significant variations in incidence on lifting surfaces. The frequency and magnitude of these disturbances depend on vehicle mass, flight speed, and the size and structure of the turbulence in the airflow. The effect of these disturbances on the boundary layer, and on the behaviour of flow separation present at low Re is not well documented or understood.

Further refinement of these areas led to the following specific research questions that this work would focus on:

1. Measure turbulence levels in the atmosphere near the ground in a range of different terrains and wind conditions at scales relevant to MAV flight.

2. Conduct a series of wind tunnel experiments to reproduce the most relevant scales and intensities of turbulence for the purpose of investigating the effects of turbulence on MAVs.

3. Investigate, using established methods, the effect of turbulence levels on a simple MAV geometry, focusing particularly on the aerodynamic performance of the wing and the behaviour and influence of the laminar separation bubble on the suction surface.

Through a program of outdoor measurements and wind tunnel experiments, useful results were obtained on both the above questions. Discussion and conclusions are presented at the end of each chapter and the most significant points are listed below.

7.1 Major Conclusions

The initial phase of this work was to investigate turbulence levels in the ABL roughness zone through a series of outdoor measurements aimed at documenting free-stream turbulence levels present in the atmospheric wind. This work found that:

1. At the small scales measurable in this work, and for the larger scales measured by Flay (1978) described in Chapter 1, the $-\frac{5}{3}$ slope describing the spectral energy cascade predicted by Kolmogorov (1961) can be applied with confidence even close to the ground in the roughness zone, where the flow field is largely dominated by the wakes of upstream objects.

2. Changes in mean wind speed have no measurable effect on the magnitude or slope of the PSD when plotted as a function of reduced frequency (frequency divided by wind speed). The terrain has a negligible effect on the slope, but does affect the level of turbulence intensity in the airstream. For example, for a given wind speed, the freestream turbulence level will be higher in a smooth terrain environment than in a rough one.

3. The variation in measured pitch angle between two laterally separated points in space (along a wing leading edge for example) increases with lateral separation and is a function of turbulence intensity and air speed. The effect of increased flight speed is to reduce the apparent variation in pitch angle since the mean horizontal component is increased whilst the magnitude of the fluctuating vertical component remains unchanged. Conversely, the effect of increasing wind speed is to increase the pitch angle fluctuation since the mean horizontal component is now fixed, and the vertical component is now increased.

Using a large wind tunnel setup to generate high levels of free-stream turbulence, measurements were made on a small flat plate wing to investigate the effects of high levels of free stream turbulence on aerodynamic performance. Major conclusions from this work are:

1. Increasing free-stream turbulence levels have a significant effect on both the performance of the airfoil section and wing, as well as the behaviour of the separation bubble present on the suction surface at angles of incidence above a few degrees. The performance of the wing can be assessed

by time-averaged C_L vs α. At higher levels of free-stream turbulence intensity it was observed that the slope of the lift curve does not change significantly; however, a higher $C_{L_{MAX}}$ is reached before stall, effectively delaying the onset of stall. Analysis of surface pressure measurements (confirmed by observation) indicate that formation of the leading edge separation bubble is delayed in the high turbulence case. An additional note is that the change in performance is significant between the low and medium turbulence levels tested (1.5 – 7%); however, the change in performance is less significant when further increasing turbulence from 7-11%.

2. It was observed that the unsteadiness in the surface pressure measurements increased significantly on the suction surfaces in the presence of elevated freestream turbulence. This indicates that the boundary layer is turbulent in these cases, which partially explains the higher values of $C_{L_{MAX}}$; however, the high unsteadiness indicates that the separation bubble which is relatively steady in smooth flow may be unsteady forming and bursting periodically in turbulent flow. This phenomenon was directly observed using flow visualisation.

3. The result of this periodic formation and bursting bubble on the suction surface is a highly transient mean force and moment profile being produced by the wing, which explains to some degree the difficulties observed in controlling these small vehicles on days with a mean wind and high levels of atmospheric turbulence.

7.2 Final Thoughts

Whilst this work represents initial efforts at measuring the effects of turbulence on small wings operating at low Reynolds numbers, it offers only a simplified subset of results due to the simplified nature of the experiment, where finite flat plate wings are exposed to largely homogenous turbulence. As the flow structures very close to the ground, particularly in city and urban environments (where MAVs are envisioned to operate) are largely dominated by the local wakes of objects upstream of the flight path, the large scale variation in flow direction and velocity in these wake structures would have significant influence on the flight of any small vehicle within them. Large flow structures on this scale are difficult to replicate within a wind tunnel and perhaps active turbulence generation schemes may need to be employed upstream.

In contrast, this work does attempt to show the effects of high levels of turbulence, representative of atmospheric flows away from these local effects, the results of which are relatively unique, as the experiments that were conducted are a rare application of experimental aerodynamic work in a environment normally associated with the discipline of wind engineers and atmospheric scientists, rather than aeronautical engineering, which is normally confined to very smooth flows and steady state conditions.

7.3 Recommendations for Further Work

This work forms the basis of an initial investigation into the effects of atmospheric turbulence on low Reynolds number aerodynamics as applicable to micro air vehicles. While this work provided some significant insight to the aerodynamic mechanisms at play, it is limited in terms of scope, and there exists a many opportunities for further work to improve the understanding of the factors involved. Possible areas for further work include:

1. Determine the strength of influence of the wing tip vortex structure by repeating the experiments with a range of aspect ratio wings from low AR to very high (approximating 2D and removing any tip vortex).

2. Analysing a range of different airfoil shapes to determine the effect of shape, wing thickness and leading edge geometry on the behaviour of the upper surface separation region. Particular attention should be payed to determine if there exists some critical case in terms of leading edge thickness and associated pressure gradient where separation is delayed, or made more stable. Particular interest would be to investigate the performance of shapes corresponding to those of birds.

3. This work focuses on only one chord-wise location for the measurement of surface pressures. Investigation of a range of chord-wise locations with simultaneous sampling would yield useful results to investigate the spanwise behaviour of flow shedding identified in this work. Clearly this would need many simultaneous channels of high frequency response pressure transducers to capture.

4. Investigating the possible benefits of passive and active flow control such as boundary layer suction, blowing or trips to control the separation region, particularly improving stability in the high turbulence high alpha cases.

5. Introducing a system where the wing was not restrained in all axis of movement, but allowed to move with the aim of reproducing limited aircraft motions such as pitching and plunging.

6. Using computation packages (CFD codes) to simulate complex turbulent flow conditions, as well to better understand the effects of changing reynolds number on the performance of the wing section used is smooth flow conditions.

7. Introducing higher levels of turbulence and longer integral length scales into the wind tunnel by perhaps employing techniques such as active turbulence generation to better simulate outdoor flow environments.

8. Investigating the effect of free-stream turbulence on boundary layer thickness and development on a surface, such as the ground plan used in this work.

The area of very low Reynolds number aerodynamics, and in particular in unsteady flow regimes, is a fruitful research area with scope for real discovery. It may well be one of the last frontiers of aerodynamic research left.

Appendix A

Terrain and Wind Classification for On-Road Testing

The development of the complete test matrix for outdoor testing considered two primary environmental variables: the mean wind speed, and the surrounding terrain. This included built-up urban and rural landscapes where MAVs might be used, for example surveillance around buildings, streets, hills and trees.

A.1 Terrain Classification

When taking measurements in the ABL it is necessary to use a classification scheme to describe the environment in which the measurements are taken, as the upwind terrain (fetch) and wind strength directly affect the turbulence properties being measured. The main parameters used to classify the surrounding terrain are the fetch roughness (a measure of the number, size and spacing of obstacles on the ground at the measurement location and for several kilometres upstream) and undulation (a measure of the degree of undulation of the ground for several kilometres upstream).

The International Standards Organisation (ISO) provides the widely used ISO/CD 4354 for the classification of terrain roughness; however, as the categories are fairly broad, for this work the classification scheme developed by Davenport (1960) was considered more appropriate. In Table A.1 this classification scheme is outlined, along with the corresponding ISA classification. As no existing reference to classification on terrain undulation or hilliness was found, one was developed based on the extremes of terrain one might encounter during testing. It separates the many different types of terrain found around the world into six very broad classifications, which can be used to describe a particular site, shown in Table A.2.

Table A.1: Classification of effective terrain roughness, Davenport (1960)

No.	Class name	Roughness length(m)	Landscape description 9H: Obstacle height; x: Obstacle separation)	ISO Categories
1	Sea	0.0002	Open water, featureless flat plain, fetch > 3 km	2
2	Smooth	0.005	Obstacle-free land with negligible vegetation, marsh, ridge-free ice	2
3	Open	0.03	Flat open grass, tundra, airport runway, isolated obstacles separated by > 50 H;	2
4	Roughly Open	0.10	Low crops or plant cover, occasional obstacles separated by 20 H	3
5	Rough	0.25	Crops of varying height, scattered obstacles with separation x 12-15 H if porous (shelterbelts) and x 8-12 H if solid (buildings)	3
6	Very Rough	0.5	Intensively cultivated landscape with large farms, orchards, bush land, x 8 H; low well-spaced buildings and no high trees, x 3-7 H	3
7	Skimming	1.0	Full similar-height obstacle cover, x H, e.g. mature forests, densely-built town area	4
8	Chaotic	> 2	Irregular distribution of very large elements: high-rise city centre, big irregular forest with large clearings	4

Table A.2: Classification of terrain undulations

No.	Class name	Hill height (ft)	Description
1	Flat	0	Flat open plain, such as salt lake or sandy desert
2	Slight undulation	0 to< 50	Undulation paddock or plain, slight undulation of a few meters in height with a long period
3	Undulating terrain	50 to < 100	Terrain common in rural farming country
4	Hilly	100 to <500	Hilly terrain
5	Steep	500 to 5000	Steep mountainous terrain
6	Alpine	> 5000	High mountains, valleys and steep cliffs

A.2 Wind Classification

The Beaufort Wind Scale (Table A.3) is a widely used scale for the classification of wind velocity which has been used for decades, and is well understood by meteorologists and wind engineers. It was originally derived for nautical use, but is just as applicable to inland use, although some of the higher categories are less common. This classification scheme was considered appropriate for generalising a set of conditions separated by orders of magnitude, allowing a single point to be inclusive of local variations, gusts and broad trends that show as a change in mean wind speed over the duration of a particular set of tests.

Table A.3: Beaufort wind scale

Force	(m/s)	(knots)	Description
0	0-0.5	0-1	*Calm* - Smoke rises vertically.
1	0.5-1.5	1-3	*Light air* - Direction of wind shown by smoke drift, but not by wind vanes.
2	2-3	4-6	*Light Breeze* -Wind felt on face; leaves rustle; ordinary vanes moved by wind.
3	3.5-5	7-10	*Gentle Breeze* - Leaves and small twigs in constant motion; wind extends light flag.
4	5.5-8	11-16	*Moderate Breeze* - Raises dust and loose paper small branches are moved.
5	8.5-10.5	17-21	*Fresh Breeze* - Small trees in leaf begin to sway; crested wavelets form on inland waters.
6	11-14	22-27	*Strong Breeze* - Large branches in motion, whistling heard in telegraph wires; umbrellas used with difficulty.
7	14.5-17	28-33	*Near Gale* - Whole trees in motion, inconvenience felt when walking against the wind.
8	17.5-20.5	34-40	*Gale* - Breaks twigs off trees, generally impedes progress.
9	21-24	41-47	*Severe Gale* - Slight structural damage occurs (chimney-pots and slates removed).
10	24.5-28	48-55	*Storm* - Seldom experienced inland; trees uprooted; considerable structural damage occurs.
11	28.5-32.5	56-63	*Violent Storm* - Very rarely experienced; accompanied by widespread damage.
12	33-36.5	64-71	*Hurricane*

Appendix B

Notes on the RMIT Industrial Wind Tunnel

The RMIT Industrial Wind Tunnel (IWT) is a closed return, closed test section aero-acoustically treated wind tunnel. A general introduction to the IWT is provided in Chapter 4, with its configuration and layout shown (in larger format) in Figure B.4. The IWT is used for a wide range of experimental work including vehicle aerodynamics, renewable energy research, sport aerodynamics, as well as aero-acoustic work. A overview of the configuration of the tunnel is presented here, as well as a summary of the grids and ground plane, used for this work.

B.1 Wind Tunnel Configuration

A schematic of the general configuration of the IWT is shown in Figure B.4 showing the closed loop layout. It has a single fan powered by a 330 kW electric motor, which is externally mounted (to reduce motor noise) driving the fan by belts. The turning vanes both upstream and downstream of the fan are acoustically treated to further reduce noise from the fan and motor drive systems. The test section is 9 m long by 2 m high by 3 m wide following a 2:1 contraction, and is vented to atmosphere at the downstream end. Extensive analysis of the flow quality in the IWT has been carried out by Pagliarella (2009), Milbank (2005) and Quirillo (1999).

This work required the placement of turbulence-generating grids in the test section and upstream of the contraction, and a raised ground plane mounted at the downstream end of the test section. The placement of these items is shown in Figure B.1.

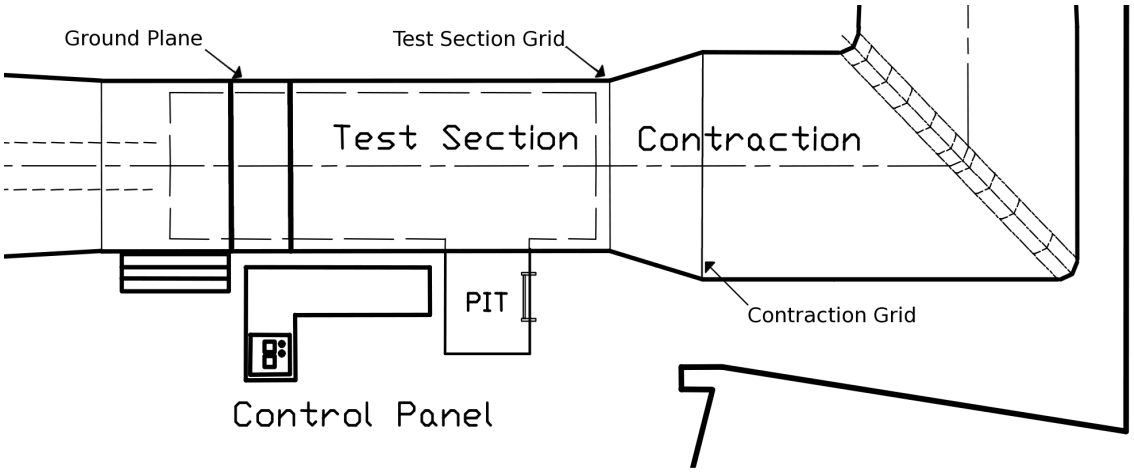

Figure B.1: Position of turbulence generating grids and ground plane in the IWT test section (not to scale)

B.1.1 Turbulence Grids

Turbulence grids were fitted to approximately replicate some of the broad features observed in outdoor measurements described in Chapter 3. Particular attention was paid to replicating high levels of turbulence intensity with as large integral length scales as possible within the constraints of the closed test section.

A number of sizes and shapes of turbulence grids were trialed and the resulting turbulence levels investigated in conjunction with an honours thesis project by Grusovin (2007), who examined the turbulence levels produced by each grid at a number of downstream locations in the test section. Turbulence intensity and integral length scale was measured, and a estimation was made of the downstream distance from the grid required before the flow became homogenous (well mixed). The two grids that were selected from this work were a coarse grid that was fitted in the entrance of the test section which produced very high turbulence levels, and a grid of the same coarseness fitted upstream of the contraction. As the turbulence levels reduce in contracting flows, this latter grid gave a significantly lower level of turbulence in the test section than the grid fitted at the test section entrance. These two grid configurations are shown in Figure B.2.

B.1.2 Ground Plane

Due to the developing and thickening boundary layer that exists on the tunnel floor and walls, which reaches a displacement thickness of approximatively 50 mm according to Pagliarella (2009), a ground plane was fitted to elevate the relatively small model from the floor removing it from the effects of the boundary layer and placing it in a more central location within the test section.

(a) Test section grid at entrance of test section (traverse in foreground)

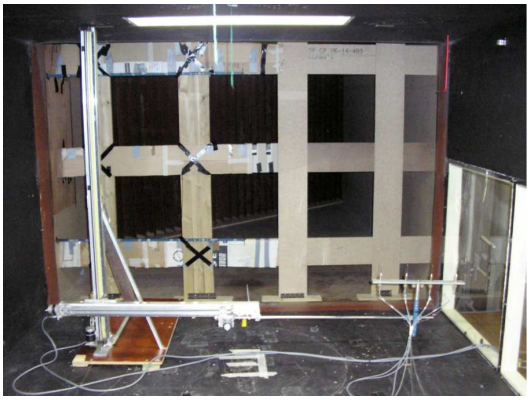

(b) Prototype contraction grid (again with traverse in foreground)

Figure B.2: Grids in both the a) test section and b) in the contraction used to generate different levels of turbulence. (Note grid element size and spacing remain unchanged)

The ground plane, shown in Figure B.3, was raised 0.5 m above the floor level. Details of the ground plane and analysis of the flow at the model location are discussed in Section 4.1.3.

B.2 Wind Tunnel Flow Analysis

Grusovin (2007) examined the mean velocity profile within the tunnel using a set of Cobra probes mounted on a 3 axis traverse, allowing the entire test section to be mapped. The velocity profile and turbulence intensity profile was examined at a number of stream-wise locations along the test section, allowing the turbulence generated by the grid to be examined, identifying how far downstream the model should be placed to ensure the flow was well mixed. It was shown in this work, and in a additional investigation by Pagliarella (2009) that mean velocity profile across the test section remained within 2% of the centreline velocity both with and without grids at the model location with the exception of the 50 mm close to the walls which was affected by the tunnel boundary layer. Since this work used only a small model, detailed flow mapping was only carried out in the immediate model location, the results of which are presented in Chapter 4.

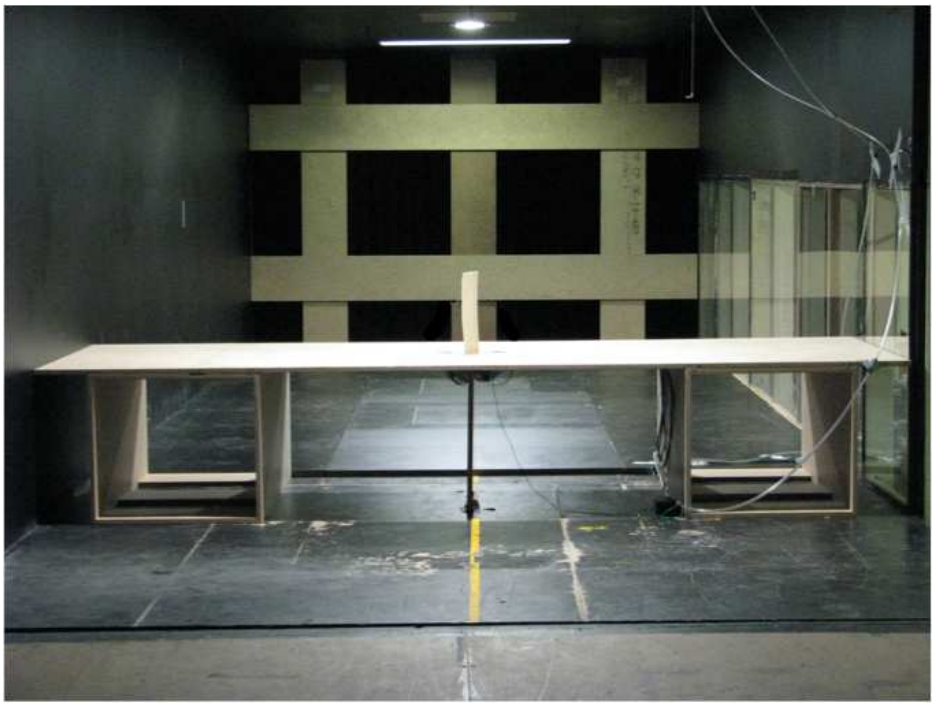

Figure B.3: Ground plane mounted in the test section with wing model mounted on top, DPMS modules underneath and the installed test section grid in the background

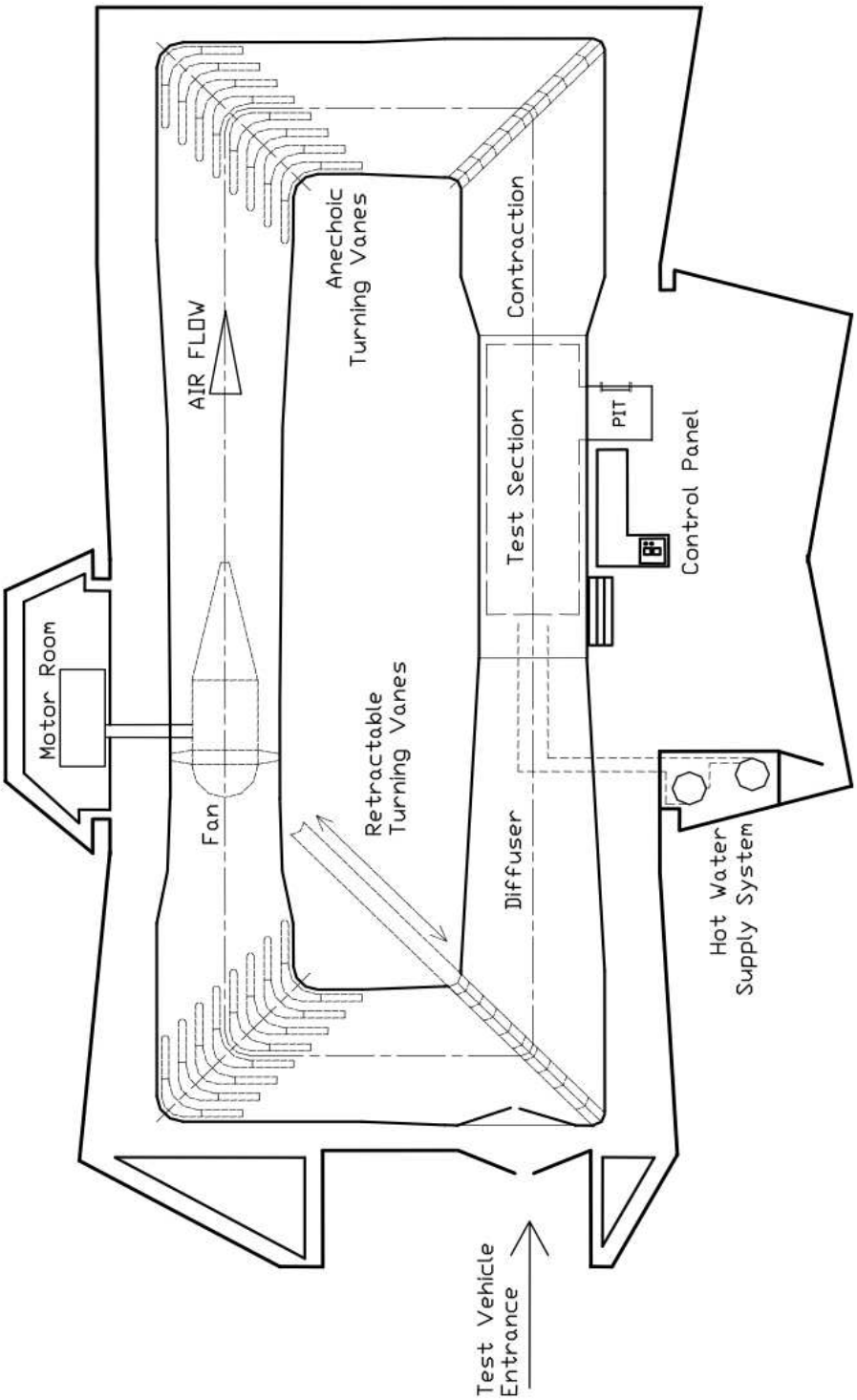

Figure B.4: Schematic of RMIT Industrial Wind Tunnel (Milbank 2005)

Appendix C

Data Post-Processing Methods and Digital Signal Processing

In this section some of the more important techniques and methodologies used in this work for processing the recorded data from experimental measurements are discussed. Digital signal processing is a large and complex field, and numerous texts and resources are devoted to the topic. This appendix first presents a basic overview of data processing used in this work, and includes detail of several important topic that are used extensively to produce the results in this thesis.

C.1 Data Acquisition and Processing Workflow

To produce meaningful results from raw data requires a number of important stages of post processing, and attention to detail at each stage. The post processing process used to produce the results for on-road measurements presented in Chapter 3 is illustrated in Figure C.1, and for producing the results from surface pressure measurements presented in Chapter 5 is shown in Figure C.2.

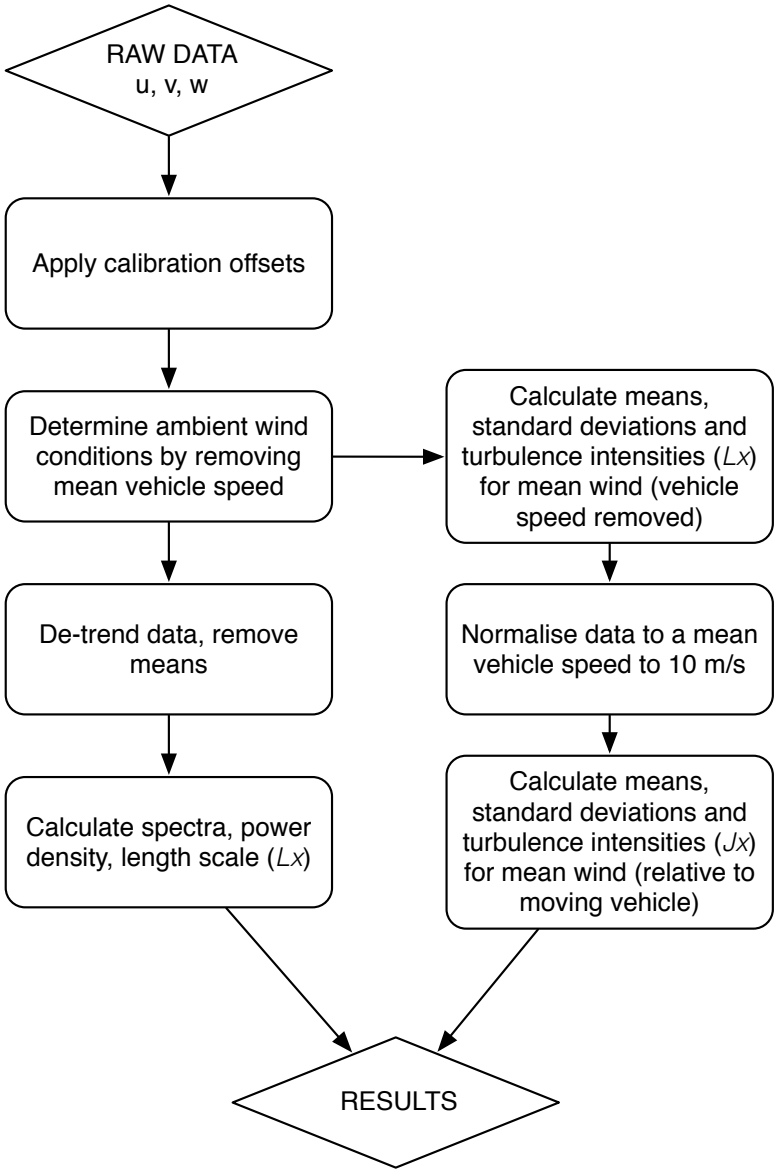

Figure C.1: Data processing work flow for on-road data measurements, producing results for spectral analysis, and turbulence levels relative both to a fixed point and a moving vehicle

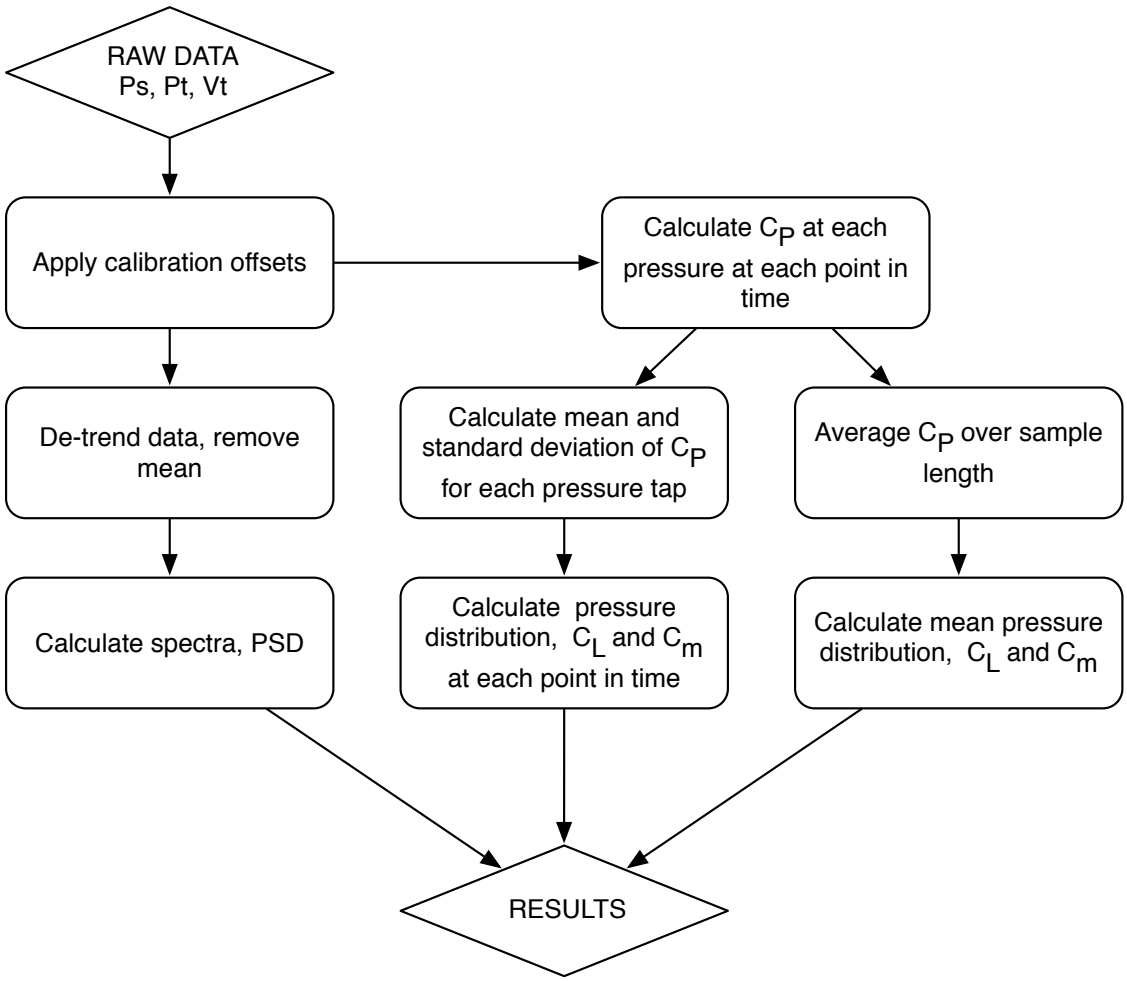

Figure C.2: Data processing work flow for surface pressure measurements

C.2 Calculating Length Scale

This work makes much use of turbulent length scales to characterise the properties of the turbulent flow field. Length scales can be derived through a number of methods; however, one of the most common, and the one used in this work is via auto-correlation. The theory is drawn from ESDU (1974, 1985), and Pope (2000).

The calculation of length scale via auto-correlation is based on Taylor's frozen flow approximation (discussed in Chapter 2) which assumes that the flow is statistically stationary and that the turbulent eddys and structures in the flow do not change appreciably overtime. Given this assumption, the auto-correlation with a time delay, τ, can be considered to approximate a spatial correlation (cross-correlation) with separation determined by the velocity of the flow moving past the sensor, and the time delay used ($\overline{U}_\tau$). This would be the same as taking the signal from two sensors separated by a stream-wise distance.

Covariance is termed a indicator of linear dependance between two date sets (for example x and y), or as a tool for comparison of two sets of data for statistical similarity and is defined as a product of the deviation (σ_{xy})about a mean value (μ).

$$\sigma_{xy} = \lim_{x\to\infty} \sum_{0}^{\tau} (x_i - \mu_z)(y_i - \mu_y) \tag{C.1}$$

In the case where two data sets are perfectly correlated ($x = y$) then the correlation will give a average product of:

$$\sigma_{xy} = \sigma_x \sigma_y \tag{C.2}$$

The correlation between two variables can therefore be normalised giving the correlation coefficient ρ_{xy}:

$$\rho_{xy} = \frac{\sigma_{xy}}{\sigma_x \sigma_y} \tag{C.3}$$

For two data sets that are completely correlated, the correlation coefficient, $\rho_{xy} = 1$, and for completely unrelated data sets $\rho_{xy} = 0$.

In the case of auto correlation, the above concept is applied to the time domain, where the two data sets x and y are instances of the same signal separated by a time delay τ. The covariance function for a dataset x separated by a time lag τ would therefore be given by:

$$C_{xx}(\tau) = \lim_{x\to\infty} \int_0^\tau \{x(t) - \mu_x\}\{x(t+\tau) - \mu_x\}dt \tag{C.4}$$

$$C_{xx}(\tau) = R_{xx}(\tau) - {\mu_x}^2 \tag{C.5}$$

where $R_{xy}(\tau)$ is the cross-correlation function. The auto-correlation function is therefore given by.

$$R_{xx}(\tau) = \lim_{x\to\infty} \int_0^\tau \{x(t)x(t+\tau)dt \tag{C.6}$$

As with two datasets, the result can be normalised, giving a auto-correlation coefficient:

$$\rho_{xx} = \frac{R_{xx}}{{\sigma_x}^2} \tag{C.7}$$

Given the assumption of Taylor's frozen flow described above, and that a flow contains large eddys moving past a sensor, then it follows that the signal measured by the sensor will contain certain periodicity or repeatability. If this holds true then at a particular time separation, τ, the signal will repeat itself. Initially at $\tau = 0$, $\rho_{xx} = 1$. As τ is increased, the eddy progressively moves past the sensor and the flow becomes less correlated. As the eddy moves completely past, ρ_{xx} becomes zero. The size of the eddy can therefore be approximated by the the time of the first zero crossing of the function.

$$T_{xx} = \int_0^\tau \rho_{xx}(\tau)d\tau \tag{C.8}$$

This can be translated into a physical length by:

$$L_{xx} = \overline{U}T_{xx} \tag{C.9}$$

These results are based on the assumption of a "frozen" flow field and a constant mean velocity component which is large with respect to the turbulent fluctuations. In addition to identifying the very large length scales found in some outdoor environments measured in Chapter 3, very long samples are required to obtain a statistically meaningful result, which is not always achievable given the physical constraints of taking measurements outdoors. This method is somewhat better suited to measurement in wind-tunnels, where length scales are smaller and stable conditions can be maintained over a greater time period.

For wind tunnel measurements the relationship between sample length and length scale results was investigated using sample lengths from five minutes to as long as thirty minuets, with little

variation observed in the resilts. From this work, and further analysis by Milbank et al. (2005), data confidence is estimated to be within 5%.

C.3 Spectral Processing - Power Spectral Density

Spectral processing methods are used in processing datasets which contain time histories of a signal as a means of analysing the signal in the frequency domain. This is commonly achieved using Fourier methods to decompose the signal into discrete sinusoids of varying phase and amplitude. Whilst the topic of signal processing is large and is well beyond the scope of this appendix, one of the more common signal processing methods used extensively to produce the results presented in Chapter 5 is the calculation of Power Spectral Density.

Power Spectral Density (PSD) is a method of calculating the distribution of power within a signal with frequency. The key reason for determining a PSD is to examine the frequency content of a given signal, highlighting the periodicity within it. There is no method for determining the exact PSD of a given digital data set, therefore approximation methods are used.

This is achieved by taking a disctrete stationary signal, $x(t)$, and dividing it into equal size successive blocks. The Fourier transform of the k^{th} block is given by:

$$X_k(f,T) = \int_0^T x_k(t) e^{-j2\pi ft} dt \tag{C.10}$$

In practice the discrete Fourier transform is determined using a Fast Fourier transform (FFT) algorithm, and calculated for each block in the time series. The result is a average of each perodiogram, which produces the final PSD. The averaging reduces the variance in the final result and the method is known as Bartlets method (Proakis and Manolakis 1996). If a time history contains a infinite number of blocks, then the variance would reduce to zero, however in practice a given time history is finite, and will therefore contain a finite number of blocks, resulting in variance in the final result that is not zero. The choice of block size therefore becomes a tradeoff between resolution and accuracy, or stability, of the final PSD.

A evolution of Barletts method is Welches method, which improves the result by implementing a windowing function over each block, and overlapping each block by 50%, which allows for an increase in the number of blocks in a given time series without compromising the statistical independence of the segment Fourier transforms. There are many variances on the window function that can be applied to each block, each with their own specific characteristics depending on the nature of the signal being analysed. The window used through this work is the Hann window, which is recognised as a general purpose window function, and is given by the function :

$$w(n) = \frac{1}{2}\left(1 - cos\frac{2\pi n}{N-1}\right) \tag{C.11}$$

The window function $w(n)$ is applies to the m^{th} block of signal x with R window size by the function:

$$x_m(n) \triangleq w(n)x(n+mR) \tag{C.12}$$

The peridogram for the th block is therefore defined by:

$$P_{x_m M}(\omega_k) = \frac{1}{M}\left|FFT_{N,k}(x_m)\right|^2 \triangleq \frac{1}{M}\left|\sum_{n=0}^{N-1} x_m(n)e^{\frac{-j2\pi nk}{N}}\right|^2 \tag{C.13}$$

The equivalent estimated PSD by Welch's method using the FFT is thus:

$$S_x^W(\omega_k) \triangleq \frac{1}{K}\sum_{m=0}^{K-1} P_{x_m,M}(\omega_K) \tag{C.14}$$

C.3.1 Spectral Errors

As the spectra are broard-band, the bias error of the spectral function is a function of signal resolution and quantisation. The dataset was digitally acquired using a 16 bit A/D card over a 10 V input range, which gives a high level of accuracy producing negligible result from signal resolution.

Appendix D

Experimental Tubing Calibration

This appendix provides details on the investigation of the performance of the tubing system integrated into the pressure tapped flat plate wing used for surface pressure measurements as presented in Chapter 5. The tubing system was used to make dynamic measurements of varying surface pressures where the range of interest was 0-50 Hz. As the dynamic response of the tubing system can introduce distortion in the form of signal amplification or attenuation, it is necessary to determine the response of the complete tubing system (including transducer characteristics) and its potential influence on the results. Whilst analytical models exist for predicting the dynamic response of a simple tubing system, the system integrated into this experiment was more complex, consisting of branching, connections and a transducer at one end. Analytical predictions were made and discussed in Chapter 4, however their accuracy of the predictions can only be determined through experimental investigation. A system for measuring the in-situ response of the tubing system and DPMS was devised, and the results are presented here, along with a discussion of their influence on the results and comparison to analytical predictions.

D.1 Experimental Calibration Procedure

The response of the tubing system was measured by taking a known input signal, feeding it into the pressure tap on the surface of the wing and using the DPMS to measure the signal using exactly the same equipment configuration as used in the wind tunnel tests. The reference signal used was measured using the DPMS and a very short (20 mm) tubing length. Such a short tubing length gives negligible dynamic distortion up to the frequency of interest, as shown by the theory on dynamic tubing response presented in Chapter 4. The reference signal is shown in Figure D.2. The signal was generated using a simple signal generator and consisted of single frequencies spaced every 10 Hz between 10 and 100 Hz.

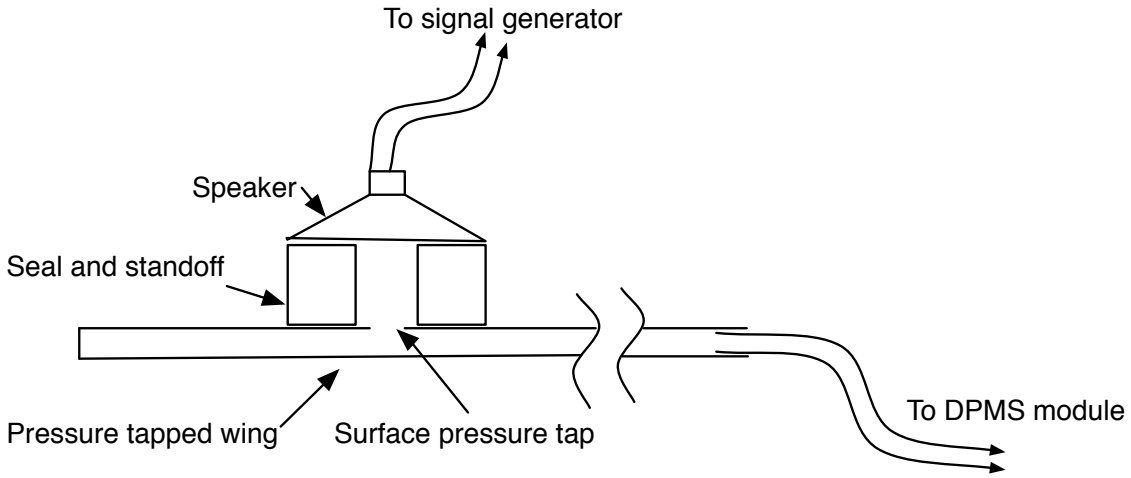

Figure D.1: Diagram of dynamic calibration experimental configuration

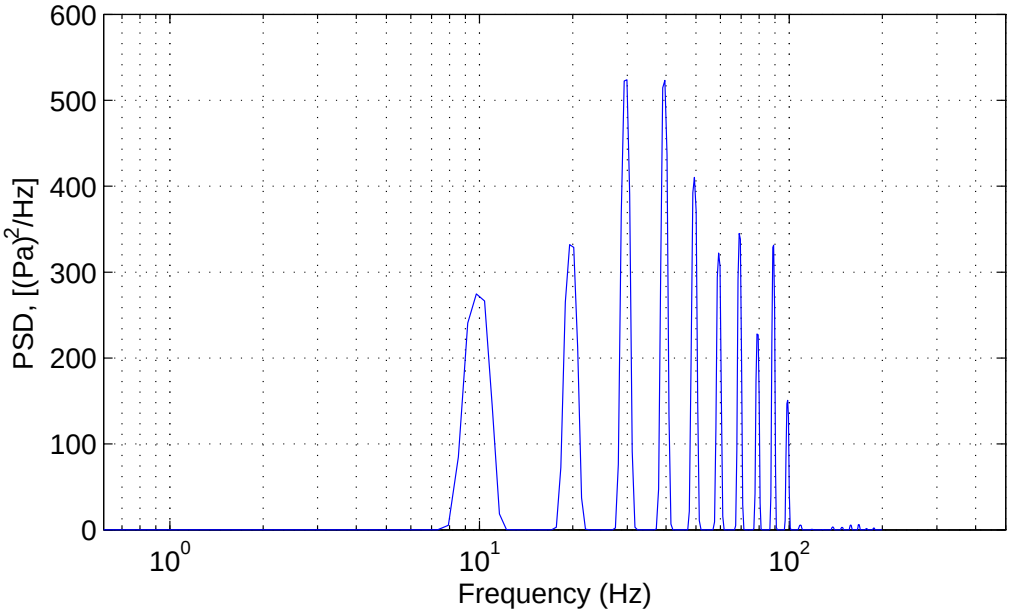

Figure D.2: Reference signal measured directly by DPMS

D.2 Measured Tubing Response

To determine the effect of the complete tubing system on the measured signal, the pressure tap on the surface of the wing was connected to the DPMS using the same equipment and sample settings as used during the experimental wind tunnel work. The reference signal was applied to each pressure tap (as per the diagram in Figure D.1). The same signal measured at the same location over several samples highlighting the good repeatability of the measurements at upto 50 Hz, as shown in Figure D.3.

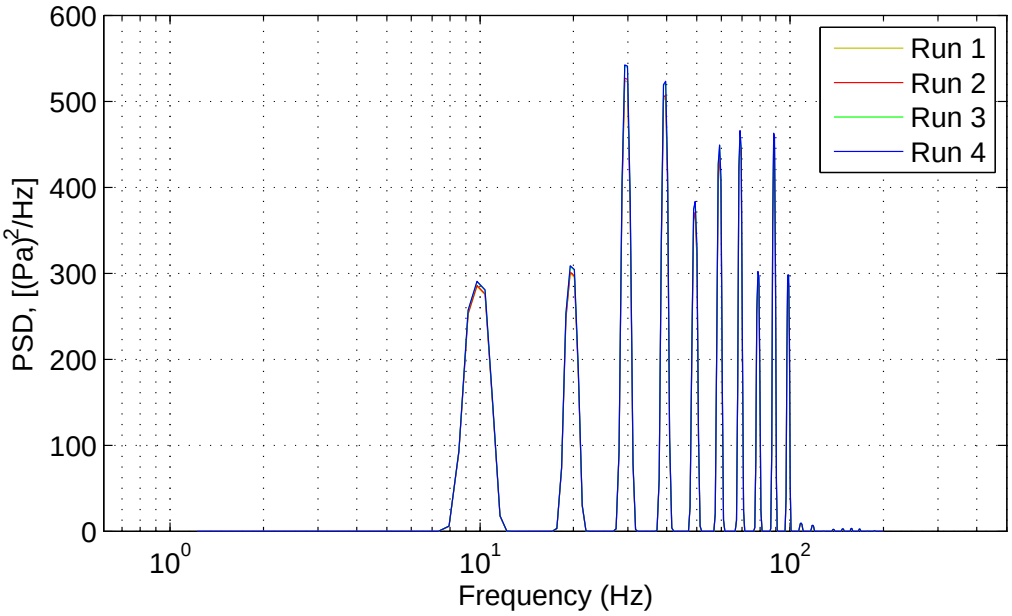

Figure D.3: Repeatability showing signal measured from one pressure tap over several runs

A comparison of the reference signal with the same signal measured using via the pressure tap and tubing system is shown in Figure D.4. Good agreement between the two signals is observed upto 50 Hz, with visible distortion in the form of signal amplification at higher frequencies, which agrees well with the theoretical prediction.

The theoretical tubing response was discussed in Chapter 4, and this response curve was applied to all the data presented in this work. This same theoretical response correction was applied to this signal, and the corrected and uncorrected signal are shown in Figure D.5. Application of the correction has the greatest effect above 50 Hz, where the tubing distortion becomes more significant.

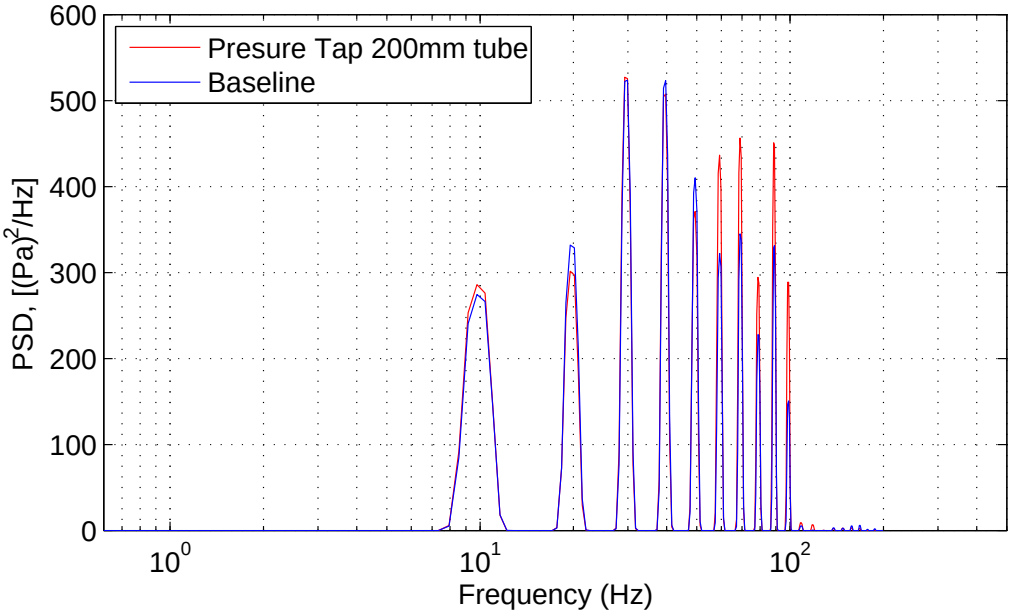

Figure D.4: Comparison of the signal measured at the pressure tap and the baseline, showing good correlation at frequencies below 50 Hz

D.3 Conclusions on Calibration

Comparison between Figures D.5 and D.4 show that the theoretical correction and actual correction required are similar, though the signal distortion is slightly greater in practice than the theoretical model predicts. It is clear that the corrected dynamic response of the system used for all the pressure measurements presented in this thesis (where relatively long tubing systems were required) was very close to the response of a system with sufficiently short lengths as to need no correction at the frequencies of interest, which are less than 50 Hz. Thus the conclusions drawn from this work can be considered valid. However, this may not be the case when higher frequencies are of interest, or longer tubing lengths are required.

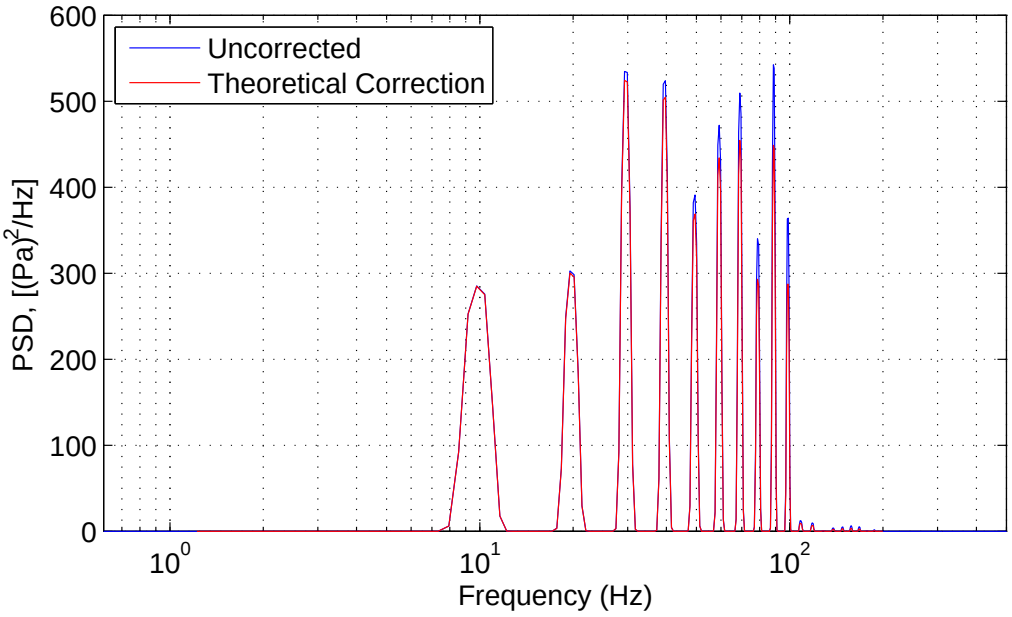

Figure D.5: Signal measured at pressure tap with and without the theoretical tubing correction applied

Bibliography

Abbott, I. H. and von Doenhoff, A. E. (1959). *Theory of Wing Sections*. Dover Publications, Mineola, N. Y. 11501 United States of America, 2nd edition.

Abdulrahim, M. (2004). Dynamic characteristics of morphing air vehicles. Master's thesis, University of Florida, United States of America.

Abdulrahim, M. (2007). *Manoeuvring Control and Configuration Adaptation of a Biologically Inspired Morphing Aircraft*. PhD thesis, University of Florida.

Alam, M. and Sandham, N. D. (2000). Direct numerical simulation of 'short' laminar separation bubbles with turbulent reattachment. *Journal of Fluid Mechanics*, 403:223–250.

Anon (1976a). Characteristics of atmospheric turbulence near the ground. Technical Report 74030, ESDU.

Anon (1976b). Lift-interference and blockage correction for two-dimensional subsonic flow in ventilated and closed wind-tunnels. Technical Report 76028, ESDU.

Anon (1979). Blockage corrections for bluff bodies in confined flows. Technical Report 80024, ESDU.

Anon (1991). Characteristics of atmospheric turbulence near the ground. Technical Report 86010, ESDU.

Arena, A. V. and Mueller, T. J. (1980). Laminar separation, transition, and turbulent reattachment near the leading edge of airfoils. *AIAA Journal*, 18, No 7:747–753.

Bearman, P. W. and Morel, T. (1983). Effect of free-stream turbulence on the flow around bluff bodies. *Progress in Aerospace Sciences*, 20:97–123.

Bergh, H. and Tijdeman, H. (1965). Theoretical and experimental results for the dynamic response of pressure measuring systems. Technical Report NLR-TRF, 328, National Aero and Astronautical Research Institute, Amsterdam.

Bourne, A. (1999). Flow optimisation of the rmit industrial wind tunnel. Undergraduate thesis, RMIT University, Melbourne, Australia.

Bowen, A. J., Flay, R. G. J., and Panofsky, H. A. (1983). Vertical coherence and phase delay between wind components in strong winds below 20m. *Boundary-Layer Meteorology*, (26):313–324.

Briassulis, G., Agui, J. H., and Andreopoulos, Y. (2001). The structure of weakly compressible grid-generated turbulence. *Journal of Fluid Mechanics*, 432:219–283.

Broeren, A. P. and Bragg, M. B. (1998). Low-frequency flowfield unsteadiness during airfoil stall and the influence of stall type. *AIAA Journal*, pages 196–206.

Broeren, A. P. and Bragg, M. B. (2001). Unsteady stalling characteristics of thin airfoils at low reynolds number. In Mueller, T. J., editor, *Fixed and Flapping Wing Aerodynamics for Micro Air Vehicle Applications*, volume 195, page 191. AIAA.

Broughton, B. A., McGranham, B. D., and Selig, M. (2003). Design of low reynolds number airfoils with trips. *Journal of Aircraft*, 40:768–775.

Bullen, R. and McKenzie, N. L. (2001). Bat airframe deign: Flight performance, stability and control in relation to foraging ecology. *Australian Jounal of Zoology*, 49:235–261.

Burger, K. (2002). Budget boost for uavs and counter-terrorism. *Janes Defence Weekly*, 37(1):6.

Carruthers, A. C., Tayler, G. K., Walker, S. M., and Thomas, A. L. R. (2007). Use and function of a leading edge flap on the wings of eagles. In *Aerospace Sciences Meeting and Exibit*, Reno, Nevada. AIAA.

Castro, I. P. and Epik, E. (1998). Boundary layer development after a separated region. *Journal of Fluid Mechanics*, 374:91–116.

Chandar, D. J. and Damodaran, M. (2008). Computational study of unsteady low-reynolds-number airfoil aerodynamics using moving overlapping meshes. *AIAA Journal*, 46:429–438.

Chen, J. M. and Fang, Y.-C. (1996). Strouhal numbers of inclined flat plates. *Journal of Wind Engineering and Industrial Aerodynamics*, 61:99–112.

Cooper, K. R. (1984a). The wind-tunnel simulation of surface vehicles. *Journal of Wind Engineering and Industrial Aerodynamics*, 17:167–198.

Cooper, K. R. (1991). The wind tunnel simulation of wind turbulence for surface vehicle testing. *Journal of Wind Engineering and Industrial Aerodynamics*, 38:71–81.

Cooper, K. R. and Watkins, S. (2007). The unsteady wind environment of road vehicles, part one: A review of the on-road turbulent wind environment. *SAE International*.

Cooper, R. K. (1984b). Atmospheric turbulence with respect to moving ground vehicles. *Journal of Wind Engineering and Industrial Aerodynamics*, 17:2150238.

Cosyn, P. and Vierendeels, J. (2007). Design of fixed wing micro air vehicles. *The Aeronautical Journal*, pages 315–326.

Courtine, S. and Spohn, A. (2003). Formation of separation bubbles on rounded edges. In *Pacific Symposium of Flow Visualisation Image Processing 4, Chamonix, France*.

Crabtree, L. (1958). Prediction of transition in the boundry layer on an aerofoil. *Journal of the Royal Aeronautical Society*, 62:598.

Davenport, A. G. (1960). Rationale for determining design wind velocities. *Journal of Structural Engineering*, 86:39–68.

de Tilly, A. and Sousa, J. M. (2008). Kelvin-helmholts instability due to slot blowing in laminar boundary layers. *AIAA Journal*, 46:1562–1565.

Devinant, P., Lavernt, T., and Hureau, J. (2002). Experimental study of wind-turbine airfoil aerodynamics in high turbulence. *Journal of Wind Engineering and Industrial Aerodynamics*, pages 689–707.

Dorgan, A. J., Loth, E., and Frazzoli, E. (2005). Autonomous control of micro aircraft vehicles falling through an atmospheric boundary layer. *AIAA Journal*, 43:768–775.

Dovgal, A. V., Kozlov, V. V., and Michalke, A. (1994). Laminar boundary layer separation: Instability and associated phenomena. *Progress in Aerospace Sciences*, 30:61–94.

Dryden, H. L. and Hugh, L. (1936). Air flow in the boundary near a plate. Technical Report 562, N. A. C. A.

Dutton, J. A. (1970). Effects of turbulence on aeronautical systems. *Progression Aeronautical Sciences*, 11:67–109.

el Hak, G. (2001a). Micro-air-vehicles: Can the be controlled better? *Journal of Aircraft*, 38:419–429.

el Hak, M. G. (2001b). Micro-air-vehicles: Can they be controlled better? *Journal of Aircraft*, 38:419–429.

Etkin, B. (1981). Turbulent wind and its effects on flight. *Journal of Aircraft*, 18:327–345.

Etkin, B. and Hanson, J. S. (1984). Effect of a damper on the wind-induced oscillations of a tall mast. *Journal of Wind Engineering and Industrial Aerodynamics*, 17:11–29.

Filippone, A. (2006). *Flight Performance of Fixed and Rotary Wing Aircraft*. Butterworth-Hinemann.

Flay, R. (1978). *Structure of a Rural Atmospheric Boundary Layer Near the Ground*. PhD thesis, University of Canterbury, Cristchurch New Zealand.

Gaonkar, G. H. (2008). Review of turbulence modelling and related applications to some problems of helicopter flight dynamics. *American Helicopter Society*, 53(1):87.

Garratt, J. R. (1992). *The Atmospheric Boundary Layer*. Cambridge University Press.

Gaster, M. (1969). The structure and behaviour of laminar separation bubbles. Technical Report R and M NO. 3595, Aerodynamics Division, N. P. L, London.

Gopalarathnam, A. and Selig, M. (2001). Low-speed natural-laminar-flow airfoils: Case study in inverse airfoil design. *Journal of Aircraft*, 38:57–63.

Gosman, A. D. (1999). Developments in cfd for industrial and environmental applications in wind engineering. *Journal of Wind Engineering and Industrial Aerodynamics*, 81:21–39.

Grasmyer, J. M. and Keennon, M. T. (2001). Development of the black widow micro air vehicle. *AIAA Journal*.

Grusovin, M. P. (2007). Modelling of atmospheric boundary layer in rmit industrial wind tunnel. Undergraduate thesis, RMIT University, Melbourne, Australia.

Hewitt, G. F. and Vassilicos, J. C. (2005). *Prediction of Turbulent Flows*. Cambridge University Press.

Hillier, R. and Chetty, N. J. (1981). The effects of stream turbulence on separation bubbles. *Journal of Wind Engineering and Industrial Aerodynamics*, 8:49–58.

Holmes, J. D. (2001). *Wind Loading of Structures*. Spon Press.

Hooper, J. and Musgrove, A. (1997). Reynolds stress, mean velocity, and dynamic static pressure measurement by a four-hole pressure probe. *Journal of Exp Thermal and FLuid Science*, 15:375–383.

Hoover, A. The size of bluejays: Tiny planes to show their stuff in competition.

Horton, H. P. (1968). *Laminar Separation Bubbles in Two and Three Dimensional Incompressible Flow*. PhD thesis, Queens Mary College, University of London, London, UK.

Horton, H. P. (1969). A semi-empirical theory for the growth and bursting of laminar separation bubbles. Technical Report C.P. No. 1073, Ministry of Technology, University of London.

Houghton, E. L. and Carpenter, P. W. (1993). *Aerodynamics for Engineering Students*. Butterworth-Hinemann, 4th edition.

Hsiao, F., Hsieh, M., Lee, M., Chang, W., Chien, Y., Lu, T., and Hsieh, S. (2005). The simulation of unmanned aerial vehicle stability under atmospheric conditions. In *20th Bristol Confrence*.

Hsiao, F., Lui, C., and Tang, Z. (1989). Aerodynamic performance and flow structure studies of a low reynolds number airfoil. *AIAA Journal*, 27:129–137.

Hu, H. and Yang, Z. (2008). An experimental study of the laminar flow separation on a low-reynolds-number airfoil. *Journal of Fluids Engineering*, 130.

Hu, H., Yang, Z., and Igarashi, H. (2007). Aerodynamic hysteresis of low-reynolds number airfoil. *journal of Aircraft*, 44 No 6:2083.

Irwin, H. P., Cooper, K. R., and Girard, R. (1979). Correction of distortion effects caused by tubing systems in measurements of fluctuating pressures. *journal of Industrial Aerodynamics*, 5:93–107.

Jenkins, D. A., Ifju, P. G., Abdulrahim, M., and Olipra, S. (2001). Assessment of controllability of micro air vehicles. In *Proceedings of the 16th Bristol Unmanned Air Vehicle Systems Conference*.

Jones, A. R. (2008). Low reynolds number aerodynamics of leading edge flaps. *Journal of Aircraft*, 45:342–774.

Jones, B. M. (1934). Stalling. *Journal of the Royal Aeronautical Society*, 38:753–770.

Jones, J. G. (2007). Measured statistics of multicomponent gust patterns in atmospheric turbulence. *Journal of Aircraft*, 44:1559–1567.

Kaimal, J. and Finnigan, J. J. (1994). *Atmospheric Boundary Layer Flows, Their Structure and Measurement*. Oxford University Press.

Kellogg, J., Bovals, C., Foch, R., Sullivan, C., Dahlburg, J., Gardner, J., Ramamuti, R., Scimbi, A., Srull, D., Hartly, R., and Spears, W. (2002). The nrl micro tactical expendable (mite) air vehicle. *The Aeronautical Journal*, pages 431–434.

Khrabrov, A. and Ol, M. (2007). Effects of flow separation on aerodynamic loads in linearised thin airfoil theory. *Journal of Aircraft*, 41:944.

Kolmogorov, A. N. (1961). A refinement of previous hypotheses concerning the local structure of turbulence in a viscous incompressible fluid at high reynolds number. *Journal of Fluid Mechanics*, 13:82.

Kristensen, L. and Jensen, N. O. (1979). Lateral coherence in isotropic turbulence and in the natural wind. *Boundry-Layer Meteorology*, 17:353–373.

Kristensen, L., Panofsky, H. A., and Smith, S. D. (1980). Lateral coherence of longitudinal wind components in strong wings. *Boundary-Layer Meteorology*, 21:1573–1472.

Lawson, T. V. (1980). *Wind Effects on Buildings*. Applied science publishers.

Lian, Y. and Shyy, W. (2007). Laminar turbulent transition of a low reynolds number rigid or flexible airfoil. *AIAA Journal*, 45:1501–1513.

Lian, Y., Shyy, W., Viieru, D., and Zhang, B. (2003). Membrane wing aerodynamics for micro air vehicles. *Progression Aerospace Sciences*, 39:425–465.

M, T., G, A., R, S., and M, G. (2005). Development of a morphing micro air vehicle wing using the combined pod and pse technique. *AIAA Journal*, pages 1–9.

McCullough, G. B. and Gault, D. E. (1951). Examples of three representative types of airfoil-section stall at low speed. Technical Report TN 2502, NACA.

McGregor, I. (1954). *The Regions of Local Boundary-Layer Separations and their role in the Stalling of Aerofoils*. PhD thesis, Queens Mary College, London, UK.

McMasters, J. H. and Henderson, M. L. (1980). Low speed single element airfoil synthesis. *Technical Soaring*, 2:1–21.

McMichael, J. M. and Francis, C. M. S. Micro air vehicles - toward a new dimension in flight.

Migita, S. A. (2006). Effects of low reynolds numbers on the aerodynamics on micro-air vehicles. Technical report, University of Hawaii at Manoa.

Milbank, J. (2005). *Investigations of Fluid-Dynamic Cavity Oscillations, and the Effects of Flow Angle, In an Automotive Context Using an Open-Jet Wind Tunnel*. PhD thesis, RMIT University, Melbourne, Australia.

Milbank, J., Loxton, B., Watkins, S., and Melbourne, W. (2005). Replication of atmospheric conditions for the purpose of testing mavs. Technical report, RMIT University.

Moschetta, J.-M. and Thipyopas, C. (2007). Aerodynamic performance of a biplane micro air vehicle. *Journal of Aircraft*, 44:291–299.

Moulin, B. and Karpel, M. (2007). Gust load alleviation using special control surfaces. *Journal of Aircraft*, 44:17–25.

Mousley, P., Watkins, S., and J, H. (1998). Use of a hot-wire anemometer to examine the pressure signal of a high-frequency pressure probe. In *13th Australasian Fluid Mechanics Conference*, Melbourne, Australia.

M.Ramasamy, Lee, T. F., and Leishman, J. G. (2007). Flowfield of a rotating–wing micro air vehicle. *Journal of Aircraft*, 44:1236–1244.

Mueller, T. J. (1989). *Low Reynolds Number Aerodynamics: Proceedings of the Conference*. Springer-Verlag, New York.

Mueller, T. J. (1999). Aerodynamic measurements at low reynolds numbers for fixed wing micro-air vehicles. Technical report, University of Notre Dame, VKI, Belgium.

Mueller, T. J., editor (2001). *Fixed and Flapping Wing Aerodynamics for Micro Air Vehicle Applications*, volume 195. Progress in Astronautics and Aeronautics, AIAA.

Mueller, T. J. and DeLaurier, J. D. (2003). Aerodynamics of small vehicles. *Annu. Rev. Fluid Mech*, 35:89–111.

Mueller, T. J., Kellogg, T. C., Ifju, P. G., and Shkarayev, S. V. (2007). *Introduction to the Design of Fixed Wing Micro Air Vehicles*. AIAA Education Series.

Murakami, S. (1998). Overview of turbulence models applied in cwe–1997. *Journal of Wind Engineering and Industrial Aerodynamics*, 74-76:1–24.

Nagib, H. M. and Corke, T. C. (1984). Wind microclimate around buildings: Characteristics and control. *Journal of Wind Eningeering and Industrial Aerodynamics*, 16:1–15.

Nieuwstadt, F. T. M. and van Dop, H. (1981). *Atmospheric Turbulence and Air Pollution Modelling*. D. Reidel Publishing Company.

Oke, T. R. (2004). Siting and exposure of meteorological instruments at urban sites. In *Proceedings of the 27th NATO/CCMS international technical meeting on air pollution modelling and application. Kluwer, Banff, Canada*. Springer.

O'Neill, P. L., Nicolaides, D., and Soria, J. (2004). Autocorrelation functions and the determination of integral length with reference to experimental and numerical data. In *15th Australasian Fluid Mechanics Conference*. The University of Sydney.

Orr, M. W., Rasmussen, S. J., Karni, E. D., and Blake, W. B. (2005). Framework for developing and evaluating mav control algorithms in a realistic urban setting. In *American Control Confrence*, pages 4096–4101, Portland, OR, USA.

Owen, P. R. and Klanfer, L. (1955). On the laminar boundary layer separation form the leading edge of a thin aerofoil. Technical Report C. P. No. 220, Ministry of Technology, London.

Pagliarella, R. M. (2009). *On the Aerodynamic Performance of Automotive Vehicle Platoons Featuring Pre and Post-Critical Leading Forms*. PhD thesis, RMIT University, Melbourne, Australia.

Panoffsky, H. A. and Townsend, A. A. (1963). Change of terrain roughness and the wind profile. *Quarterly Journal of the Royal Meteorological Society*, 90:147–155.

Panofsky, H. A. and Dutton, J. A. (1976). *Atmospheric Turbulence, Models and Methods for Engineering Applications*. John Wiley and Sons.

Panofsky, H. A. and Press, H. (1962). Meteorological and aerological aspects of atmospheric turbulence. In A., F., D., K., and L.H.G., S., editors, *Progress in Aeronautical Sciences*, volume 3.

Peake, D. J an Tobak, M. (1982). Three-dimensional flows about simple components at angle of attack. In *AGARD Lecture Series NO. 121*.

Pelletier, A. and Mueller, T. J. (2000). Low reynolds number aerodynamics of low- aspect-ratio thin/flat/cambered-plate wings. *Journal of Aircraft*, 37:825–832.

Pelletier, A. and Mueller, T. J. (2001). Effect of endplates on two-dimensional airfoil testing at low reynolds numbers. *Journal of Aircraft*, Vol. 38 No. 6:825–832.

Phillips, W. F. (2004). *Mechanics of Flight*. John Wiley and Sons, New York.

Pines, D. J. and Bohorquez, F. (2006). Challenges facing future micro-air-vehicle development. *Journal of Aircraft*, 43:290–305.

Pinton, J. and Labbe, R. (1994). Correction to the taylor hypothesis in swirling flows. *Journal of Physics*, page 1461.

Pope, S. B. (2000). *Turbulent Flows*. Cambridge University Press.

Proakis, J. and Manolakis, D. (1996). *Digital Signal Processing*. Prentice-Hall, NJ.

Quirillo, G. (1999). Flow optimisation of the rmit industrial wind tunnel. Undergraduate thesis, RMIT University, Melbourne, Australia.

Radespiel, R., Windte, J., and Scholz, U. (2007). Numerical and experimental flow analysis of moving airfoils with laminar separation bubbles. *AIAA Journal*, 45:1346–1356.

Reed, D. A. and Scanlan, R. H. (1984). Autoregressive representation of longitudinal, lateral and vertical turbulence spectra. *Journal of Wind Engineering and Industrial Aerodynamics*, 17:199–214.

Reich, G. and Sanders, B. (2007). Introduction to morphing aircraft research. *Journal of Aircraft*, 44(4).

Ricketts, P. (2001). Uav market survey indicates operational trial. Technical Report 6, The Defence Reporter: Australia and Asia Pacific, Canberra, Australia.

Saathoff, P. J. and Melbourne, W. H. (1997). Effects of free-stream turbulence on surface pressure fluctuations in a separation bubble. *Journal of Fluid Mechanics*, 337:1–24.

Sachs, G. (2007). Why birds and miniscale airplanes need no vertical tail. *Journal of Aircraft*, 44:1159–1167.

Schlicting, H. (1960). *Boundary Layer Theory*. McGraw Hill Book Company.

Shiotani, M., Iwatani, Y., and Kuroha, K. (1978). Magnitudes and horizontal correlations of vertical velocities in high winds. *Meteorological Society of Japan*, 56:35–42.

Shyy, W., Berg, M., and Ljungqvist, D. (1999). Flapping and flexible wings for biological and micro air vehicles. *Progress in Aerospace Sciences*, 35:455–505.

Sicot, C. and Aubrum, S. (2006). Unsteady characteristics of the static stall of an airfoil subjected to free-stream turbulence level upto 16 *Journal of Experimental Fluids*, 41:641–648.

Simons, M. (1999). *Model Aircraft Aerodynamics*. Special Interest Model Books.

Simpson, R. L. (1996). Aspects of turbulent boundary-layer separation. *Progress in Aerospace Sciences*, 32:457–521.

Sinha, A. K., Kusumo, R., Scott, M. L., Bil, C., and Mahondas, P. (2001). A system approach to issues and challenges of uav systems. In *Proceedings of the 16th Bristol Unmanned Air Vehicle Systems Conference*.

Spedding, G. R. and Lissaman, P. B. S. (1998). Technical aspects of microscopic flight systems. *Journal of Avian Biology*, 29:458–568.

Stalp, S. R., Skrbek, L., and Donnelly, R, J. (1999). Decay of grid turbulence in a finite channel. *Physical Review Letters*, 82(24).

Stollery, J. L. and Dyer, D. J. (1989). Wing-section effects on the flight performance of a remotely piloted vehicle. *Journal of Aircraft*, 26:932–938.

Street, R. L., Watters, G. Z., and Vennard, J. K. (1996). *Elementary Fluid Mechanics*. John Wiley and Sons.

Stull, R. B. (1988). *An Introduction to Boundry Layer Meteorology*. Kluwer Academic Publishers.

Sunada, S., Yasuda, T., Yasuda, K., and Kawachi, K. (2002). Comparison of wing characteristics at an ultra low reynolds number. *Journal of Aircraft*, 39:331–338.

Sutton, O. G. (1953). *Micrometeorology*. McGraw and Hill Books, New York.

Swalwell, K. E. (2005). *The Effect of Turbulence on Stall of Horizontal Axis Wind Turbines*. PhD thesis, Monash University, Melbourne, Australia.

Swalwell, K. E., Sheridan, J., and Melbourne, W. H. (2004). The effect of turbulence intensity on performance of a naca4421 airfoil section. In *42nd AIAA Aerospace Sciences Meeting and Exibit*, Reno, Nevada. AIAA, AIAA.

Tang, L. (2008). Raynolds-averadged navier stokes simulation of low-reynolds-number airfoil aerodynamics. *Journal of Aircraft*, 45:848–856.

Tani, I. (1964). Low speed flows involving bubble separations. *Progression Aeronautical Sciences*, 4.

Taylor, G. I. (1938). The spectrum of turbulence. *Proceedings of the Royal Society of London. Series A, Mathematical and Physical Sciences*, pages 476–490.

Teunissen, H. W. (1980). Structure of mean winds and turbulence in the planetary boundary layer over rural terrain. *Boundry-Layer Meteorology*, 19:187–221.

Torres, G. E. and Mueller, T. J. (2000a). Aerodynamic characteristics of low aspect ratio wings at low reynolds numbers. In *Proceedings of the Conference on Fixed, Flapping and Rotary WIng Vehicles at Very Low Reynolds Numbers*, pages 278–305, Notre Dame, Indiana. University of Notre Dame.

Torres, G. E. and Mueller, T. J. (2000b). Effects of propeller slipstream on the aerodynamic characteristics of low aspect ratio wings at very low reynolds numbers. In *Proceedings of the Conference on Fixed, Flapping and Rotary WIng Vehicles at Very Low Reynolds Numbers*, pages 373–395, Notre Dame, Indiana. University of Notre Dame.

Torres, G. E. and Mueller, T. J. (2000c). Micro aerial vehicle development: Design, components, fabrication and flight-testing. In *Proceedings of Unmanned Systems*, Orlando, Florida. University of Florida.

Torres, G. E. and Mueller, T. J. (2004). Low aspect ratio wing aerodynamics at low reynolds numbers. *AIAA Journal*, Vol 42. No. 5:865–873.

Townsend, A. A. (1966). Wind and the formation of inversions. *Atmospheric Environment*, 1:173–175.

Townsend, A. A. (1976). *The Structure of Turbulent Shear Flow*. Cambridge University Press, Cambridge, England, 2nd edition.

Tuncer, I. H. and Platzer, M. F. (2000). Computational study of flapping airfoil aerodynamics. *Journal of Aircraft*, 37:514–520.

Uchida, T. and Ohya, Y. (2003). Large-eddy simulation of turbulent airflow over complex terrain. *Journal of Wind Engineering and Industrial Aerodynamics*, 91:219–229.

Van der Hoven, I. (1957). power spectrum of horizontal wind speed in the frequency range from 0.0007 to 900 cycles per hour. *Journal of Atmospheric Sciences*, 14:160–164.

Vino, G. (2005). *An Experimental Investigation into the Time-Averaged and Unsteady Aerodynamics of a Simplified Passenger Vehicle in Isolation and in Convoys*. PhD thesis, RMIT University, Melbourne, Australia.

Von Doenhoff, A. E. (1938). A preliminary investigation of boundary-layer transition along a flat plate with adverse pressure gradient. Technical Report TN 639, NACA.

Walshe, D. E. J. (1972). Wind-excited oscillation of structures. Technical report, Her Majesty's Stationery Office, London, UK.

Walshe, D. E. J., Thuillier, R., and Lappe, U. (1964). Wind and temperature profile characteristics from observations on a 1400 ft tower. *Journal of Applied Meteorology*, 3:299–306.

Ward, J. (1963). The behaviour and effects of laminar separation bubbles on airfoils in incompressible flow. *Journal of the Royal Aeronautical Society*, 67:783–789.

Wasco, M. (2003). Wind tunnel simulation of on-road turbulence using an oscillating, upstream pendulum. Undergraduate thesis, Monash University.

Watkins, S. (1990). *Wind-Tunnel Modelling of Vehicle Aerodynamics: With Emphasis on Turbulent Wind Effects on Commercial Vehicle Drag*. PhD thesis, School of Aerospace, Mechanical and manufacturing Engineering, RMIT University.

Watkins, S. (2003). Development of a micro air vehicle. *Aeronautical Journal (Royal Aeronautical Society)*, 107(1068):117–123.

Watkins, S. and Cooper, K. R. (2007). The unsteady wind environment of road vehicles, part two: Effects on vehicle development and simulation of turbulence. *SAE International*.

Watkins, S., Loxton, B., Bil, C., Abdulrahim, M., and Milbank, J. (2008). Flow fields in complex terrain and their challenges to micro flight. In *AIAA Guidance, Navigation and Control Conference and Exhibit*, number 2008-6509 in AIAA, Honolulu, Hawaii.

Watkins, S., Milbank, J., and Loxton, B. (2006). Atmospheric winds and their effects on micro air vehicles. *AIAA Journal*.

Watkins, S., Ravi, S., and Loxton, B. (2010a). The effect of turbulence on the aerodynamics of low reynolds number wings. In *The 2010 International Conference of Mechanical Engineering*. ICME.

Watkins, S. and Saunders, J. W. (1995). Turbulence experiences by road vehicles under normal driving conditions. *SAE Journal*, 120:173–181.

Watkins, S., Saunders, J. W., and H, H. P. (1995). Turbulence experienced by moving vehicles part i. introduction and turbulence intensity. *Journal of Wind Engineering and Industrial Aerodynamics*, 57:1–17.

Watkins, S., Thompson, M., Shortis, M., Segal, R., Abdulrahim, M., and Sheridan, J. (2010b). An overview os expriments on the dynamic sensitivity of mavs to turbulence. *Aeronautical Journal (Royal Aeronautical Society)*, 114:485–492.

Watkins, S. and Vino, G. (2004). The turbulent wind environment of birds, insects and mavs. In *15th Australasian Fluid Mechanics Conference*. The University of Sydney.

Watmuff, J. H. (1999). Evolution of a wave packet into vortex loops in a laminar separation bubble. *Journal of Fluid Mechanics*, 397:119–169.

Wieringa, J. (1992). Updating the davenport roughness classification. *Wind Eningeering and Industrial Aerodynamics*, 41:357–368.

Wilcox, D. C. (1998). *Turbulence Modelling for CFD*. DCW Industries, California, USA, 2nd edition.

Willis, G. E. and Deardorff, J. W. (1976). On the use of taylor's hypothesis for diffusion in the mixed layer. *Journal of Royal Meteorological Society*, 102:817–822.

Wilson and Schneph (2001). Micro air vehicles: New military capability. In *Proceedings of the 16th Bristol Unmanned Air Vehicle Systems Conference*.

Woolley, J. (2007). Calibration of a four component micro force balance and investigations into the effects of turbulence on mavs. Undergraduate thesis, RMIT University, Melbourne, Australia.

Yang, Z. and Hu, H. (2008). Laminar flow separation and transition on a low-reynolds-number airfoil. *Journal of Aircraft*, 45:1067–2086.

Yasuda, T. and K, Y. (2002). Comparison of wing characteristics at an ultra low reynolds number. *Journal of Aircraft*, 39:331–338.